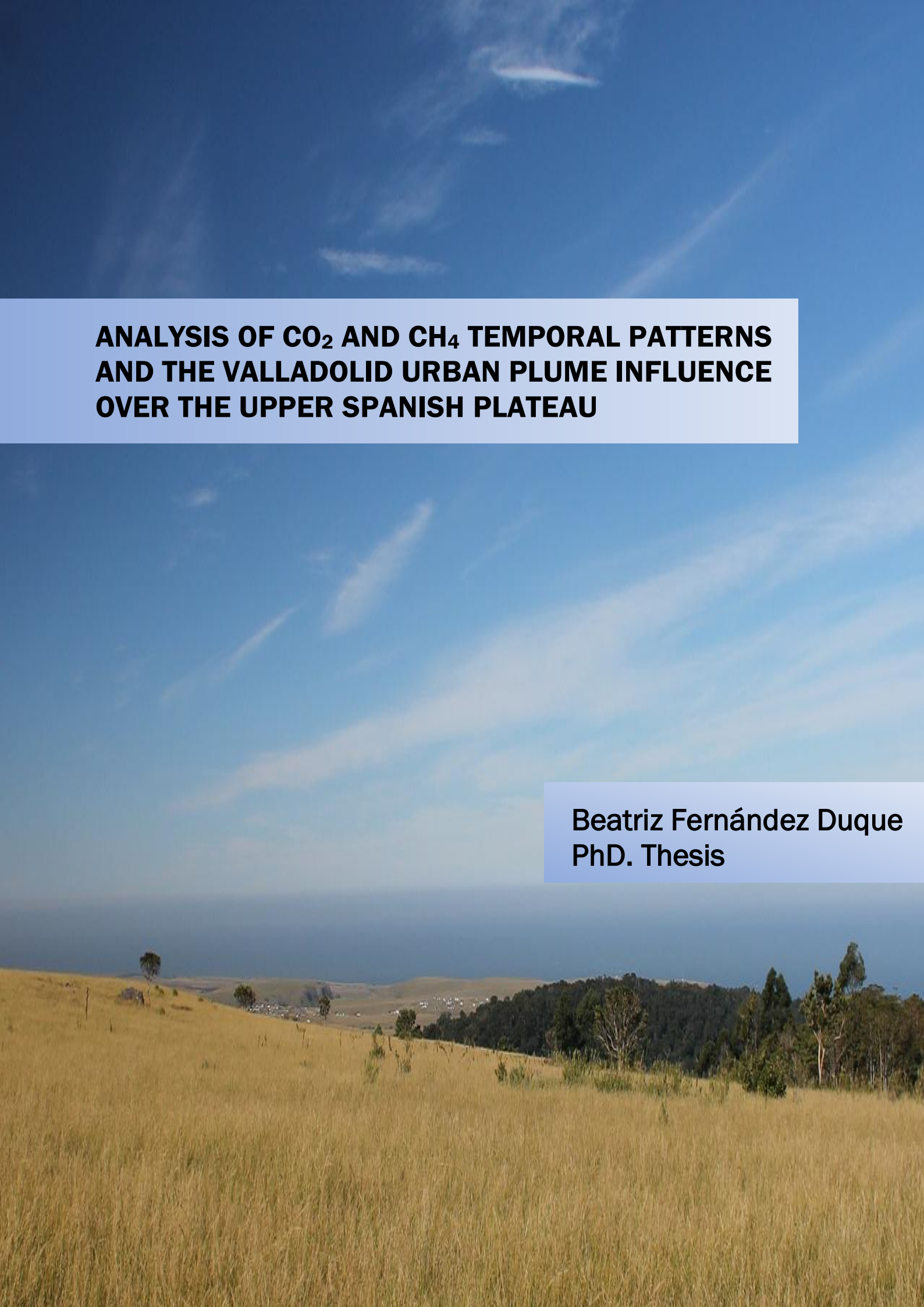

ANALYSIS OF CO_2 AND CH_4 TEMPORAL PATTERNS AND THE VALLADOLID URBAN PLUME INFLUENCE OVER THE UPPER SPANISH PLATEAU

Beatriz Fernández Duque

PhD. Thesis

Universidad de Valladolid

Escuela de Doctorado Universidad de Valladolid

PROGRAMA DE DOCTORADO EN FISICA

TESIS DOCTORAL:

ANALYSIS OF CO_2 AND CH_4 TEMPORAL PATTERNS AND THE VALLADOLID URBAN PLUME INFLUENCE OVER THE UPPER SPANISH PLATEAU

ANÁLISIS DE LOS PATRONES TEMPORALES DE CO_2 Y CH_4 Y DE LA INFLUENCIA DEL PENACHO URBANO DE VALLADOLID EN LA MESETA NORTE CASTELLANA

Presentada por Beatriz Fernández Duque para optar al grado de
Doctora por la Universidad de Valladolid

Dirigida por:
Dra. María Luisa Sánchez Gómez
Dr. Isidro A. Pérez Bartolomé

Analysis of CO_2 and CH_4 temporal patterns and the Valladolid urban plume influence over the upper Spanish plateau

PhD Student:

Beatriz Fernández Duque

Supervisors:

Dra. María Luisa Sánchez Gómez
Dept. Applied Physics
University of Valladolid
Paseo de Belén, 7, 47011. Valladolid (Spain)

Dr. Isidro A. Pérez Bartolomé
Dept. Applied Physics
University of Valladolid
Paseo de Belén, 7, 47011. Valladolid (Spain)

Supervisor of the international stay:

Dr. Alfredo Rocha
Dept. Physics
University of Aveiro
Campus Universitário de Santiago, 3810-193 Aveiro (Portugal)

External reviewers:

Dra. Mastura Mahmud
Dept. Social, Environmental and Developmental Sustainability Research
Universiti Kebangsaan
Malaysia
43600 UKM, Bangi, Selangor (Malaysia)

Dra. Florinda Artuso
Dept. Diagnostics and metrology Laboratory
Italian National Agency for New Technologies Energy and Sustainable Economic Development
Lungotevere Thaon di Revel, 76
00196, Rome (Italy)

Doctorate program:

Doctorate in Physics

Faculty of Sciences. University of Valladolid (Spain)

Place of publication: Valladolid, Spain

Year of publication: 2021

Printed by: LLAR digital

Design: Deankruger from Pixabay (cover) and Beatriz Fernández Duque (main text and graphical material).

UVa FacultaddeCiencias

GCA Grupo de Contaminación Atmosférica

General index

Acknowledgements / Agradecimientos

This thesis has been carried out at the Department of Applied Physics of the University of Valladolid under the frame of the project CGL2014-53948-P and the predoctoral contract BES-2015-074254 funded by the Spanish Ministry of Economy and Competitiveness and co-financed by the European Regional Development Fund (FEDER). The University of Valladolid and the Santander Bank have also financed this work throughout two grants for attending international conferences in which some of the results of this thesis have been presented. I would like to acknowledge all these institutions for their support and financial contribution.

La presente tesis doctoral se ha desarrollado bajo la supervisión de la Dra. María Luisa Sánchez Gómez y el Dr. Isidro A. Pérez Bartolomé a quienes debo agradecer la oportunidad brindada para formarme en el seno del Grupo de Contaminación Atmosférica (GCA). Agradecerles la confianza depositada en mí desde el primer momento y sus incansables ánimos al hacerme creer que todo es posible con esfuerzo y dedicación. Gracias por todos los conocimientos transmitidos y por su apoyo incondicional en cada uno de mis pasos.

De igual modo, me gustaría agradecer a mis compañeros del GCA, Mª Ángeles y Nuria por la adquisición de los datos y sus ánimos en el transcurso de estos años, a Javier Peláez por resolver los problemas de mantenimiento surgidos durante la realización de las medidas y a Alberto por su apoyo y buen humor.

To my international supervisor, Dr. Alfredo Rocha at the University of Aveiro (Portugal) for giving me the chance of being part of the Atmospheric Processes & Modelling (APM) group. Thanks to all the members of APM for investing part of your time in me.

Al Departamento de Física Aplicada por permitirme iniciarme en las labores docentes completando de este modo mi formación predoctoral, así como a todos sus miembros que se han interesado por el desarrollo de la presente tesis.

A mi familia y amigos. Mención especial merecen mis padres, porque sin su apoyo incondicional nunca hubiera podido llegar hasta aquí. A mi hermana Verónica por sentirse tan orgullosa de mí como yo de ella. Y por supuesto a Jordán por estar conmigo en cada reto y compartir todas mis ilusiones.

Beatriz Fernández Duque

1. Abstract / Resumen

1.1. Abstract

Since the Industrial Revolution, the atmospheric mole fractions of greenhouse gases have changed due to human activities, leading to an increase in the average temperature of the planet. Determining greenhouse gases at regional background sites is crucial vis-à-vis assessing what impact anthropogenic emissions have on the atmospheric environment. However, observational studies are still scarce at such background sites. The current thesis first seeks to improve existing knowledge concerning the evolution of the two major greenhouse gases (CO_2 and CH_4) in terms of trends, growth rate and seasonal variations in the lower atmosphere. Secondly, the effect of the Valladolid urban plume on the final CO_2 and CH_4 mixing ratios recorded at the Low Atmosphere Research Centre (CIBA) was analysed in order to better understand its impact on the final mixing ratios recorded at the station. To achieve this goal, dry continuous CO_2 and CH_4 mixing ratios were carried out over five and a half years (from 15 October 2010 to 29 February 2016) at 8.3 m. height using a Picarro G1301 analyser at a remote rural site at the CIBA station on the upper Spanish plateau. This is the first study conducted at the CIBA station with such lengthy records, employing a database collected with a high precision instrument and differentiating between diurnal and nocturnal records. Firstly, in order to analyse temporal patterns, the time series was conveniently detrended and deseasonalised from the observed values so as to capture the intrinsic dynamics of the time series associated to different phenomena. In order to accurately describe CO_2 and CH_4 temporal evolution over time, three scientific works employing different mathematical functions were performed. The use of different mathematical functions enabled detection of possible bias caused by the method applied and provided a comparison among the mathematical functions employed in terms of ease of use, computational cost involved in the calculations and final data fit. The first paper used a harmonic equation comprising a third-degree polynomial (trend) plus a series of four harmonics (seasonal cycle), each made up of a constant and a variable part along the time series. The second paper applied an Epanechnikov, a Gaussian, a biweight, a triangular, a tricubic and a rectangular kernel function to extract the salient features of the CO_2 and CH_4 temporal patterns. Moreover, a novel method for simultaneously determining the optimal bandwidths of kernel functions for the long and short-term based on experimental contour plots of R^2 values was proposed. The third paper was grounded on the hypothesis that local linear regressions were able to capture CO_2 and CH_4 temporal evolution equally as well as quadratic linear regressions. The results derived from the temporal analysis point to different behaviour between day and night CO_2 and CH_4 measurements, with the highest mixing ratios during the night-time when atmospheric mixing

and turbulent processes are low. A seasonal pattern was also inferred for the study period for both gases, revealing summer minima, partially due to greater summertime photosynthesis as regards CO_2 and to maximum OH concentration during the summer as regards CH_4. A simpler cycle was found for CH_4, showing only a maximum for diurnal and nocturnal data in winter, partially due to the low presence of OH radicals. However, a different behaviour between diurnal and nocturnal data was revealed by CO_2 observations. As regards nocturnal CO_2 data, two maxima, one in spring and another in autumn, were reported. These two maxima were linked to an increase in rainfall which corresponded to a period of maximum vegetation growth, thus increasing respiration rates. For CO_2 daytime records, only the spring peak was detected. The mixing ratios of the abovementioned gases at the CIBA station were comparable to those at other background sites around the world. Increasing growth rates were obtained for both gases over the whole study period. The slight differences among mixing ratios at different sites may be mainly attributable to the impacts of anthropogenic emissions near the background sites and to regional atmospheric transport. Secondly, it should be considered that assessing the link between atmospheric mixing ratios and wind direction data can help to identify possible pollution sources, thereby giving additional information to the previous temporal patterns described. Unfortunately, the influence of urban plumes on the final measurements recorded at rural stations is an issue which has rarely been touched upon in detail. Thus, in order to provide a full understanding of the temporal patterns at the CIBA station, a fourth scientific paper considering CO_2 and CH_4 mixing ratio data measured at CIBA, surface wind direction data and back-trajectories at 500 m a.g.l. computed with the METEX model, was produced to analyse the impact of the Valladolid urban plume on the final mixing ratio measured at the station. The final south-westerly component of the urban mean back-trajectory, its longer time spent travelling over the Iberian Peninsula and its recirculation in the final 24 h before impacting the CIBA station, might result in more pollutants being dragged to the station. As a result, the highest CO_2 and CH_4 values were detected for southern sectors, showing what effect the Valladolid plume has on final CO_2 and CH_4 measurements. Finally, the results derived from the current thesis prove crucial in terms of understanding the processes that govern CO_2 and CH_4 trend and cycle evolution. Describing the gases in this way would enable more effective mitigation policies to be planned in order to achieve the goal of reducing the amount of greenhouse gases in the atmosphere.

Keywords: CO_2, CH_4, temporal patterns, rural background station, harmonic function, kernel functions, bandwidth, local regression functions, air mass modelling, METEX model.

1.2. Resumen

Desde la Revolución Industrial, las concentraciones de los gases de efecto invernadero han aumentado debido a diversas actividades antrópicas, provocando con ello el aumento de la temperatura media del planeta. La determinación de gases de efecto invernadero en estaciones de fondo es crucial para evaluar el impacto de las emisiones antropogénicas en la baja atmósfera. Sin embargo, estos estudios aún son escasos en estaciones de fondo. La presente tesis doctoral busca, en primer lugar, mejorar el conocimiento existente sobre la evolución de los dos principales gases de efecto invernadero (CO_2 y CH_4) en términos de tendencias, tasa de crecimiento y variaciones estacionales en la troposfera. En segundo lugar, se pretende analizar el efecto del penacho urbano de Valladolid en las concentraciones de CO_2 y CH_4 registradas en el Centro de Investigación de la Baja Atmósfera (CIBA). Para alcanzar este doble objetivo, se registraron las concentraciones en seco de CO_2 y CH_4 durante cinco años y medio (del 15 de octubre de 2010 al 29 de febrero de 2016) a 8,3 m. de altura mediante el empleo de un analizador de precisión, el Picarro G1301, en un emplazamiento rural remoto en la estación del CIBA en la meseta norte castellana. Este es el primer estudio realizado en la estación del CIBA con una base de datos tan amplia, tomada mediante un instrumento de alta precisión y diferenciando entre los datos diurnos y nocturnos. En primer lugar, a fin de analizar los patrones temporales, se destendenció y desestacionalizó la serie temporal para capturar la dinámica intrínseca de la serie temporal. Con el objetivo de describir con precisión los patrones temporales de CO_2 y CH_4 se llevaron a cabo tres amplios estudios en los que se emplearon diferentes funciones matemáticas. El empleo de diferentes funciones matemáticas permitió la detección de posibles sesgos causados por el método empleado, así como una comparación entre las funciones empleadas en términos de facilidad de uso, coste computacional y grado de ajuste de cada una de las funciones con los datos experimentales. El primer artículo empleó una ecuación armónica formada por un polinomio de tercer grado para expresar la tendencia y una serie de cuatro armónicos para expresar la evolución estacional de los datos. Cada uno de los armónicos constaba de una parte constante y una parte variable con el tiempo. El segundo artículo aplicó 6 funciones de kernel para analizar los patrones temporales del CO_2 y el CH_4. Las 6 funciones de kernel empleadas fueron: Epanechnikov, Gaussiana, cuártica, triangular, tricúbica y rectangular. Del mismo modo, esta segunda contribución propuso un método novedoso y sencillo para determinar simultáneamente los anchos de banda óptimos para analizar la tendencia y el ciclo estacional basado en gráficos de contorno en los que se emplean los valores de R^2 valores como estadístico robusto para la toma de decisiones. El tercer artículo se basó en la hipótesis de que las regresiones locales lineales eran capaces de capturar la evolución temporal del CO_2 y el CH_4 con la misma precisión que las regresiones locales cuadráticas. Los resultados

derivados de estas tres primeras contribuciones originales pusieron de manifiesto un comportamiento diferente entre las medidas diurnas y las nocturnas de CO_2 y el CH_4, obteniendo las máximas concentraciones durante la noche cuando los procesos turbulentos y de mezcla son mínimos debido a la estabilidad atmosférica en esta parte del día. En lo que respecta al ciclo estacional, las concentraciones mínimas se encontraron en verano debido a la actividad fotosintética en el caso del CO_2 y a la máxima concentración de OH en el caso del CH_4. De igual modo, cabe destacar que el ciclo estacional del CH_4 es más simple que el del CO_2, mostrando el mismo comportamiento para los datos diurnos y nocturnos, presentando un único máximo en invierno debido a la baja presencia de radicales OH en dicha estación. Sin embargo, las observaciones de CO_2 revelaron un comportamiento distinto entre la serie diurna y nocturna. En cuanto a la serie nocturna para el CO_2, se encontraron dos máximos, uno en primavera y otro en otoño. Estos dos máximos se vincularon al aumento de las precipitaciones en estas estaciones, lo que conllevó a un período de máximo crecimiento de la vegetación, aumentando con ello las tasas de respiración. Por su parte, la serie diurna del CO_2, sólo mostró un máximo en primavera. Cabe destacar que se obtuvieron tasas de crecimiento crecientes para ambos gases durante el período de estudio. Además, las concentraciones de ambos gases en la estación del CIBA fueron comparables a las de otras estaciones de fondo en otras partes del mundo. Las ligeras diferencias en las concentraciones del CO_2 y el CH_4 de la estación del CIBA con respecto a otras analizadas en la bibliografía se debieron principalmente a los impactos de las emisiones antropogénicas cercanas a las estaciones de medida y al transporte de masas de aire desde zonas más contaminadas. Finalmente, es importante evaluar la relación entre las concentraciones de CO_2 y el CH_4 atmosféricas en relación con la dirección del viento a fin de identificar posibles fuentes de contaminación, aportando información adicional a los patrones temporales ya descritos en las tres primeras contribuciones. Por tanto, la cuarta contribución original se centró en analizar la relación existente entre la dirección del viento en superficie y en altura (retrotrayectorias a 500 m. calculadas con el modelo METEX) con las concentraciones finales de CO_2 y CH_4 registradas en la estación del CIBA para analizar el efecto del penacho urbano de Valladolid en las concentraciones finales registradas. El componente suroeste de la retrotrayectoria media para los sectores urbanos en las últimas 24 horas antes del impactar en la estación, el mayor tiempo de transporte dentro de la Península Ibérica y el mayor factor de recirculación, supusieron un mayor arrastre de contaminantes hacia el CIBA. Como resultado, las mayores concentraciones de CO_2 y CH_4 se detectaron para los sectores sur poniendo de manifiesto el efecto del penacho urbano de Valladolid en las concentraciones finales. Por último, los resultados arrojados por la presente tesis doctoral ayudaron a comprender los procesos que gobiernan la tendencia y los ciclos estacionales del CO_2 y CH_4. Esta caracterización de ambos

gases pretende contribuir a la planificación de políticas de mitigación de cambio climático más efectivas para lograr el objetivo de reducir la concentración de gases de efecto invernadero en la atmósfera.

Palabras clave: CO_2, CH_4, patrones temporales, estación de fondo rural, función armónica, funciones kernel, ancho de banda, funciones de regresión local, modelado de masa de aire y modelo METEX.

2. Introduction

2.1. An overview

Over the last century, climate change has become a subject of great interest and is recognized as one of the major global challenges facing mankind in the 21st century (Almeida et al., 2017; Anderson et al., 2016; del Río et al., 2005; Hernández-Ceballos et al., 2016; IPCC, 2019). Climate change, and its impact on the earth's surface, together with the increase in greenhouse gases, radiation budget and changes in global temperatures, has increasingly attracted the attention of researchers in different areas as it has an important environmental, social and economic impact from a local to a global scale (del Río et al., 2005; Ramos et al., 2012). Some of the most devastating effects of climate change include warming in cities and their surroundings (urban heat island), desertification, loss of biodiversity (Espinosa et al., 2018; Miller et al., 2017), changing rainfall patterns or greater frequency of some extreme events (IPCC, 2019) such as wildfires (Halofsky et al., 2020). Moreover, climate change will also have adverse effects on livelihoods, food security, habitats, and land degradation (IPCC, 2019). Greenhouse gases from anthropogenic activities are the most significant driver of climate change to have been observed since the mid-20th century (IPCC, 2013). Due to the effects of climate change, over the last third of the twentieth century, an international awareness of the danger involved and of the need to take measures to prevent global warming has emerged. The following subsections briefly point out the most important international climate change instruments and agreements adopted with regard to regulating greenhouse gas emissions in an effort to tackle climate change.

2.1.1. International instruments and agreements for regulating greenhouse gas emissions

2.1.1.1. The Intergovernmental Panel on Climate Change (IPCC)

In 1988 the World Meteorological Organization (WMO) and the United Nations Environment Program (UNEP) created the Intergovernmental Panel on Climate Change (IPCC) to analyse the problem of global climate change. The IPCC is a group open to all members of the United Nations and WMO (IPCC, 2020a). The function of the IPCC is not to conduct its own research but to analyse, in a comprehensive, objective, open and transparent way, the relevant scientific, technical and socioeconomic information required to understand the scientific elements involved in climate change caused by human activities, its possible repercussions and the possibilities of attenuation and/or adaptation (IPCC, 2020a). In addition, through their evaluations, the IPCC seeks to identify the strength of scientific agreement in different areas and indicates where further research is needed. The IPCC is made up of three different working

groups. Working Group III is responsible for assessing different options for limiting greenhouse gas emissions to mitigate climate change.

In 1990, the IPCC published its First Assessment Report and confirmed the scientific elements that raised concern about climate change. It pointed out the need to reduce greenhouse gas (GHG) emissions by 67% by 2025 in order to reach a global emissions reduction of 20% compared to 1985 levels (IPCC, 1992). Following the First IPCC Report, the United Nations General Assembly decided to prepare a Framework Convention on Climate Change in 1992 (IPCC, 1995). This United Nations Framework Convention on Climate Change (UNFCCC) came into force legally in 1994 and provided the starting point for the Kyoto Protocol. The main goal of the UNFCCC was to stabilise the greenhouse gas mixing ratio amount in order to avoid or limit anthropogenic interference in the climate system, ensure food production and allow economic development to continue in a sustainable manner. The supreme body of the United Nations Framework Convention on Climate Change is the Conferences of the Parties (COP), comprising all the state parties who meet annually at world conferences in order to take decisions aimed at achieving the objectives of tackling climate change. The first COP was held in 1995 in Berlin with the aim of initiating negotiations to reduce emissions beyond 2000 through quantitative objectives and specific deadlines (Roberts, 2016). To date, 25 COPs have been held, with the last having taken place in December 2019 in Spain.

In 1995, the Second Assessment Report provided scientific material for the Kyoto Protocol negotiations derived from the Convention on Climate Change held in 1992 in Brazil (IPCC, 1995).

In 2001, the Third Assessment Report highlighted the existence of climate change and its main impacts and consequences, providing scientific and technical issues that would prove useful for implementing effective policy design (IPCC, 2001).

In 2007, the Fourth Assessment Report went a step further by stating that climate system warming was indisputable and was mainly due to the increased concentration of greenhouse gases as a result of human activities mainly linked to the use of fossil fuels, changes in land use and some agricultural practices. Moreover, the Fourth Report revealed a growing trend in extreme events and stated that temperature increases, heat waves, and heavy rainfall events were becoming increasingly frequent (IPCC, 2007).

In 2014, the Fifth Assessment Report reported that anthropogenic GHG emissions had reached their highest ever levels (IPCC, 2014).

The IPCC is currently working on the Sixth Assessment Report, which will be finished in the first half of 2022. In this report a refinement of the methodology employed in the previous IPCC reports is expected (IPCC, 2020b).

2.1.1.2. International agreements

The Kyoto Protocol was the first legal international agreement linked to the regulation of greenhouse gas emissions. The justificatory arguments of the Kyoto Protocol began at the third conference of the parties (COP3) of the United Nations Framework Convention on Climate Change in Kyoto (Japan) in 1997, ending at Buenos Aires in 2004 (COP10) (Lövbrand, 2009; Roberts, 2016). This international agreement sought a reduction in greenhouse gas emissions in industrialized countries (Roberts, 2016). The Kyoto Protocol was initially in effect from 2008 to 2012 (Klimenko et al., 2019; Roberts, 2016). It was the first binding agreement on the fight against climate change, and established legally binding emission reduction targets. In November 2009, the Protocol was ratified by 192 countries which jointly account for 86.8% of all greenhouse gas emissions (Klimenko et al., 2019). In it, industrialized countries committed to reduce greenhouse gas emissions by 5.2% before 2012 compared to 1990 levels (Klimenko et al., 2019). Finally, a reduction of around 9.6% in greenhouse emissions from 2008 to 2012 compared to 1990 levels for most countries was achieved, virtually twice the initial amount (Klimenko et al., 2019). As regards EU countries, a reduction in GHG emissions was observed as a result of economic restructuring in eastern Europe in the 1990s (Balsalobre et al., 2015). However, outside EU borders the Protocol had little impact since the United States failed to ratify it and Canada abandoned it at the Durban conference in 2011 (COP17) (Corti, 2017; Klimenko et al., 2019). Furthermore, the Protocol left out the developing countries. In general, virtually only Australia, New Zealand and Japan joined the European model, together with Russia's late incorporation, albeit with doubtful long-term effects (Corti, 2017).

The Kyoto Protocol was initially expected to end in 2012. Hence the 15th Conference of the Parties (COP 15) of the United Nations Framework Convention on Climate Change (UNFCCC) held in Copenhagen in 2009 sought to reach an international agreement that would establish a framework to replace the Kyoto Protocol. Unfortunately, the Copenhagen Accord did not enable a new agreement to reduce emissions to be reached after 2012 (Corti, 2017; Roberts, 2016). The main reason for the failure of the Copenhagen Accord was the 2008 global financial crisis which undermined economies as well as confidence in development models, added to

which emerging countries were not willing to adopt a scheme that could jeopardize their growth (Corti, 2017; Griffiths et al., 2020; Hu et al., 2020; Klimenko et al., 2019). However, two important advances were made at the COP15. Firstly, it showed the need to limit the increase in global temperature to 2ºC from pre-industrial levels as well as the need to limit global emissions based on the results to come out of the Fourth Assessment Report of the IPCC (IPCC, 2007). Secondly, many countries signed up to the agreement and developing countries adopted an active role in the negotiations by making minor commitments to reduce greenhouse gas emissions (Corti, 2017). Another notable facet of the Copenhagen Accord was the fact that political agreement was reached between key world leaders: the United States, China, India, Brazil, and South Africa, especially the first two with a decline in European Union leadership (Corti, 2017). However, the main developing countries, such as China or India, did not accept measurement, information and verification of their emissions by third parties who were seeking increased transparency.

In 2011, the COP17 held in Durban (South Africa), resulted in the decision to replace the Kyoto Protocol with another protocol designed to establish concrete actions to combat climate change (Roberts, 2016). A working group was formed to develop the text of the global agreement that served as the basis for the agreement which would ultimately be signed at the Paris conference. In the frame of the COP17, Europe adopted a more neutral stance, mediating between the two great powers: the US and China, and providing concrete action measures (Corti, 2017).

In 2012, the Qatar Conference of the Parties (COP18) established a second period for the Kyoto Protocol, covering the 2013-2020 period (Roberts, 2016).

In 2013, the Warsaw Conference of the Parties (COP19) presented the updated draft of the international agreement that would be worked on at the 2015 Paris Conference (COP21) (Lörcher et al., 2015).

In 2015, the 21st Conference of the Parties (COP 21) of the United Nations Framework on Climate Change (UNFCCC) took place in Paris, ending with the adoption of the Paris Agreement by the 195 UNFCCC countries (Boffino et al., 2019). The Paris Agreement establishes the global framework for combating climate change from 2020, promoting a transition towards a low-emission economy in the fight against climate change (Boffino et al., 2019; Pauw et al., 2019). This agreement establishes a plan to reduce emissions of CO_2 and other greenhouse gases, aiming to keep global temperature increases to below 2ºC relative to

pre-industrial levels and to even pursue efforts to limit temperature increases to 1.5°C above pre-industrial levels (Anderson et al., 2016; Arioli et al., 2020). To date, 178 countries have ratified the agreement (Simsek et al., 2019). It is worth noting that China, one of the major emitters (Chen et al., 2020; Guo et al., 2020), ratified the agreement that set the goal of reducing carbon emissions per unit of the Gross Domestic Product by 60-65% compared to 2005 levels (Morris et al., 2019). The European Union (which accounts for 7.57% of global emissions) ratified the agreement, with the aim of reducing 2005 levels by 43% before 2030 (Parry, 2020). As regards Spain, a reduction in its emissions by around 20-30% from 2005 emissions was adopted, with special emphasis on the transport and building sector (Parry, 2020). The Paris Agreement came into force in 2020 after the end of the second period of the Kyoto Protocol (Roberts, 2016).

2.1.1.3. International agreements in the framework of the European Union

The European Union has already proposed measures through the Energy Roadmap 2050 document to reduce greenhouse gas emissions by at least 40% (Đozić et al., 2019), although it actually aims to reduce them to 80–95% below 1990 levels by 2050 (Energy Roadmap 2050, 2012; Rečka et al., 2017). The Energy Roadmap 2050 document of the European Commission aims to promote economically cost-effective scenarios to adapt the European Union's economy to a competitive and sustainable low-carbon economy model while ensuring the security of energy supply (Đozić et al., 2019; Energy Roadmap 2050, 2012). As stated in the Energy Roadmap 2050 (2012) document, solutions to curb greenhouse gas emissions need many years of preparation if they are to begin to be fruitful, such that decision-making should be implemented quickly. In this sense, the Energy Roadmap 2050 document establishes the need for concrete strategies to be established after 2020 in order to reach reduction and decarbonisation objectives.

2.1.2. Global greenhouse gas emissions

The link between greenhouse gases and climate warming has caught the attention of scientists, politicians and the general public, via the well-known ‘‘greenhouse effect’’ in which molecules of gas in the atmosphere intercept infrared radiation from the Earth's surface and part of the absorbed energy is re-radiated back to the surface, increasing the Earth’s mean temperature (Anderson et al., 2016). This process is schematically shown in Figure 1.

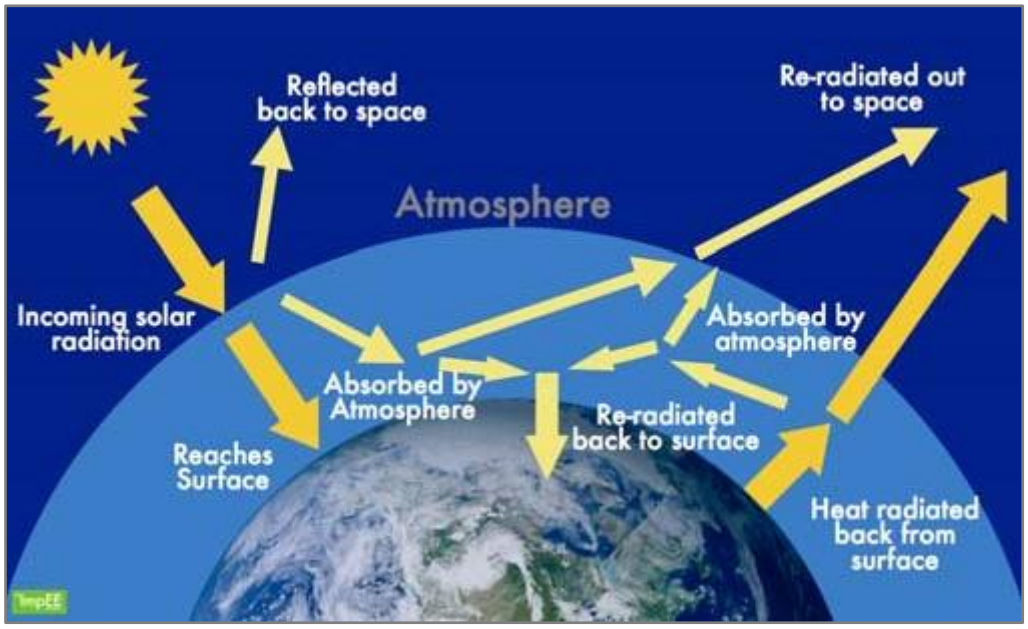

Figure 1. Distribution of energy from the Sun to the Earth (Riza et al., 2011).

The origin of climate change is found in the mass emission into the atmosphere of so-called greenhouse gases (GHG). The Intergovernmental Panel on Climate Change (IPCC) points to anthropogenic emissions as the main cause of the climate variations observed in recent decades. Climate change is a global problem of exponential nature (occurring in accordance with the intensity of human activities and their emissions) and is persistent since, even if measures were implemented today, it would take many decades to reduce the vast amount of GHG in the atmosphere. At a global scale, the key greenhouse gases emitted by human activities are carbon dioxide (CO_2), methane (CH_4), nitrous oxide (N_2O) and fluorinated gases (F-gases) (Hartmann, 1994; IPCC, 2014; Jiménez et al., 2015). Figure 2 depicts the percentage of anthropogenic GHG gases from 1970 to 2010.

As can be seen in Figure 2, the main GHG contributor is CO_2 followed by CH_4. Both gases together contributed over 90% of all GHG emissions in the atmosphere for the period 1970-2010 (IPCC, 2014). It is important to point out that during the 1980s, CFCs contributed around 25% of climate forcing (Hartmann, 1994). However, important restrictions were adopted through the Montreal Protocol to reduce the amount of CFCs in the atmosphere in order to preserve the ozone layer. This led to a decrease in CFCs but reinforced CO_2 contribution. Furthermore, CO_2 and CH_4 are considered to be long-lived gases in the atmosphere (IPCC, 2007), which means that they need a long time to achieve a new equilibrium or steady state in response to a perturbation (i.e. their time of residence) (Hartmann, 1994). However, the difference in terms of years for both gases should be noted, since time residence for CO_2 is in the range of 50-200 years, whereas time residence for CH_4 is around 10 years (Beck et al.,

2018; Fiore et al., 2015; Hartmann, 1994; Hill et al., 2016; Lee et al., 2020; Prather et al., 2012). Furthermore, in recent decades, there has been growing scientific consensus that the increase in the concentrations of several key long-lived greenhouse gases is contributing to an overall global warming effect via the radiative forcing effect (IPCC, 2014; Jiménez et al., 2015; Sorribas et al., 2019). CO_2 and CH_4 are the largest radiative forcing contributors, accounting for 69% (2.044 Wm^{-2}) and 18% (0.512 Wm^{-2}), respectively, of total radiative forcing by all long-lived greenhouse gases in 2018 (NOAA, 2020b). It should be remembered that the effects of GHG emissions on the energy balance of the atmosphere are cumulative over their atmospheric lifetimes (Rella et al., 2013). Due to lower CH_4 lifetime in the atmosphere, a quicker stabilization or reduction in its emissions, compared to CO_2, is possible (Saunois et al., 2020).

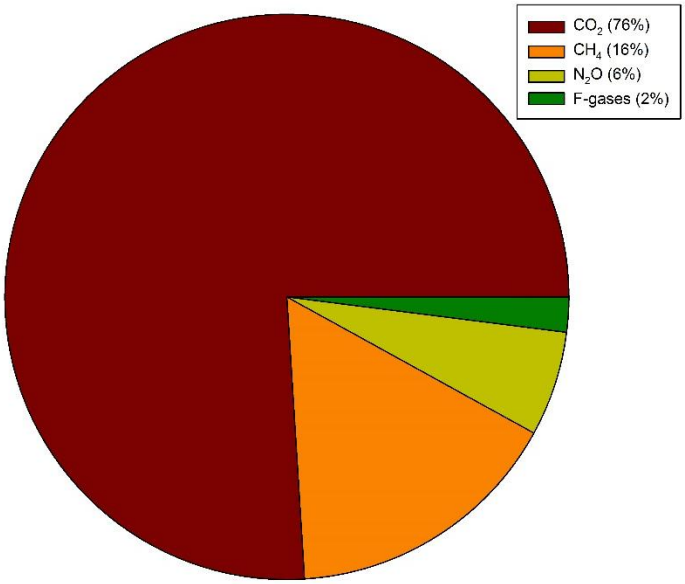

Figure 2. Anthropogenic greenhouse gases between 1970-2010 (IPCC, 2014).

As regards global emissions by economic sector, those which lead to major impacts are shown in Figure 3 and are the following (IPCC, 2014):

- Electricity and Heat Production: the burning of coal, natural gas, and oil for electricity and heat is the largest single source of global greenhouse gas emissions.
- Agriculture, Forestry, and other Land Use (AFOLU): cultivation of crops, livestock and deforestation are the main emissions from the AFOLU sector. This estimate does not include the CO_2 that ecosystems remove from the atmosphere by sequestering carbon in biomass, dead organic matter, and soils.
- Industry: primarily fossil fuels burned in industry for energy. However, emissions from chemical, metallurgical, and mineral transformation processes not associated with

energy consumption, and emissions from waste management activities are also included.

- Transportation: involves fossil fuels burned for road, rail, air, and marine transportation. Almost all of the world's transportation energy comes from petroleum-based fuels, mainly gasoline and diesel.
- Buildings: refers to onsite energy generation and burning fuels for heating in buildings or cooking in homes.
- Other Energy: refers to all emissions from the energy sector which are not directly associated with electricity or heat production, such as fuel extraction, refining, processing, and transportation.

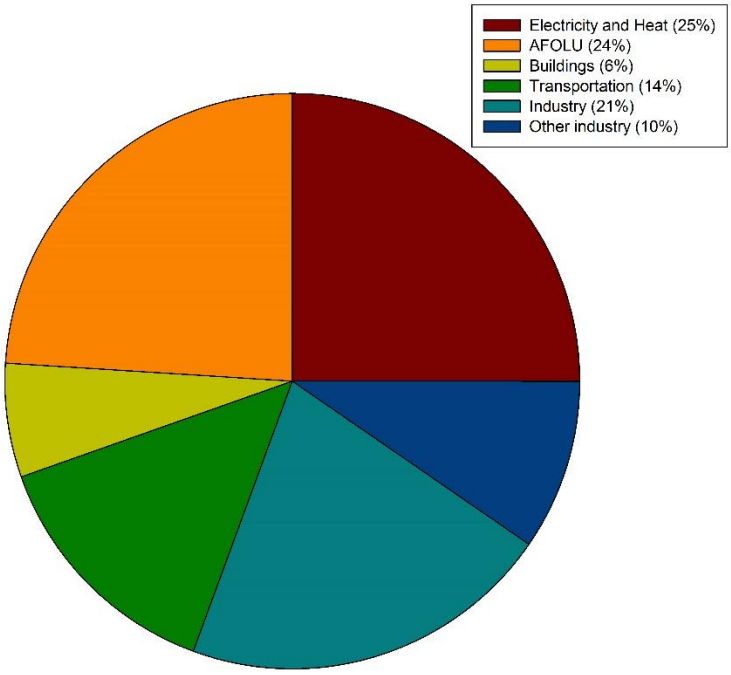

Figure 3. Anthropogenic GHG emissions by economic sectors in 2010 (IPCC, 2014).

The main greenhouse gas emitting countries are China, the United States, the European Union and India, as shown in Figure 4. Moreover, as stated by Agrawal (2019), global greenhouse gas emissions reached approximately 37.15 billion tonnes of CO_2 in 2018.

As regards European Union (EU27) emissions (Figure 5), Germany, France, Italy, Poland, and Spain (which also reflects GHG contribution from Andorra) are the main GHG emitting countries.

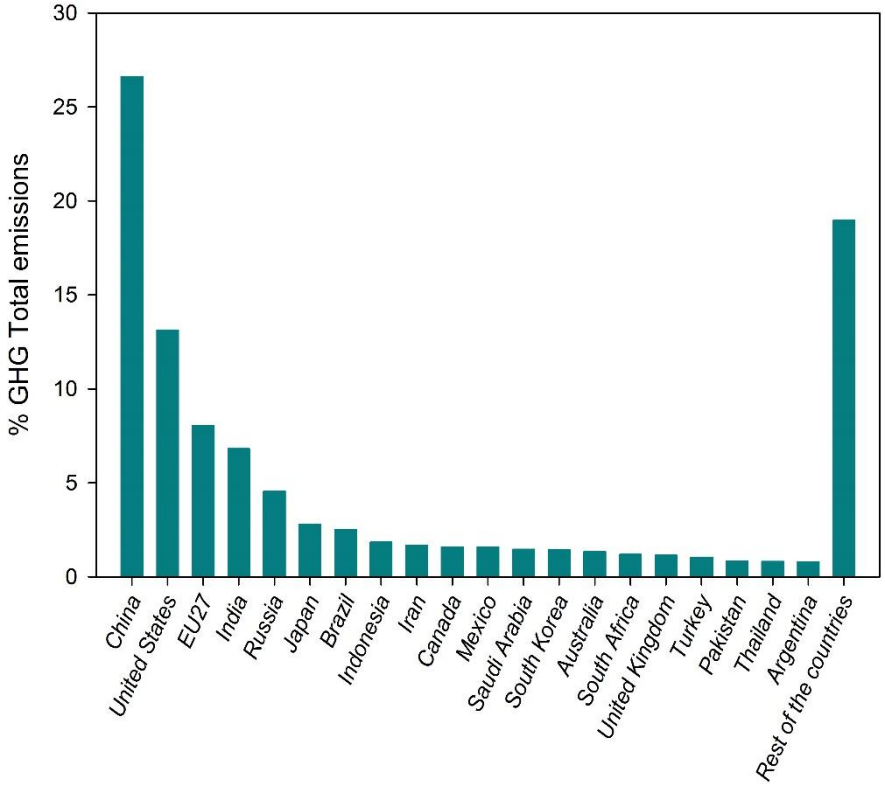

Figure 4. Percentage of total emissions of greenhouse gases by countries at a global scale referring to 2015 data from EDGAR (2020).

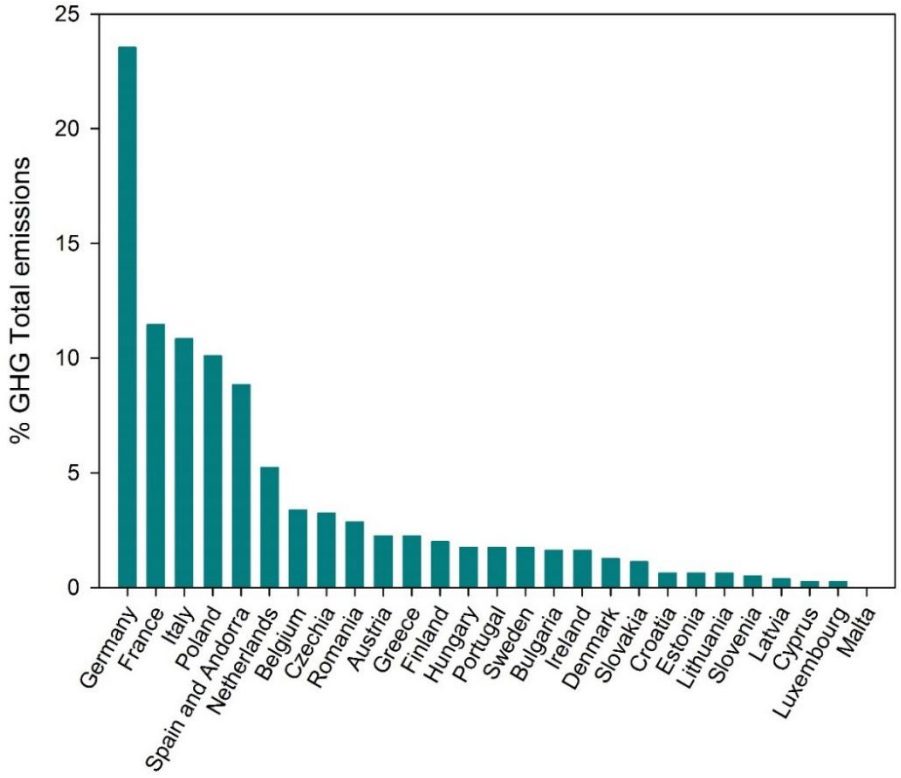

Figure 5. Percentage of total emissions of greenhouse gases for EU countries referring to 2015 data from EDGAR (2020).

Since CO_2 and CH_4, are the two most important greenhouse gases in terms of abundance and radiative forcing, understanding and quantifying their mixing ratios at different scales is crucial for assessing realistic pathways to mitigate climate change (Curcoll et al., 2019; Jiménez et al., 2015; Sauonis et al., 2020). Hence, the two next sections are focused on pointing out the main characteristics of their cycles and their mixing ratio evolution over time.

2.2. CO_2

2.2.1. The CO_2 cycle

The major anthropogenic CO_2 sources are global fossil fuel emissions (E_{FF}) which include the combustion of fossil fuels through a wide range of activities (e.g. transport, the heating and cooling industry, fossil fuel industry and natural gas flaring), the production of cement and other industrial emissions (Friedlingstein et al., 2019). The second most important CO_2 sources are emissions from land use, land use change and forestry activities (E_{LUC}) (Friedlingstein et al., 2019; Li et al., 2014). E_{LUC} emissions reflect the net sum of emissions (e.g. deforestation, land clearing for agriculture, degradation of soils) and removals (e.g. reforestation) due to anthropogenic activities (Friedlingstein et al., 2019). As regards the main CO_2 sinks, prominent are terrestrial CO_2 sinks (S_{LAND}), which refers to some natural CO_2 reservoirs (e.g. soils, plants or permafrost) (Friedlingstein et al., 2019). The second most important natural CO_2 sinks are the oceans (S_{OCEAN}) (Friedlingstein et al., 2019). Figure 6 depicts the main CO_2 global sources and sinks.

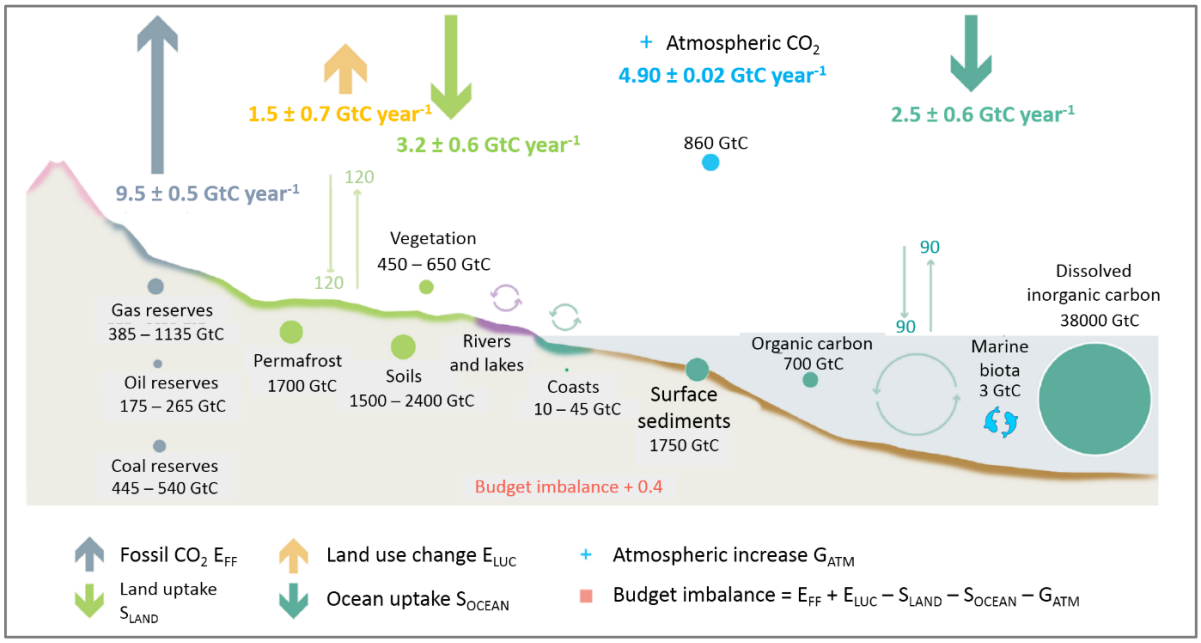

Figure 6. Schematic representation of CO_2 sources and sinks for the most recent available decade data (2009-2018) (modified from Friedlingstein et al., 2019).

Accurate assessment of CO_2 emissions and distribution in the atmosphere is important vis-à-vis gaining a better understanding of the global carbon cycle in order to support the development of climate policies and to mitigate and tackle climate change (Curcoll et al., 2019; Le Quéré et al., 2016). However, as many authors have pointed out (e.g. Bergamaschi et al., 2010; Ciais et al., 2000; Hase et al., 2015; Hu et al., 2018) the distribution of CO_2, as well as its sources and sinks, is still poorly constrained at a regional scale (Curcoll et al., 2019). Hence, as stated by Sreenivas et al. (2016), atmospheric CO_2 measurements are crucial in order to understand the carbon cycle.

2.2.2. The history of measuring CO_2

The first relevant scientific contribution as regards climate change was proposed by the mathematician and physician Joseph Fourier in 1827, who established that the Earth was getting warmer because the atmosphere was trapping heat as if under a pane of glass (Anderson et al., 2016; Weart, 1997). This process is currently well known as the "greenhouse effect". At this time, Fourier considered water vapour to be the main gas responsible for this warming process. However, in 1859 the Irish physician John Tyndall found that other gases, such as methane and carbon dioxide, also block infrared radiation (Anderson et al., 2016; Fleming, 2000; Weart, 1997). The geologist Arvid Högbom pointed out in 1894 that human activities were adding CO_2 to the atmosphere at a rate roughly comparable to natural geochemical processes (AIP, 2020).

Högbom's research provided the physician Arrhenius with a starting point to speculate in his pioneering work of 1896 about the possibility of a society releasing higher quantities of carbon dioxide that would increase the global warming effect (Hawkins et al., 2013; Weart, 1997). Arrhenius conducted tedious and time-expensive calculations of how carbon dioxide intercepted radiation in the atmosphere (Anderson et al., 2016; Fleming, 2000). Although Arrhenius could only make a rough estimation of CO_2 feedback effects with the available data, according to his calculations, doubling the amount of carbon dioxide would raise the planet's average surface temperature by around 5-6°C (Anderson et al., 2016; Weart, 1997). In this sense, Arrhenius' work proved to be crucial in terms of pointing to the possible effect of increasing amounts of CO_2 in the atmosphere (Weart, 2006). Arrhenius's work served as a starting point for Chrowder Chamberlin who, in 1896, stated that the level of CO_2 in the atmosphere changes over time and that considering these dynamics of the carbon cycle influences the climate (Fleming, 2000; Weart, 2006). Nevertheless, many authors cast doubt on the existence of global warming due to an increase in the CO_2 mixing ratio abundance in the atmosphere. For example, the Swedish physicist Knut Ångström who, in 1990, measured

the passage of infrared radiation through a tube filled with carbon dioxide, concluded that adding or reducing the quantity of carbon dioxide in the tube barely altered the amount of radiation that got through the tube. Furthermore, the conviction that the Earth automatically regulated itself by absorbing these gases through the oceans and/or vegetation was also an important reason to deny the greenhouse effect (AIP, 2020). Such was the line taken by the mathematician Lotka (1924) who considered the sea as a vast equalizer able to absorb up to 95% of all the carbon dioxide in the atmosphere, such that fluctuations could easily be reduced (Weart, 1997).

However, some scientists disagreed with the view that changes in CO_2 would have no effect on climate, which encouraged them to carry out studies to demonstrate this. In 1931, the physician O. Hulburt conducted tedious calculations which supported Arrhenius's estimation that doubling (or halving) CO_2 would bring an increase (decrease) of around 4°C (AIP, 2020). In 1938, the engineer Stewart Callendar analysed 147 land-based stations to rebuild global temperature series for different regions for around 50 years, showing that the Earth's land surface was warming due to manmade burning of fossil fuels, due to the so-called "Callendar Effect" (Anderson et al., 2016; Hawkins et al., 2013; Weart, 2006). Callendar suggested that the production of carbon dioxide by the combustion of fossil fuels was largely responsible for climate change, reviving interest in the issue of climate change and its link to CO_2 (Hawkins et al., 2013).

The vastly improved techniques which emerged in the 1940s enabled a revision of the old measurements with gases in a tube carried out by Ångström (Weart, 1997). It should be pointed out that in the old spectrographs used by Ångström, the bands of water vapour and carbon dioxide overlap (AIP, 2020). However, Hulburt and Callendar found that at low pressure and temperature, CO_2 and H_2O absorption lines do not exactly overlap but that there were two sets of narrow lines where radiation can get through (Weart, 1997). Scientists therefore considered it important to calculate absorption for radiation passing through the atmosphere in each layer and not as a whole (Weart, 1997).

The idea that CO_2 from human activity could never become a problem was overturned even further during the 1950s by a series of costly observations. In 1952, the theoretical physician Lewis D. Kaplan conducted extensive numerical computations with digital computers, pointing out that adding more CO_2 to the upper atmosphere could change the balance of radiation. In 1955, the theoretical physicist Gilbert Plass's calculations showed that adding carbon dioxide to the atmosphere would increase the infrared radiation intercepted (Weart, 2006). However,

in 1955, the chemist Hans Suess reported an increase of around only one percent of fossil carbon in the atmosphere by analysing wood trees grown over the past century, concluding that oceans were taking up most of the carbon that came from burning fossil fuels (Weart, 1997). The matter would not rest there, thanks in particular to Roger Revelle, director of the Scripps Institute of Oceanography in California who had spent his whole career studying the chemistry of the oceans (Munk, 1997). Revelle stated that seas were not able to absorb all the carbon dioxide in the atmosphere (Weart, 2006). Suess and Revelle studied how carbon moves through the air, ocean, minerals, soils, and living organisms in order to determine how much of the CO_2 produced from fossil fuels was absorbed by oceans or vegetation (Weart, 1997). Measurements of radioactive carbon travel finally showed that oceans were not able to absorb all the carbon dioxide that human industry was pouring out (Weart, 1997).

By the mid-1950s, researchers felt that it was important to measure the concentration of CO_2 in the atmosphere far more accurately. In addition, new funding became available in connection with the International Geophysical Year (1958), allowing Revelle and Suess to commence a major measurement programme aimed at establishing baseline CO_2 values around the world, and enabling these values to be checked over time (Weart, 1997). However, the programme needed costly and precise measurements collected at background sites far from disturbances. Charles Keeling was the geochemist responsible for starting the programme in 1958, measuring CO_2 in the pristine air of Antarctica and at the top of the Mauna Loa volcano in Hawaii (Weart, 1997). Due to the lack of funds the Antarctic station was closed, but Keeling managed to keep the Mauna Loa measurements going (Weart, 1997). In 1960, with only two full years of Mauna Loa data collected, a regular seasonal cycle was already evident, showing how the planet breathes in the Northern Hemisphere (Keeling, 2008). The record documented a global rising trend attributable to the burning of fossil fuels worldwide (Keeling, 2008) and provided well-known evidence of the greenhouse effect (Weart, 1997). By the early 1960s, many scientists had become seriously concerned that warming might not just be a moderate natural cycle but the onset of an abrupt rise (Weart, 1997). Keeling's curve, jagged but inexorably rising, was soon widely cited by scientific review panels and science journalists (Keeling, 2008; Marx et al., 2017). Keeling therefore heralded both the end and the beginning in the influence of increasing CO_2 and its effect on climate change.

2.2.3. CO_2 mixing ratio evolution over time

The data collected from Keeling's measurement programme is the longest continuous record of direct atmospheric CO_2 in the world and provided compelling evidence that the concentration of CO_2 in the atmosphere was rising (Keeling, 2008). Apart from the

measurements collected at Mauna Loa by Keeling from May 1958, NOAA started its own CO_2 measurements in May 1974, running parallel with those made by Scripps (NOAA, 2020c). A global average value is obtained for a specific time interval by fitting a smoothed curve as a function of time to each observation station. CO_2 mole fraction is expressed as parts per million (ppm), indicating that one out of every million molecules in an air-dry sample is CO_2. Figure 7 reflects the CO_2 mixing ratio evolution over time from the last glacial period to the present time, giving also a prediction for two future periods.

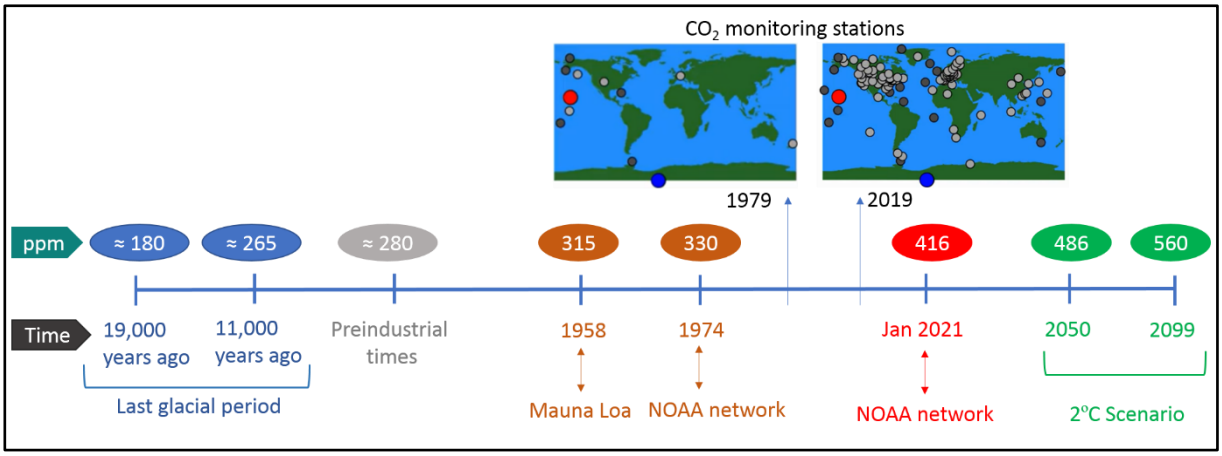

Figure 7. CO_2 mixing ratio evolution over time (data from Da et al., 2019; Keeling, 2007; NOAA, 2020a; c; d; Visconti, 2016).

2.3. CH_4

2.3.1. The CH_4 cycle

As already mentioned, reducing CH_4 emissions is an effective option for climate change mitigation, especially on decadal timescales (Saunois et al., 2020). In order to better understand the CH_4 cycle, Figure 8 shows the main sources and sinks for the 2008-2017 decade in accordance with the most recent global methane budget data (Sauonis et al., 2020).

Global anthropogenic CH_4 sources are in the range of 50-65% (Sauonis et al., 2020), with around two thirds originating from the Northern Hemisphere (Lelieveld, 2006). The main anthropogenic CH_4 sources include fermentation in livestock, manure management, waste water treatment, landfills, gas, coal mining (Sauonis et al., 2020), and biomass burning when incomplete combustion occurs (Sánchez et al., 2014). The main natural CH_4 sources are wetlands (Lee et al., 2020), peatlands, wild animals, digestion processes in termites, microorganisms living in the oceans, forest fires, CH_4 carbohydrates and permafrost (Saunois et al., 2020). It is important to bear in mind that permafrost can be exposed to either aerobic or anaerobic soil conditions, which determine the form (CO_2 and CH_4) and magnitude of carbon

released into the atmosphere (Song et al., 2020). Although many scientific studies point out that greenhouse gas production of permafrost under aerobic conditions is higher (producing CO_2), the importance of CH_4 production in anaerobic conditions vis-à-vis the climate forcing of greenhouse gases is also very important, as highlighted by Knoblauch et al. (2018) (Song et al., 2020). Oxidation of CH_4 by OH radicals in the troposphere is the major sink and accounts for 90% of CH_4 loss in the atmosphere (Beck et al., 2018; Fang et al., 2013).

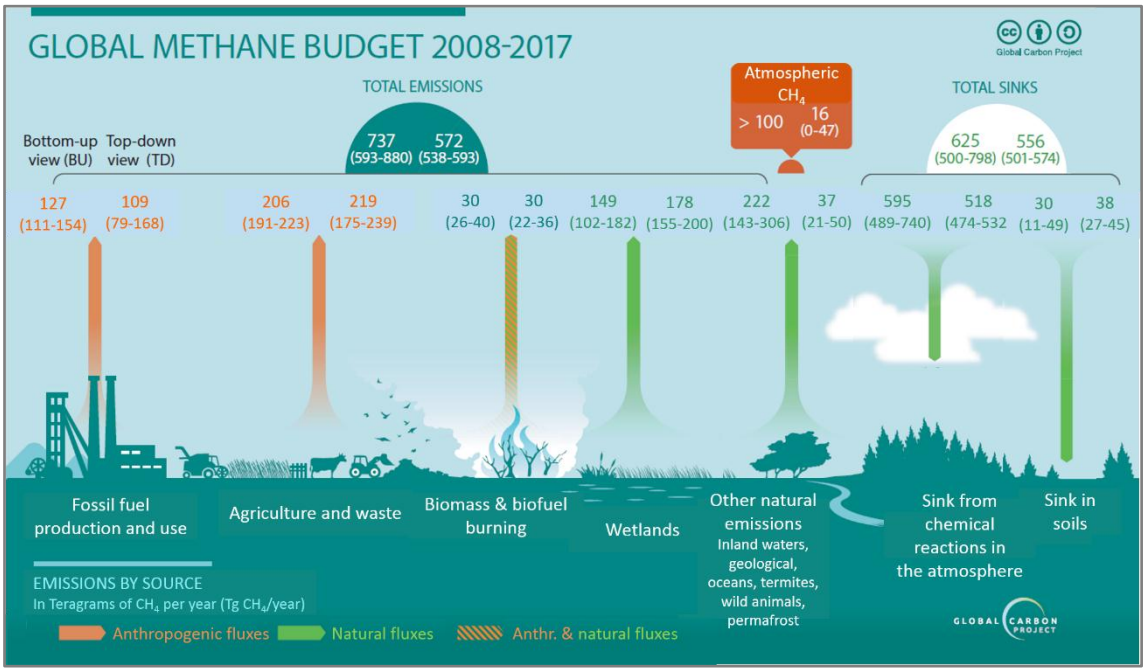

Figure 8. Schematic representation of CH_4 sources and sinks for the most recently available decade data (2008-2017) (modified from Saunois et al., 2020).

It should be pointed out that there is still considerable debate about the individual contributions of CH_4 sources and their variability, which is evidenced by the mismatch of bottom-up and top-down estimates of total CH_4 emissions, as reflected in Figure 8 (Beck et al., 2018). To address this topic, new research should be encouraged at different scales so as to improve and update the global methane budget (Sauonis et al., 2020).

2.3.2. The history of measuring CH_4

The Global Monitoring Division of NOAA's Earth System Research Laboratory started measuring the CH_4 mixing ratio in 1983 at a globally distributed network of air sampling sites (Dlugokencky et al., 1994). A global average is constructed exactly in the same way as is done with CO_2 measurements (NOAA, 2020e). Prior to 1983, methane levels were obtained from ice core data from Antarctica (2º Institute, 2020).

2.3.3. CH_4 mixing ratio evolution over time

Figure 9 reflects CH_4 mixing ratio evolution over time from the last glacial period to the present day, and also gives a prediction for 2030. CH_4 is expressed as parts per billion (ppb), which indicates that one out of every billion molecules in an air-dry sample is CH_4.

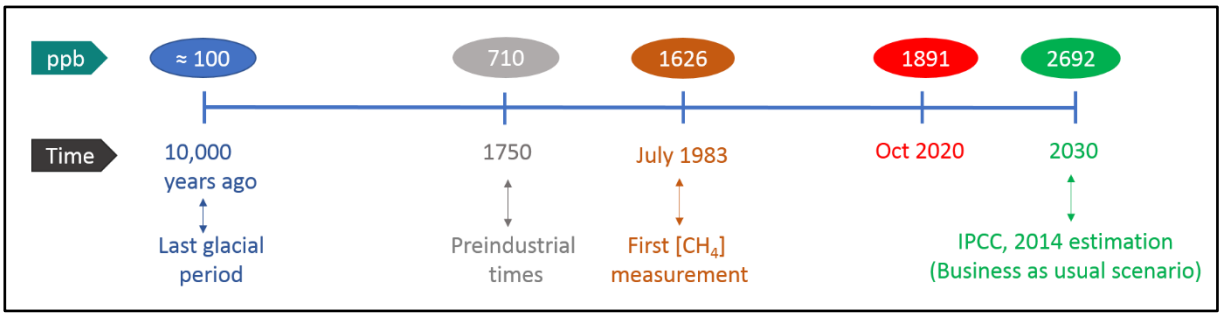

Figure 9. CH_4 mixing ratio evolution over time (data from Beck et al., 2018; Ganesan et al., 2019; IPCC, 2013; NOAA, 2020e).

As can be seen from Figure 9, CH_4 mixing ratio values during the Holocene, the last inter-glacial period, were around 100 ppb, and have increased rapidly due to industrialization (Beck et al., 2018; Ganesan et al., 2019). Due to human influence on the Earth's system, current CH_4 levels in the atmosphere have increased by a factor of around 2.5 relative to preindustrial levels (Beck et al., 2018) and are expected to reach almost 2700 ppb in ten years' time if the current energy scenario continues (IPCC, 2014).

2.4. The importance of accurate CO_2 and CH_4 mixing ratio measurements

CO_2 and CH_4 mixing ratios should be measured using a common scale in order to avoid, or at least reduce, bias in outputs. For this purpose, the World Meteorological Organization (WMO) established requirements for the inter-laboratory compatibility of atmospheric greenhouse gas measurements, correcting the effect of water vapour for obtaining dry samples (Reum et al., 2019). Furthermore, the characteristics of greenhouse gases at regional background sites are crucial for assessing the impact of anthropogenic emissions, ecosystems and climate change on the atmospheric environment (Cheng et al., 2019) since they are relatively well isolated from major urban and industrial emissions.

2.4.1. The importance of drying the samples

CO_2 and CH_4 are both reported as dry air mole fraction defined as the number of molecules of CO_2 or CH_4, respectively, divided by the number of all molecules in air, including CO_2 and CH_4, after water vapour has been removed (Yver Kwok et al., 2015; Rella et al., 2013). In order to

achieve the goal of inter-laboratory compatibility established by the Global Atmosphere Watch programme of the World Meteorological Organisation (WMO/GAW) (i.e. accuracy of ± 0.1 ppm for CO_2 and ± 2 ppb for CH_4 measurements) it is necessary to dry the samples to very low levels of water vapour (i.e. dew point <−25 ºC) (Rella et al., 2013). However, when water vapour is removed from a sample of ambient air, via evaporation or condensation processes, two major drawbacks emerge. First, it should be taken into account that the mole fraction of the other gases in the sample is also affected via dilution by water vapour (Rella et al., 2013). Second, drying the sample gas to low levels of water vapour can be expensive and time-consuming.

Traditional methods for measuring CO_2 and CH_4 mole fractions of greenhouse gases consist of non-dispersive infrared (NDIR) spectroscopy for CO_2 and gas chromatography for CH_4 (Rella et al., 2013; Schmidt et al., 2014; Yver Kwok et al., 2015). However, both methods evidence major drawbacks such as the frequent calibrations required to obtain high-precision measurements and the high level of expertise needed when employing the gas chromatography methodology (Yver Kwok et al., 2015). Fortunately, advances in optical measurement techniques, in particular cavity ring down spectroscopy (CRDS), have led to the development of greenhouse gas analysers capable of simultaneous measuring CO_2, CH_4 and H_2O. Unlike non-dispersive infrared (NDIR) spectroscopy and gas chromatography techniques, which suffered from significant uncorrected interference from water vapour, CRDS instruments allow for accurate greenhouse gas measurements able to meet WMO/GAW inter-laboratory compatibility goals (Rella et al., 2013). CRDS analysers can directly measure the water vapour content of the air at the same time as carbon dioxide and methane are also measured. Thus, the dry mixing ratios of CO_2 and CH_4 can be directly quantified by correcting the H_2O content in the air (Rella et al., 2013). Other notable features of cavity ring down spectroscopy technology are its infrequent calibration as well as low maintenance and few consumables required compared to gas chromatography and NDIR sensors (Yver Kwok et al., 2015).

For about 10 years, CRDS analysers have been developed and commercialized by a few companies (Crosson, 2008; Peltola et al., 2014). The Picarro G1301 model, which is the equipment used in the current study, was the first commercial instrument of CRDS sensors (Crosson, 2008). CRDS sensors are based on an optical technology in which direct measurement of infrared absorption loss in a sample cell is used to quantify the mole fraction of the gas (Rella et al., 2013). The CRDS technique is based on measurements of time not of absorbance. Thus, any fluctuations in laser intensity have no effect on the measurement,

unlike conventional spectrometers and gas analysers. More details concerning the CRDS techniques are given in the material and methods section.

2.4.2. Background stations

Background stations are those located in remote areas, far from highly populated areas and relatively well isolated from major urban and industrial emissions (Calvo et al., 2012). Moreover, road traffic is moderate in surrounding areas. Background stations experience a well-mixed atmosphere (van der Wal et al., 1997), representing atmospheric conditions under a specific climate pattern, vegetation composition and economic area (Cheng et al., 2018). Atmospheric background mixing ratios thus reflect regional atmospheric conditions and are closely related with regional emissions (Cheng et al., 2017; 2018).

In contrast to studies in urban areas, studies on greenhouse gases at background stations provide relevant information on the influence of anthropogenic emissions, which are limited in this type of station, but which are also helpful for addressing the potential influence of long-range transport of air masses from other areas and which can lead to important variations in background mixing ratios in rural areas (Calvo et al., 2012; Cheng et al., 2019; Di Gilio et al., 2015). Atmospheric background mixing ratio levels can therefore play a significant role in understanding regional source–sink patterns (Cheng et al., 2018).

Given their critical importance, a number of studies on CO_2 and CH_4 have been carried out at several background sites worldwide (e.g. Curcoll et al., 2019; Feng et al., 2019; Guha et al., 2015; Pu et al., 2014; Wang et al., 2016; Yang et al., 2019) in order to provide useful information to study their temporal patterns at background levels (Bamberger et al., 2017; Schibig et al., 2015; Schmidt, 2003). However, more observational studies at such background sites are still required in order to increase current knowledge concerning the temporal evolution of CO_2 and CH_4 worldwide (Cheng et al., 2019; Curcoll et al., 2019) so as to establish appropriate thresholds for policy decisions. The CIBA station is, to the best of our knowledge, the background station in Castilla y León with the longest time series record of CO_2 and CH_4 mixing ratios and the only one in the Iberian Peninsula included in the international Carbon Cycle Surface Flasks network, led by the National Oceanic & Atmospheric Administration (NOAA), from May 2009 (labelled as CIB station). Thus, maintenance of the station and the characterization of CO_2 and CH_4 temporal patterns is crucial due to its regional representativeness in terms of atmospheric conditions and regional emissions.

2.5. CIBA station characteristics

Briefly, the main characteristics that make the CIBA station an ideal place to monitor CO_2 and CH_4 evolution are the following:

1. Castilla y León, the region where the station is located, is considered one of the cleanest atmospheric areas in south-western Europe, according to Burgos (2016b).
2. The station is labelled as a regional background station and, therefore, observations from the CIBA station could be considered as representative of the whole region.
3. The station is located in a remote semi-arid area mostly surrounded by croplands, which is the main vegetation in the region of Castilla y León (Paredes, 2013) and, therefore, representative of regional vegetation composition.
4. The sampling site is located in a flat area; hence, it is easy to access and to maintain the equipment.
5. The regular topographical characteristics of the area also make atmospheric circulation consistent.

The CIBA station has proven to be an ideal emplacement node in the region for a wide number of scientific atmospheric studies, the most relevant of which are listed in Section 5.1.

2.5.1. Previous studies at the CIBA

First, one of the most prominent studies was conducted by San José et al. (1985) in which the mathematical limits of Businger's functions, which are designed to calculate two important turbulent parameters - friction velocity and the Monin-Obukhov length - were analysed.

Second, the studies conducted by Cuxart et al. (2000) merit particular attention. Cuxart et al. (2000) studied the properties of the Stable Atmospheric Boundary Layer at the CIBA station during September 1998 under the "SABLES98" project. The goal of the project was to study the stable boundary layer in flat conditions and to look for the presence of low-level jets. As a continuation of the "SABLES98" project, Terradellas et al. (2001) introduced wavelet methods to study the atmospheric boundary layer under stable conditions. Furthermore, Conangla and Cuxart (2006) continued with the characterization of low-level jets by employing captive balloon soundings as well as turbulence measurements performed with high-frequency data. Finally, Cuxart et al. (2008) studied low-level jets, combining observational data at the CIBA station and modelling experiments.

Third, Yagüe et al. (2007) showed preliminary results concerning the characterization of wave events at the CIBA station in the context of the Stable Atmospheric Boundary Layer Experiment in Spain 2006, the so-called "SABLES2006" project. As a continuation of the "SABLES2006" project, Viana et al. (2009) described the generation and propagation of a gravity-wave episode through tower, RASS-SODAR, microbarometric, satellite imagery and automatic station data. In the same line, Viana et al. (2010) illustrated drainage or katabatic flows as a common source of internal gravity waves. Furthermore, wavelet techniques were applied to sonic anemometer records to study the interaction between turbulence and larger-scale motions. Finally, Udina et al. (2013) reproduced the internal gravity waves generated during the "SABLES2006" project and their origin through mesoscale meteorological modelling.

Fourth, Soler et al. (2014) analysed eight atmospheric density current fronts at the CIBA station within the framework of the "INTERCLE" project, designed to study and parameterise heat, humidity and momentum exchanges in the stable boundary layer. The study was conducted from September 2002 to November 2003, using observational data and numerical simulations through the Weather Research and Forecast (WRF) Model. The equipment used was located on the 100-m high tower equipped with fast-response sonic anemometers and conventional sensors which measure wind speed and direction, air temperature and relative humidity at different heights, as well as soil temperature and atmospheric pressure at the surface.

Fifth, other important analyses conducted outside the framework of major projects at the station include those carried out by Bravo et al. (2008) who analysed the performance of two different mesoscale models during two nights at the CIBA station. In addition, Román-Cascón et al. (2012; 2016a; b; 2019) performed climatology studies of radiation fog events through robust statistical analysis in order to evaluate the robustness of different methodologies designed to forecast radiation fog events.

Finally, the University of Valladolid Atmospheric Pollution Group, within which the current thesis has been carried out, has been involved since the CIBA's creation in many scientific topics. To mention but a few, these include the description of daily wind speed evolution at the station through measurements using sodar equipment (Pérez et al., 2004a) or the identification of cyclical processes in wind speed and temperature data using autocorrelation analysis (Pérez et al., 2004b). In addition, Sánchez et al. (2008) analysed the daily and seasonal variation of surface ozone mixing ratio data at the station from February 2000 to December 2005. Other important studies are those involving a daily, seasonal and inter-annual variability description of atmospheric CO_2 mixing ratio data for an eight-year period using a MIR 9000

continuous infrared analyser (Sánchez et al., 2010). Sánchez et al. (2014) also studied diurnal and seasonal CH_4 mixing ratio patterns from June 2010 to May 2012 using a high precision cavity ringdown spectroscopy technique. An interesting comparison between CO_2 concentrations at a suburban site in the city of Valladolid and the rural site of the CIBA station was also conducted by García et al. (2012). Some of the most recent studies of the group involve those concerning the analysis of the role played by meteorological variables in CO_2 and CH_4 trend and seasonal evolution (Pérez et al., 2017; 2018b; 2019). To conclude, several backward analyses have been conducted in order to link their characteristics to the final CO_2 and CH_4 mixing ratio measured at the CIBA station (García et al., 2016; Pérez et al., 2017; 2018a; 2019). The current thesis aims to study CO_2 and CH_4 temporal patterns by employing different statistical techniques whilst at the time exploring the possible influence of the city of Valladolid on final CO_2 and CH_4 mixing ratio values collected at the CIBA station. For that reason, the following section (2.6) is devoted to analysing what a time series is as well as the most common methods used to study it.

2.6. Time series

A time series is a set of recorded values of a specific variable collected at regular time intervals in chronological order over a long period of time (Chatfield, 1995; Everitt et al., 2010). A time series is basically made up of three different components; namely the trend, the seasonal component, and the random error. Generally, a time series (Y_t) is expressed as follows (Bianchi et al., 2019; Chham et al., 2019; Fan et al., 2003):

$$\mathrm{Y_t} = \mathrm{T_t} + \mathrm{P_t} + \mathrm{R_t} \qquad [1]$$

where t is the time and Y_t are the observations. The two first components of equation 1 are commonly referred to in the ample literature as temporal pattern indicators (Cui et al., 2011; Fang et al., 2020; Fernandez-Cortes et al., 2006; Li et al., 2020). On the one hand, T_t represents the trend component which stands for the long-term variations that provide information concerning changes in annual evolution by simply ignoring the seasonal cycle of the time series. It should be mentioned that the trend is frequently discussed through the growth rate indicator which reflects the mixing ratio evolution over time. The current thesis also employs the growth rate indicator to analyse mixing ratio evolution over time. P_t is the short-term referred to as the seasonal component which expresses the cycles (i.e. regular fluctuations) occurring within the time series, and providing information about changes in the intra-annual evolution. As the presence of trends in a time series hinders the identification of periodicities, they should be removed in order to identify periodicities within a dataset. Finally, R_t is a stochastic component reflecting the mean of the residuals. In this case, and following

other authors such as Fan et al. (2003) or Fernandez-Cortes et al. (2006), the mean of the residuals is assumed to be constant and equal to zero.

The main goals of a time series analysis are [1] to describe and analyse its evolution over time, [2] to forecast future events, and [3] to control future events through intervention (Fan et al., 2003). The current thesis is focused on the first objective.

The first step when analysing a time series is to plot the data in order to visually analyse the data pattern. If a trend or seasonal pattern is observed, it is crucial to analyse both components of the time series separately (Fan et al., 2003) in a detrending or deseasonalised process. The detrending (deseasonalised) process involves subtracting the trend (seasonal) component of the time series from the original values of the series; hence, the seasonal (trend) component can be analysed separately (Everitt et al., 2010).

To display data graphically in a simple way, data should be smoothed so as to remove, by averaging, the extreme values of the time series, identifying peaks and troughs as well as data symmetry (Fan et al., 2003; Gramacki, 2018; Wand et al., 1995; Wasserman, 2006). Smoothing techniques involve fitting a mathematical equation to a set of observations to highlight any unusual structure, which allows conclusions to be drawn from well-designed graphics (Everitt et al., 2010). Temporal series usually require special methods for their analysis due to the presence of serial correlation between the individual observations. Since reducing emissions is one of the major concerns of energy and environmental protection policies worldwide, robust estimations are crucial when assessing CO_2 and CH_4 temporal evolution. There are many different approaches for smoothing time series data (Cheng et al., 2018; Fang et al., 2015) although most are based on moving averages values. Despite the great use of autoregressive moving average models for analysing time series, there are many phenomena that cannot be adequately described by this method (Everitt et al., 2010). In this sense, Everitt et al. (2010) consider harmonic regression functions as an alternative for analysing time series. However, harmonic functions, as with all parametric functions (i.e. the form of the probability laws is specified) might occasionally prove to be too rigid due to their restriction of a function belonging to a parametric family, which could lead to inappropriate conclusions (Fan et al., 2003). However, the rigidity of parametric regressions can be overcome by removing the restriction that a function should belong to a parametric family. This approach leads to what is commonly referred to as non-parametric regression techniques (i.e. the form of the probability laws is not completely specified). Indeed, there is a long tradition in applying non-parametric methods in time series analysis to decompose them (Fan et al., 2003;

Krisp et al., 2009; Peña et al., 2001; Wasserman, 2006). The main motivation for a non-parametric approach regression is to let the data decide which function fits them best without the restrictions imposed by a parametric function. However, the gain in flexibility comes at the price of finding the optimal (given certain criteria) bandwidth (Gramacki, 2018; Müller, 1988; Peña et al., 2001).

Nevertheless, parametric and non-parametric regressions should not be seen as competitors, since in many cases a non-parametric regression estimate will suggest a simple parametric function, while in other cases it will be clear that the underlying regression function is so complicated that no reasonable parametric function would be adequate (Wand et al., 1995). For these reasons, the current thesis employed both parametric and non-parametric functions, as shown in Figure 10.

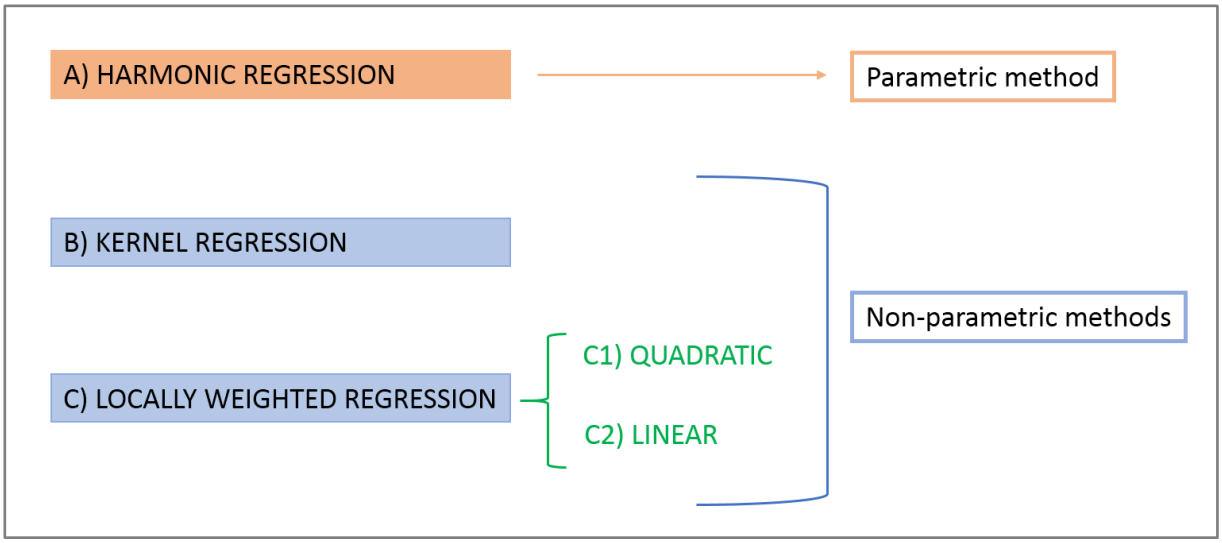

Figure 10. Schematic representation of the smoothing mathematical methods used in the current thesis.

2.6.1. Parametric equations

2.6.1.1. Harmonic regression equations

Harmonic functions employ a k-degree polynomial function in order to obtain the trend component of a time series (Fernandez-Cortes et al., 2006; Peña et al., 2001). As regards the seasonal component, harmonic functions employ a sum of sine and cosine terms to the time series (Everitt et al., 2010; Peña et al., 2001).

In parametric polynomial regression the degree of the polynomial is the smoothing parameter (Wand et al., 1995) for determining the trend. Thus, a decision involving the degree of the

polynomial trend and the trigonometric polynomial should first be taken. Fitting a higher-order polynomial will possibly reduce bias although, on the other hand, variance will increase since more parameters must be locally estimated.

2.6.2. Non-parametric equations

The practical implementation of the kernel density estimator and the local weighted method first require optimal determination of the bandwidth value (Wand et al., 1995). The bandwidth (h) is a smoothing parameter that controls the amount of smoothing applied to the data and the size of the local neighbourhood data points considered in the estimation (de Haan 1999; Gramacki, 2018; Hernández-Ceballos et al., 2019; Wand et al., 1995; Wasserman, 2006). It is important to bear in mind that high h values lead to an estimator with major bias but small variance, resulting in smoother shapes (i.e. over-smoothing), thereby suppressing some details of the time series (Wasserman, 2006). On the other hand, low h values lead to an estimator with small bias but large variance, resulting in a more irregular shape (i.e. under-smoothing) dominated by noise or large peaks, making it difficult to locate true peaks (Wasserman, 2006). An optimal bandwidth will thus be achieved when changes in bias and variance balance out (Peña et al., 2001). Figure 11 shows the effect of different bandwidth values on kernel density estimations.

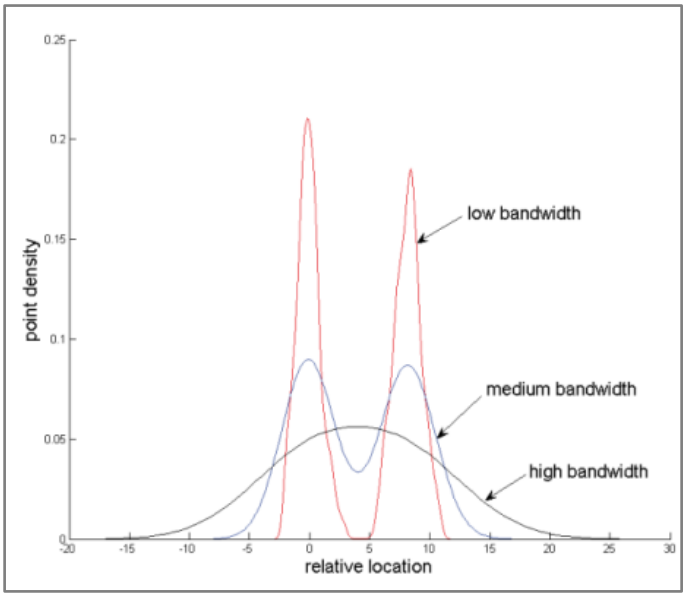

Figure 11. Kernel Density estimation employing different bandwidth values (Krisp et al., 2009).

The field of bandwidth selection remains unresolved, although there is a considerable amount of ground-breaking research into the problem. Bandwidth selection aims to find a simple method to make automatic bandwidth selection, which would prove to be extremely useful

when kernel estimators are used as components of larger statistical procedures (Wand et al., 1995). Briefly, it is possible to point to two different approaches to select optimal bandwidth. The first consists of applying mathematical equations which aim to find a reasonable bandwidth for a wide range of situations, but without any guarantee of being close to the optimal bandwidth for the specific dataset. These are motivated by the need to have fast automatically generated kernel estimates and to provide a reasonable starting point for choosing the smoothing parameter (Wand et al., 1995). However, they require substantial computational resources. On the other hand, a trial and error approach, which is highly recommended for exploratory analysis, is one possible solution for easy bandwidth determination (Wilks, 2019).

2.6.2.1. Kernel regression equations

Kernel regression smoothing is a distribution method for smoothing data by using kernel density estimators (Everitt et al., 2010; Wasserman, 2006). The accuracy of the kernel estimators strongly depends on the bandwidth value (Gramacki, 2018). Kernel regressions offer a large family of curves to choose from for increasing data flexibility (Wand et al., 1995). Figure 12 (next page) shows the different kernel functions analysed in the current thesis. More details concerning kernel density estimation can be found in Devroye and Györfi (1985), Scott (1992) and Silverman (1986) (Fan et al., 2003).

2.6.2.2. Local regression equations

The decomposition of a time series into trend and seasonal components by locally weighted scatterplot smoothing (lowess) was introduced into the statistical literature by Cleveland (1979) and Stone (1977) (Peña et al., 2001). Locally weighted regression, usually known as lowess, is a robust method of regression analysis in which polynomials of degree one (linear) or two (quadratic) are used to approximate the regression function in particular “neighbourhoods” of the space of the exploratory variables. This mathematical procedure is used to guard against deviant points distorting the smoothed points. Essentially, the process involves an adaptation of iteratively reweighted least squares (Everitt et al., 2010).

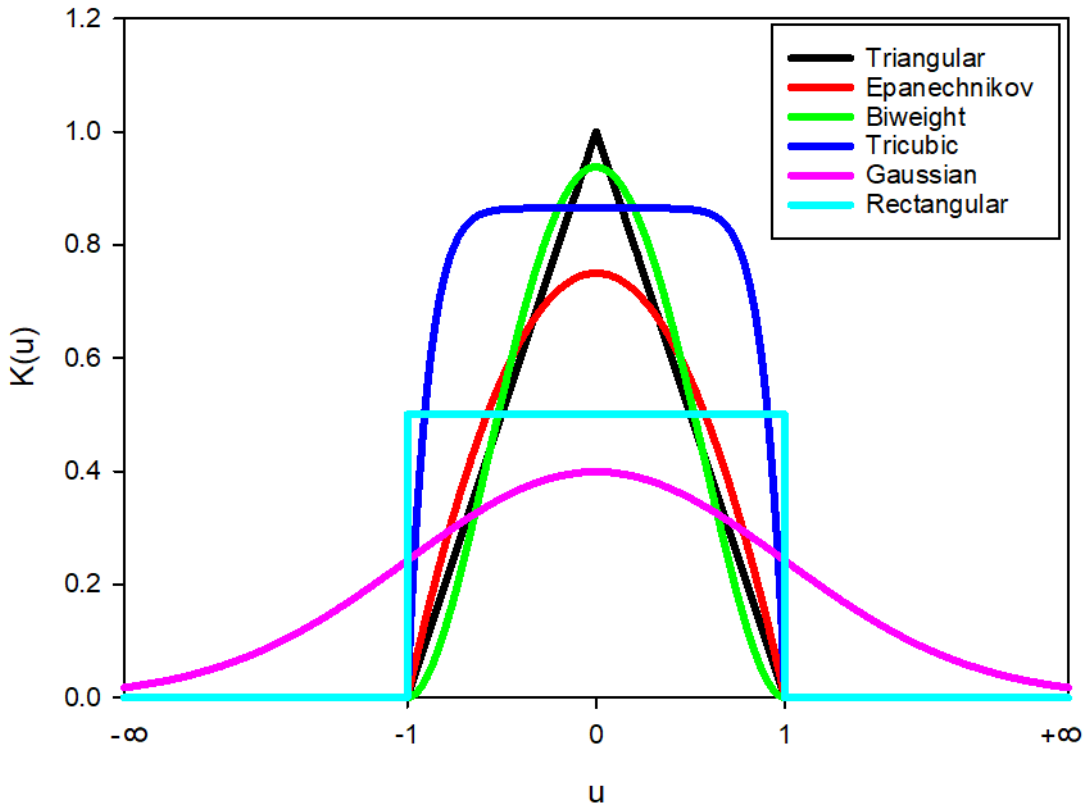

Figure 12. Smoothing kernels employed in contribution **II**. It should be noted that u= [(t-ti)/h], where t is the time expressed in days and h is the bandwidth, which is also expressed in days. Kernel functions are mathematically described in section 4.6.2.1.

2.7. Valladolid urban plume analysis

Once in the atmosphere, the primary process favouring the transport and dispersion of substances is wind regimes (Hernández-Ceballos et al., 2019). As stated by Liu et al. (2000), wind direction determines the travel direction of an air species and the receptor which is affected at a given time. After emission, pollutants can be quickly dispersed and diluted, resulting in low concentrations levels, or they can be concentrated in a relatively small volume, which leads to episodes of high mixing ratio values (Brancher et al., 2017). As Brancher et al. (2017) stated, one of the main purposes of studying atmospheric behaviour is to mathematically describe the spatiotemporal distribution of substances emitted into the atmosphere.

2.7.1. Transport of air masses

Ninety percent of the atmosphere's mass lies within just 15 km of the surface (Liu et al., 2000), in the lower atmosphere. The lower atmosphere comprises the troposphere, which is governed by turbulent mixing of air and where weather and air pollution problems occur (Liu et al., 2000;

Visconti, 2016). The troposphere is divided into the planetary boundary layer (PBL), which extends from the Earth's surface to about 3,000 m a.g.l. (Hernández-Ceballos et al., 2013), and the free troposphere, extending from about 3,000 m a.g.l. to the tropopause (Brancher et al., 2017). This thesis focuses on analysing the temporal patterns of CO_2 and CH_4 within the lower troposphere, and more specifically within the planetary boundary layer since this is the region which contains most emission sources of air pollutants (Turner, 1994). Indeed, most gases from anthropogenic activities or natural processes enter the atmosphere through the PBL (Brancher et al., 2017). The transport of a pollutant emitted into the PBL suffers the action of mechanical turbulence (wind speed and topography) and thermal turbulence (heating and cooling of the Earth's surface) (Di Gilio et al., 2015). The mathematical equations governing air mass movements might be extremely complex since they involve the three classical conservation equations: mass, momentum, and energy (Fraile et al., 2006). Air transport methods make use of the meteorological models available to explain the transport of air mass parcels (Fraile et al., 2006). The main differences between the meteorological model available concern the approach used when applying the equations and the temporal and spatial scales employed (Brancher et al., 2017; Fraile et al., 2006).

Air trajectory analysis is a scientific tool that is mainly used to characterize wind flow patterns (e.g. Calvo et al., 2012), to identify the source regions of atmospheric pollutants (e.g. Dimitriou et al., 2017a) or to analyse the relation between air mass properties and final mixing ratio of different air species (e.g. Burgos et al., 2016a; Dimitriou et al., 2017b; Hernández-Ceballos et al., 2013; Lozano et al., 2012; Sorribas et al., 2015; 2019; Toledano et al., 2007; Velasco-Merino et al., 2018) due to the role that meteorology plays in the formation, dispersion, transport and dilution processes of air species.

In meteorological studies, trajectory is defined as the pathway of an infinitesimal air parcel through a centreline of an advected air mass with time (Hernández-Ceballos et al., 2019). The back-trajectory is then the pathway previously travelled by the air mass before arriving at a certain point (Hernández-Ceballos et al., 2013). This is useful because it provides information about whether the air has previously been in touch with a source of pollution, thereby supporting data interpretation (Megido et al., 2017). The outputs of the model are the geographic coordinates of the air mass position, at hourly intervals, from the moment chosen until the arrival time, and which can be plotted on a map so as to better visualize the air paths followed (Fraile et al., 2006).

The current thesis used a flexible tool for air trajectory calculation called the METEX model, which consists of a Lagrangian and a Eulerian approach. As stated by Brancher et al. (2017),

Lagrangian models describe variations in concentration in relation to the moving fluid when air plumes divide into simpler elements (Zannetti, 1993). Eulerian models, which are a common way of describing heat and mass transfer phenomena, describe the behaviour of air species in relation to a fixed coordinate system (Brancher et al., 2017). Moreover, the METEX model is also a receptor model since it is designed to search for possible sources that could contribute to the mixing ratio recorded at the receptor point (Fraile et al., 2006), established in the current thesis as the CIBA station.

2.7.2. CO_2 and CH_4 episode determination

In order to identify the CO_2 and CH_4 mixing ratio episodes that occurred during the study period, a mixed methodology based on statistical and air trajectory analysis was employed. Calculation of the statistical 90^{th} percentile value for the mixing ratio data as a threshold enabled rapid identification of the highest values over the time series (Hernández-Ceballos et al., 2015a; Lozano et al., 2012; San Miguel et al., 2019), which were considered episodes. Only episodes were considered for analysing the possible influence of the Valladolid urban plume on the final CO_2 and CH_4 mixing ratio data measured at the CIBA station. Once the episodes were determined, they were first linked to their incoming wind surface direction. Second, back-trajectories were computed at the CIBA station, linking the final CO_2 and CH_4 mixing ratio collected at the station with the back-trajectory paths so as to confirm the possible influence of the urban plume of the nearby city of Valladolid at 500 m height a.g.l.

Computing back-trajectories together with surface wind observations sought to combine regional and local approaches for analysing the possible influence of the Valladolid urban plume on the final CO_2 and CH_4 mixing ratio measured at the CIBA station. As stated by García-Mozo et al. (2017), differences between mixing ratio values allows for a distinction to be drawn between local and external contributions, thus giving a clearer idea of the origin of the mixing ratio measured at the station. However, as pointed out by Hernández-Ceballos et al. (2014b), attempts at quantitative analysis using backward trajectory models are scarce. Thus, the current thesis aims to highlight the usefulness of these methods for identifying the possible origin of pollution sources.

2.8. Motivation of the study

In the absence of rapid emission reductions, an escalation in the climate change process is expected (IPCC, 2019), partially due to the influence of human activities on the environment (Megido et al., 2017), such as the increased burning of fossil fuel, which is exacerbating the

greenhouse effect because of a rise in the GHG mixing ratio in the atmosphere (Anderson et al., 2016). In order to reach the main goal of the Paris Agreement, emissions of greenhouse gases must be drastically reduced. As many authors have stated, the ongoing climate crisis demands the quantification of greenhouse emissions as a first step towards obtaining data for important assessment reports (e.g. IPCC) which serve as a guideline for implementing an effective climate policy (Arioli et al., 2020). By the same token, long-term studies of the evolution of GHG in the atmosphere are essential vis-à-vis evaluating the effectiveness of the environmental policies implemented.

As already described, CO_2 and CH_4 are the two most important greenhouse gases involved in climate change. As a result, identifying and understanding their temporal patterns is crucial for predicting different climate change scenarios using various Earth system models (Friedrich et al., 2020; Wang et al., 2020). An understanding of CO_2 and CH_4 temporal patterns could suggest specific methods, thereby making model selection more efficient by adding or removing the trend or the seasonal component and thus enabling a more precise modelling result. Moreover, CO_2 and CH_4 temporal patterns may be useful to modellers as input data in order to compare modelled values with reliable observations from a representative background station (Arioli et al., 2020; Wang et al., 2020). Finally, this information is valuable for society as a whole, which is now greatly concerned about climate change and its possible consequences.

Despite the importance of analysing CO_2 and CH_4 temporal patterns, important gaps in our knowledge persist in this field, mainly due to; [1] lack of data, which can become a serious challenge for climate solutions, [2] the choice of adequate calculation methods for determining temporal patterns. The main motivation of the present thesis is therefore to overcome both of these gaps in our knowledge.

First, in order to overcome the lack of data, it should not be forgotten that data collection needs to be improved in terms of availability, coverage, resolution, quality, and reliability (Arioli et al., 2020). To overcome the challenge of data availability and coverage, the number of stations needs to be increased, since the number of measurements and their spatial coverage are still insufficient in certain European regions (Marquis and Tans, 2008), especially in the north-western part of the Mediterranean area (Curcoll et al., 2019). As regards data resolution, Curcoll et al. (2019) pointed out the importance of regional or local studies to assess the extent to which ecosystems influence climate change. In this way, it is important to note that rural background stations are ideal emplacements for determining GHG temporal patterns, since air species footprints are more distinguishable due to the reduced local emission sources in the surrounding areas (Arioli et al., 2020). Finally, in order to meet the need for high quality and

reliable time series it is crucial to use high precision technology to measure air species mixing ratios. Studies at the CIBA station are particularly important due to the crucial role that the station plays since it is a background station and is therefore representative of the region of study. Furthermore, the station is equipped with high precision technology to measure CO_2 and CH_4 mixing ratios in real time.

Second, in order to overcome the problem of the calculation method chosen to examine the temporal series (i.e. trend, growth rate, and seasonal analysis) of the CO_2 and CH_4 mixing ratio, the current thesis proposed the analysis of different statistical techniques. As stated by Nakazawa et al. (1997), it is important to study the same database applying different statistical methods in order to determine which of them is best able to capture the salient features of the time series. At the same time, an evaluation of database consistency can be assessed by comparing the results obtained from the different methods employed. In addition, use of the methods employed here at other background stations is another of the main motivations of the current thesis. Hence, all the methods used pursue simple implementation (i.e. easy to use, quick and with low computational requirements) which encourage their use, thus achieving greater coverage of the worldwide evolution of CO_2 and CH_4, and improving our understanding of how these two important greenhouse gases develop in the lower atmosphere.

The current thesis therefore aims to describe, analyse and quantify CO_2 and CH_4 temporal patterns (i.e. annual and intra-annual changes) over the upper Spanish plateau for five and a half years at a background regional station where few studies on this topic have been conducted to date. The current thesis constitutes an extension of previous studies in the sampling area carried out by the research group (e.g. Pérez et al., 2016; 2017; 2018b), although they used a smaller database (e.g. Sánchez et al., 2014), collected data using less precise measuring equipment (e.g. Sánchez et al., 2010) or did not distinguish between diurnal and nocturnal data (e.g. Pérez et al., 2016; 2017; 2018b), which the current thesis does do.

More specifically, the motivation of the contributions that make up the current thesis are as follows:

- ✓ As regards harmonic analysis (contribution **I**), the main motivation was based on the need to use a harmonic equation to analyse temporal patterns whilst at the same time capturing the salient features of the time series.

- ✓ As regards the kernel smoothing analysis (contribution **II**), since the most crucial task in the kernel smoothing regression involves determining an optimal bandwidth (de

Haan, 1999), contribution **II** aimed to establish a simple and fast method for determining this whilst at the same time demanding low computational resources. Moreover, analysing the influence of different kernel functions when determining temporal patterns was another important motivation, since some authors do not consider the chosen kernel function to be a key point (e.g. de Haan, 1999; García-Portugués et al., 2014) whereas others do (e.g. Nakazawa et al., 1997; Rodríguez-Cortés et al., 2015). Moreover, since most of the papers in the literature have applied either the Epanechnikov or Gaussian kernel, few scientific papers compare the efficiency of different kernels on a dataset (Gramacki, 2018), such that we consider it interesting to address this issue in the present study. Finally, since the Gaussian kernel involves a higher computational cost due to all of the observations being considered (Wilks, 2019), we considered it interesting to cut the interval calculation to (-3, 3) and also to (-1,1) so as to assess whether a decrease in computational time may be observed without any loss of data accuracy.

- ✓ As regards the local smoothing regression technique (contribution **III**), an analysis concerning the differences between the local linear and local quadratic approach was conducted in order to determine the possible superiority of either approach in determining the salient features of the temporal series.

- ✓ Finally, a backward trajectory analysis (contribution **IV**) was conducted in order to analyse the possible influence of the Valladolid urban plume as well as its urban emissions on the final CO_2 and CH_4 measurements collected at the CIBA station.

A concept map of the thesis including all of the original contributions is shown in Figure 13 (next page).

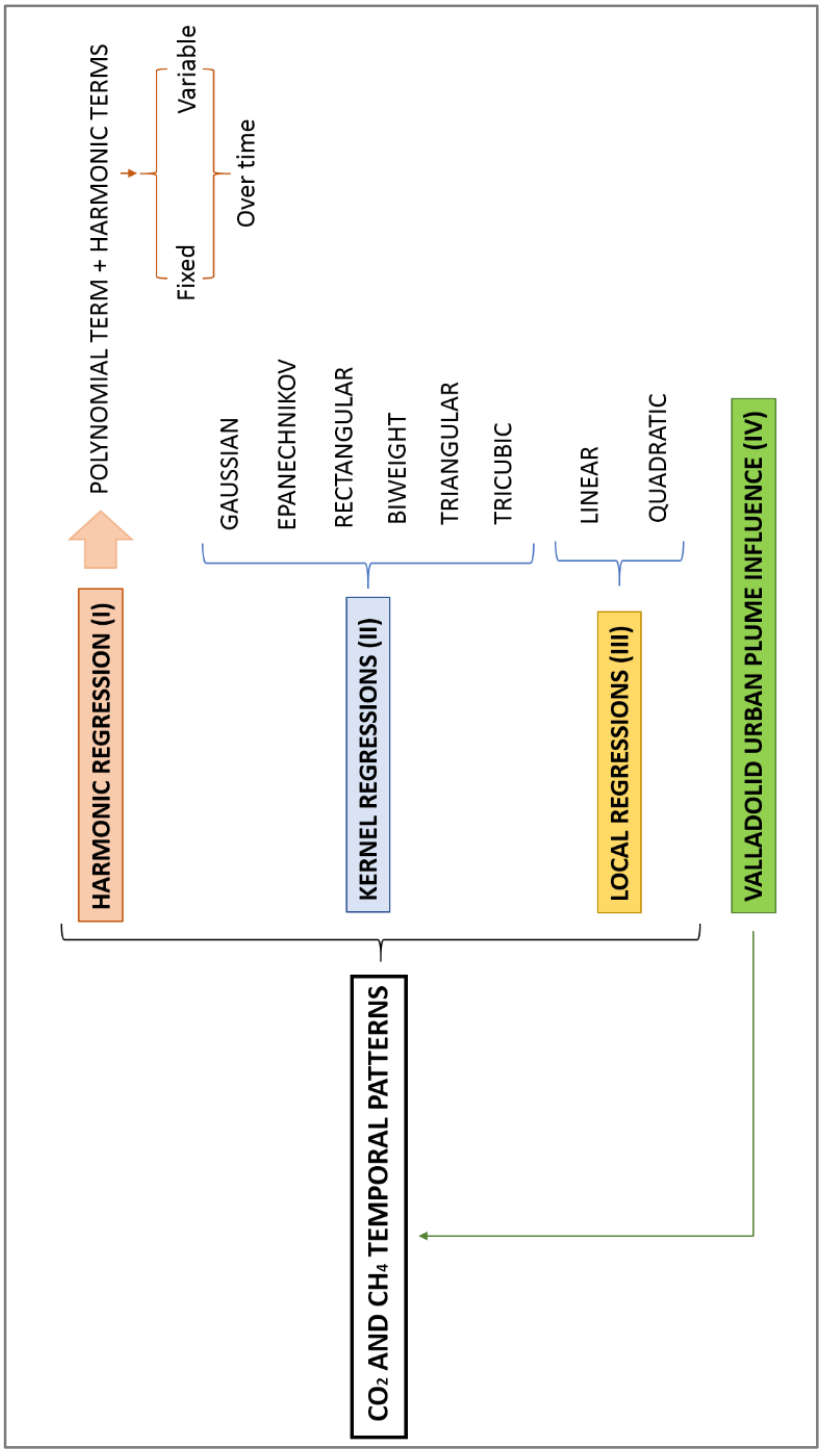

Figure 13. Concept map of the thesis including all of the original contributions in Roman numerals.

3. Objectives

3.1. General objective

The main goal of the current thesis is to characterize the temporal patterns (i.e. annual trends, growth rate and seasonal cycles) of a five and a half year long CO_2 and CH_4 mixing ratio time series over the upper Spanish plateau using different mathematical functions. In addition, differentiation between diurnal and nocturnal data was carried out in order to obtain a better knowledge of both scenarios. This is the first CO_2 and CH_4 temporal analysis at the sampling site based on such a long-term dataset with emphasis on the differentiation between diurnal and nocturnal data. Finally, determining the influence of the Valladolid urban plume effect on the final CO_2 and CH_4 measurements collected at the monitoring station also formed part of the general objective.

3.2. Specific objectives

I	To apply a harmonic equation considering a third-degree polynomial plus four harmonics considering the amplitude variable over time in order to better analyse the temporal patterns of the dataset (original contribution **I**).
II	To provide an easy, quick and reproducible method to determine the optimal bandwidth for a kernel function (original contribution **II**).
III	To analyse the ability of six kernel functions to capture the salient features of the time series (original contribution **II**).
IV	To study the ability of local linear and quadratic regressions to describe CO_2 and CH_4 temporal patterns (original contribution **III**).
V	To compare the efficiency of different mathematical functions for describing the CO_2 and CH_4 temporal patterns of the time series (not considered in the articles).
VI	To determine the influence of the Valladolid urban plume on the final CO_2 and CH_4 mixing ratio dataset (original contribution **IV**).

4. Material and methods

4.1. Site description

The area of study corresponds to a semi-arid Mediterranean rural area located in the large region of Castilla y León. This area is referred to as the Upper Spanish plateau. Castilla y León, located in the North-West of Spain (Figure 14), is one of the Spanish regions with the lowest population density. It covers an area of 94,222 km^2, which is about one fifth of the whole country (del Río et al., 2007). It is the largest region in Spain and the third largest in Europe, and has a population of around 2.5 million people (European Commission, 2020). Castilla y León is characterized by prevalent clean atmospheric conditions with the occurrence of long-range transport pollutants of anthropogenic origin. Thus, the area of study is adequate for this kind of study (Bennouna et al., 2016). Except to the west, the region is surrounded by large mountain systems which are around 2,000-2,500 m height.

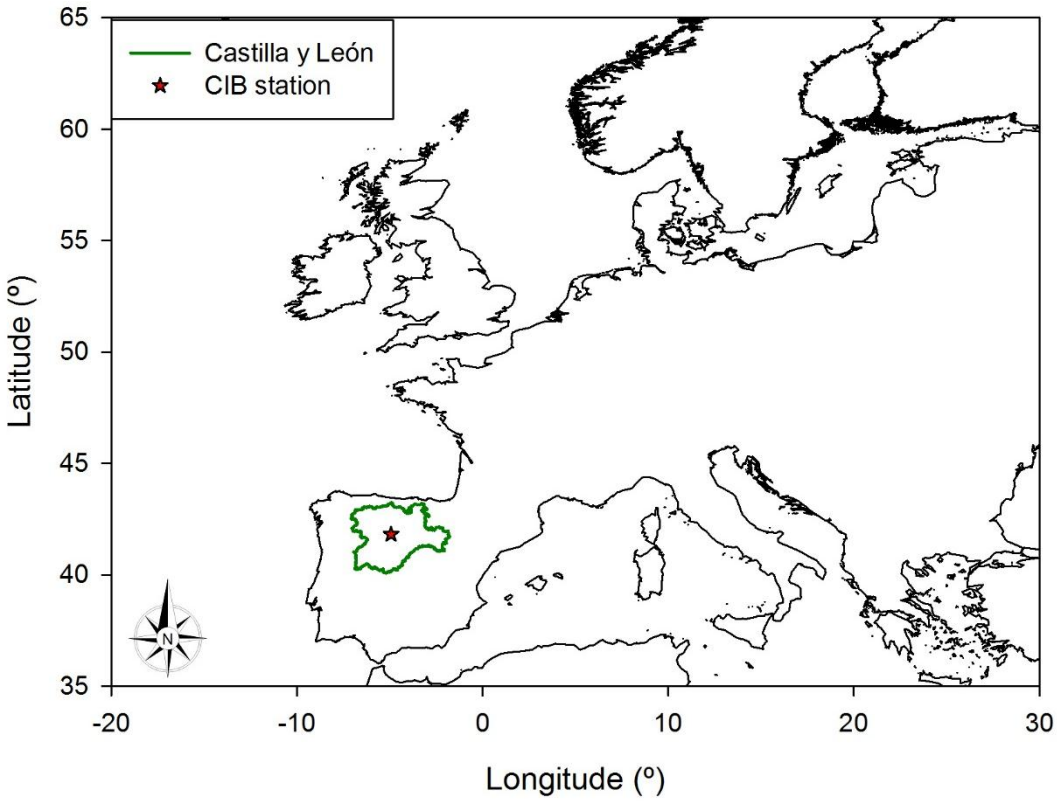

Figure 14. Location of the region and the monitoring station of the study.

As shown in Figure 15, Castilla y León is surrounded to the north by the Cantabrian mountain range, to the east by the Iberian System, to the south by the Central System and to the north-west by the Galician Massif (Pérez et al., 2018c). Internal waves associated with a katabatic

flow from the Guadarrama mountain range 100 km southeast of the CIBA station are also noticeable in the area (Cuxart et al., 2000). The Duero River flows along the south-eastern part of the region towards its western part, extending across Portugal to the Atlantic Ocean. The monitoring station is located on a smaller plateau within the Upper Spanish plateau, known as Montes Torozos, which is an almost flat area of 800 km^2 (Conangla and Cuxart, 2006; Román-Cascón et al., 2012; Soler et al., 2014).

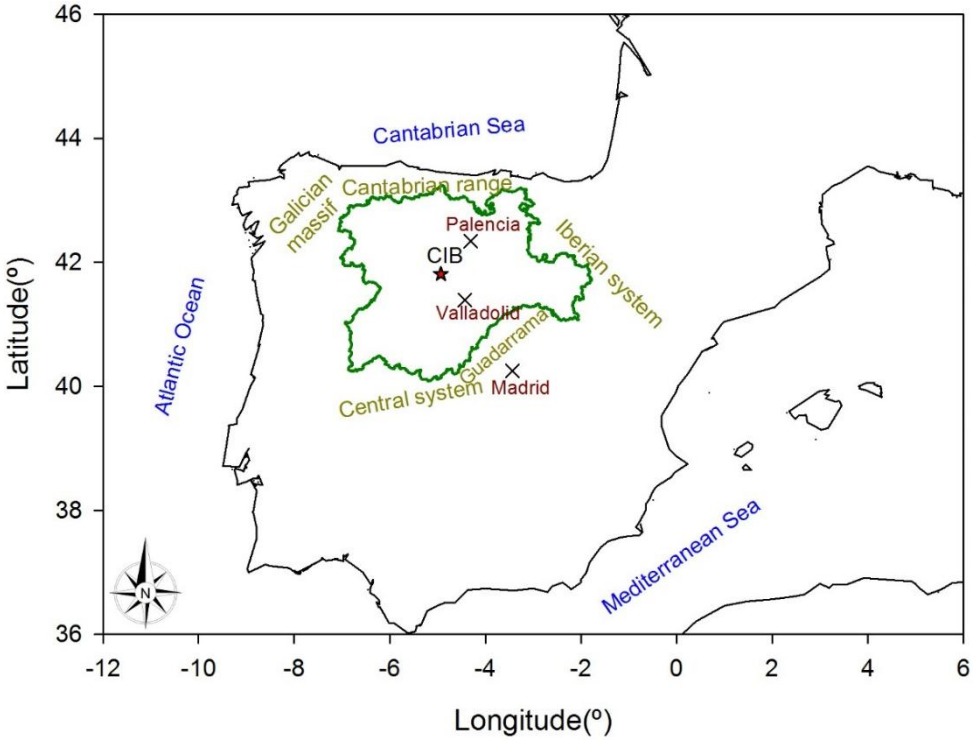

Figure 15. Characterization of the monitoring station in terms of main water bodies, mountain ranges and nearest populated cities.

The plateau rises some 50 m above an extensive region of homogeneous flat terrain (Cuxart et al., 2000). The change in height across the plateau is only around 5 m from northwest to southeast and around 30 m along 50 km from the northeast to the southwest, with a negative slope in the southwest direction (Cuxart et al., 2000). The two major cities near the CIBA station are Valladolid (304,000 inhabitants), which is 24 km to the southeast, and Palencia (80,000 inhabitants), which is 40 km to the northeast. Climatologically speaking, a Mediterranean continental climate characterizes the area. Indeed, the area of study is labelled as a warm summer Mediterranean climate (Csb) following the Köppen–Geiger climate classification (Kottek et al., 2006; Román-Cascón et al., 2016a). This climate consists of maximum temperatures in the hot summer and minimum temperatures in the long cold winter, and there are frequent hard frosts. In terms of rain, the area is characterized by wet springs and autumns stemming from cold and warm fronts arriving from the Atlantic with westerly winds, and dry

summers punctuated only by rains in the form of sudden storms and showers caused by convection (Fernández-Raga et al., 2010; García et al., 2012; Román Cascón et al., 2016a; Sánchez et al., 2003; 2014). Finally, it should be pointed out that agricultural crops, grass, scattered coniferous stands and Mediterranean shrubs make up the surrounding vegetation.

4.2. Monitoring station

The temporal CO_2 and CH_4 time series on which the current thesis is based was obtained from the Low Atmosphere Research Centre (CIBA station) and covers a five and a half year period (October 2010-February 2016). The CIBA station (lat: 41º 48´ 49´´N; long: 4º 55´59´´W, alt: 845 m a.s.l.) was founded in 1978 by the University of Valladolid and current Spanish Meteorological Agency (AEMET) (Cuxart et al., 2000). The station is currently managed by the Department of Applied Physics of the Faculty of Sciences at the University of Valladolid (Spain). The monitoring station has formed part of the Carbon Cycle Surface Flasks Network, managed by the Global Monitoring Division (GMD) of the National Oceanic & Atmospheric Administration (NOAA) since May 2009. The GMD network certifies the quality of the data used in the current thesis. This cooperative air sampling network began in 1967 at Niwot Ridge (Colorado). Currently, the network is a global project comprising 229 stations in 50 different countries, although in Spain there are only two stations which take surface flask measurements: the Izaña Observatory in the Canary Islands and the CIBA station in the Upper Spanish plateau. The gas species under consideration at the CIBA station for the flask campaign are: CO_2, CH_4, CO, H_2, N_2O, SF_6 and the isotopes $\delta^{13}C_{CO2}$ and $\delta^{18}O_{CO2}$.

4.3. Instrumentation

A Cavity Ring-Down Spectroscopy (CRDS) analyser (G1301, Picarro Inc., USA) installed at the CIBA station was the equipment used to obtain CO_2 and CH_4 mixing ratios. The analyser is based on optical absorption spectroscopy of the sample gases to determine the mixing ratio (Tang et al., 2015). The analyser presents quick response, high linearity and precision (± 0.02 ppm for CO_2 and ± 1 ppb for CH_4) and requires minimal calibration. Furthermore, the equipment requires no consumables and no sample preparation or drying. Figure 16 shows an aerial view of the CIBA station and its instrumentation.

The Picarro analyser comprises two different parts, as shown in Figure 17:

A. The Power Vacuum Unit (PVU) contains a computer and a diaphragm pump to draw the sample gas through the instrument. In this component, AC power is converted to DC power.

B. The Data Acquisition System (DAS) contains the spectrometer and the sample chamber. From this part of the equipment the spectroscopic information is sent to the computer. This part converts spectroscopic data into mixing ratio data and controls the operation of the system. The gas mixing ratio data, expressed in ppm, are displayed in real-time and continuously stored in the analyser's internal hard drive. Users can connect remotely with the analyser and control it through a standard remote desktop connection.

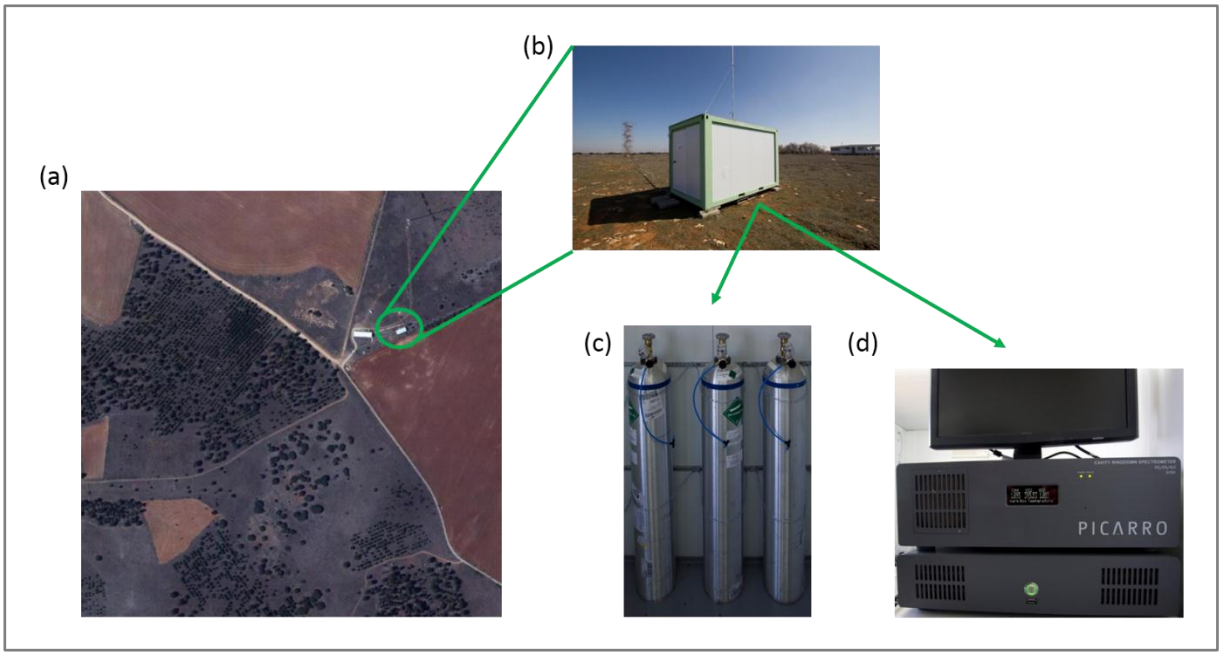

Figure 16. (a) PNOA image courtesy of © ign.es showing an aerial view of the CIBA station and the surrounding vegetation composition, (b) building with the instrumentation, (c) NOAA standard calibration gases (d) Picarro analyser G1301.

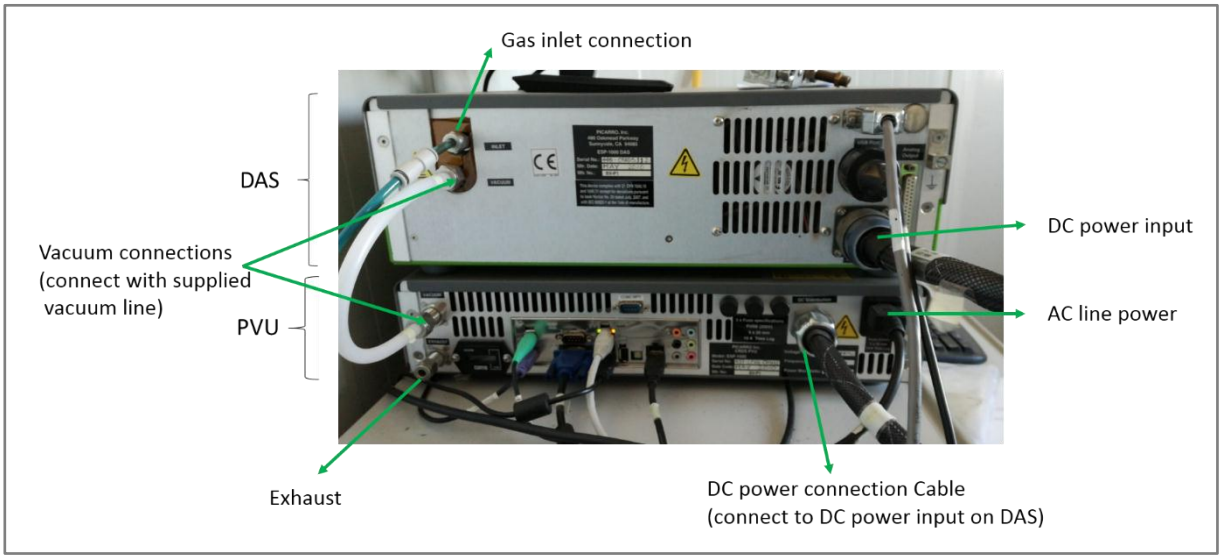

Figure 17. Main connections of the Picarro analyser G1301.

The analyser employs a near-infrared laser to measure the spectral signature of a molecule sample (Tang et al., 2015). CRDS instruments have the spectral resolution and absolute wavelength precision required to isolate and uniquely measure these spectral lines (Rella et al., 2013). Moreover, CO_2, CH_4 and H_2O absorption lines are well separated from other absorption features as well as from one another (Yver Kwok et al., 2015). Furthermore, since the laser is systematically tuned over the target absorption line during each 1 Hz measurement cycle, the intensity of the line is very accurately determined. It is important to note that the line intensity (i.e. extinction) is linearly dependent on the mixing ratio of molecules in the cavity (Woelk, 2009). Even weaker lines corresponding to molecular species containing low quantities can be measured with a high signal (Woelk, 2009). Basically, the procedure can be summarized as follows:

1. Light from a semiconductor laser diode is directed into an optical resonator cavity containing the gas sample (Rahn et al., 2008). The sampling cavity, which serves as a compact flow cell with a volume of less than 10 standard cm^3, contains three highly reflective (>99.999%) mirrors which trap the light from the laser, as shown in Figure 18a (Rella et al., 2013).

2. The sampling cavity is automatically and precisely temperature and pressure stabilized (Crosson, 2008). This ensures accurate measurements over long periods of time with minimal use of the standard calibration gases since the characteristics of the spectral lines do not vary at constant temperature and pressure conditions (Rella et al., 2013).

3. Gas molecules absorb the energy of light from the laser at a particular wavelength and generate molecular vibration and rotation. Since the frequency of the vibration and rotation movement is a function of the atom's mass, each molecule has a unique near-infrared absorption spectrum consisting of well-defined lines at different frequencies (i.e. wavelengths) (Rella et al., 2013).

4. The light re-circulates many times through the sample, travelling from and to the three mirrors within the cavity, creating a very long effective path length for the light to interact with the sample (Crosson, 2008; Yver Kwok et al., 2015). The air sample circulates inside a cavity of only 25 cm in length, where the average path length that any photon effectively travels can be over 20 kilometres. This long path length allows for measurements at a very high precision (Rella et al., 2013).

5. When the optical frequency matches the resonance frequency of the cavity, energy builds up in the cavity (Rahn et al., 2008).

6. When the signal from the detector reaches a steady state condition (i.e. the build-up is maximum), the laser is switched off (Figure 18c) (Woelk, 2009).

7. Since the mirrors do not have perfect reflection power, the light intensity inside the cavity slowly leaks out (Woelk, 2009) and the energy exponentially decreases from the cavity in time, or “rings down”, with a characteristic decay time.

8. Energy decay is then measured, as a function of time, on a photodiode located behind one of the mirrors (Yver Kwok et al., 2015).

9. The decay (or ring-down) time not only depends on cavity loss but also on the presence of any absorber species inside the cavity (Yver Kwok et al., 2015). As stated by the Beer-Lambert law, the absorption per unit length at the peak of a spectral line is proportional to the number of molecules in the gas sample (i.e. the response of the instrument is linear to increases in mole fraction) (Rella et al., 2013). The instrument records sub-picometer wavelength targeting on a microsecond timescale. The resulting spectrograms are analysed using nonlinear spectral pattern recognition routines, and the outputs of these routines are converted into gas mixing ratio data almost instantaneously (Rella et al., 2013).

10. When the laser is at a wavelength where the gas in the cavity is strongly absorbing, the ring-down time is short (Figure 18c) (Rahn et al., 2008).

11. The ring-down time is continuously repeated at several well-controlled points in wavelength. The mixing ratio is determined by a multi-parameter fit and is proportional to the gas mixing ratio (Crosson, 2008b; Jung et al., 2013). Higher concentrations of the target analyte molecule in the cavity correspond to shorter ring-down times (Yver Kwok et al., 2015).

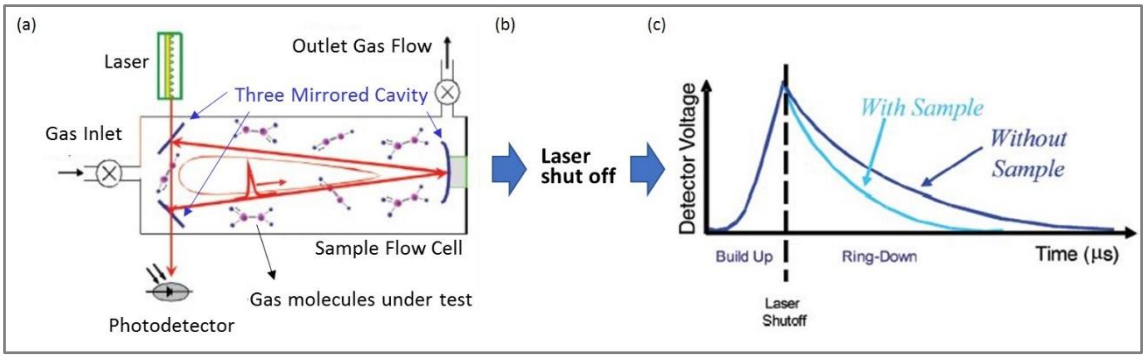

Figure 18. Schematic diagram of the CRDS working system (modified from Crosson, 2008b; Jung et al., 2013). (a) Light from a laser is trapped in a three-mirror cavity, (b) laser shut off after the process, and (c) measured absorption intensity and laser light decay over time.

The CRDS technique is therefore a measurement of time not of absorbance. Thus, any fluctuations in laser intensity have no effect on the measurement, unlike conventional spectrometers and gas analysers (Rahn et al., 2008).

4.4. Database

The database used in the current thesis consists of five and a half years (15 October 2010 to 29 February 2016) of CO_2 and CH_4 mixing ratio values collected with the Picarro analyser (G1301). Data collection is mostly complete (84% of availability), and consists of 79,263 data points. The few gaps that do exist are due to maintenance of the equipment or power failure. As regards the original contributions **I**, **II** and **III,** data were averaged in half-hour intervals. Furthermore, the dataset was divided into a diurnal and a nocturnal dataset in order to analyse and compare both scenarios. Differentiation between diurnal and nocturnal data was based on considering the GMT hour from the National Geographic Institute of Spain. As regards contribution **IV,** data were averaged in one-hour intervals and no differentiation between diurnal and nocturnal data was carried out. Furthermore, contribution **IV** considered surface wind direction data obtained from the Agroclimatic Information System for Irrigation website service (SIAR in its Spanish acronym).

The Medina de Rioseco monitoring station was considered (lat: 41º 51´ 36´´N; long: 5º 4´14´´W, alt: 731 m a.s.l.) since it is the closest meteorological station to the CIBA station (14 km NW) with data available for the study period. The station provides semi-hourly weather data at a height of 2 m a.g.l. Since the terrain in the region is very homogeneous, the conditions at both the CIBA station and the Medina de Rioseco station can be assumed to be roughly the same. Thus, wind direction surface data were used to link the CO_2 and CH_4 mixing ratio data with the arrival wind surface direction, detecting those wind surface direction sectors in which mixing ratio data are higher.

4.4.1. Data acquisition

Dry air mixing ratios of CO_2 and CH_4 are continuously collected and recorded by the Picarro analyser in the computer. The analyser software includes a valve sequencer to automatically control external solenoid valves to measure at 1.8, 3.7 and 8.3 m a.g.l. The valve level changes each 10-min. Thus, 10-min of continuous measurements were taken at each of the three levels, with around 28 measurements per minute. It should be taken into account that the first 20 data in each level were not considered in order to avoid the discontinuities produced in the recorded data when the valve level changed (Pérez et al., 2012). Thus, around 260 measurements were

considered and averaged for each height level, representing semi-hourly data. Figure 19 shows the operating scheme for the CO_2 and CH_4 data acquisition.

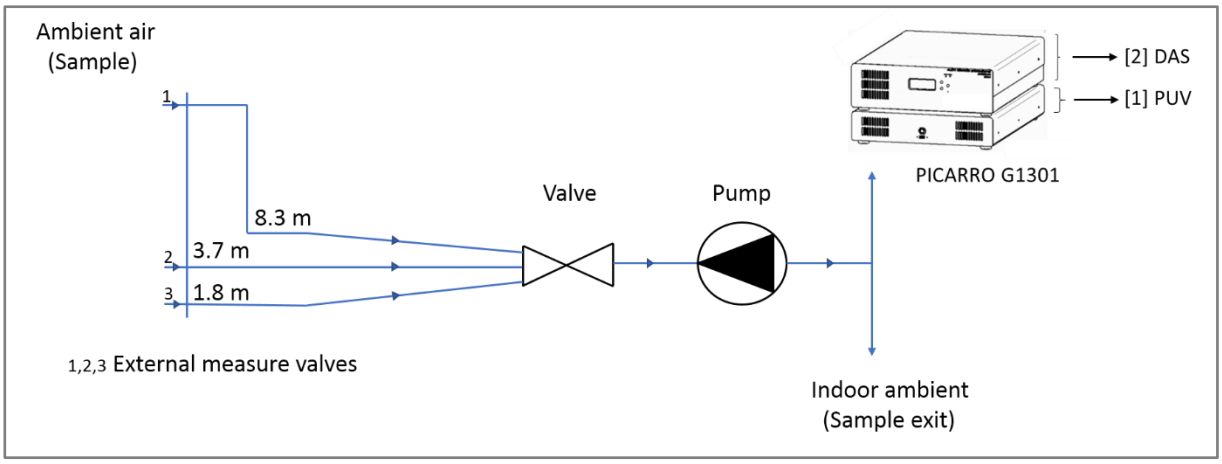

Figure 19. Operating schematic diagram of the Picarro G1301.

Contribution **I** analysed the statistical differences between the three level measurements and concluded there were no statistically significant differences at 95% confidence level when using the Fisher Least Significant Difference test. Thus, only the highest mixing ratio data (i.e. measured at 8.3 m height a.g.l.) were considered, since these are less influenced by soil roughness and soil activity.

4.4.2. Data processing

The analyser was calibrated fortnightly by injecting three standard synthetic gas mixtures calibrated by the Global Monitoring Division (GMD) of the National Oceanic & Atmospheric Administration (NOAA). Since the Picarro is extremely accurate, it is only necessary to use three calibration standards to calibrate the equipment; two points determine the calibration line and the third intermediate is used as a control point. Table 1 shows the characteristics of each standard gas employed for calibration.

Table 1. Characteristics of the three NOAA calibration gas standards used.

Gas standard	[CO_2] (ppm)	[CH_4] (ppb)
1	452.56	1990.4
2	399.27	1842.0
3	348.55	1631.0

Each standard gas was measured for five minutes and data were recorded. The first measurements were not considered in order to avoid discontinuities due to the settling-in effect (Vardag et al., 2014). No significant drift was observed in the two-week period between

calibrations, showing the high linearity and signal stability of the equipment. The calibration process is explained in detail in contribution **II** and is schematized in Figure 20.

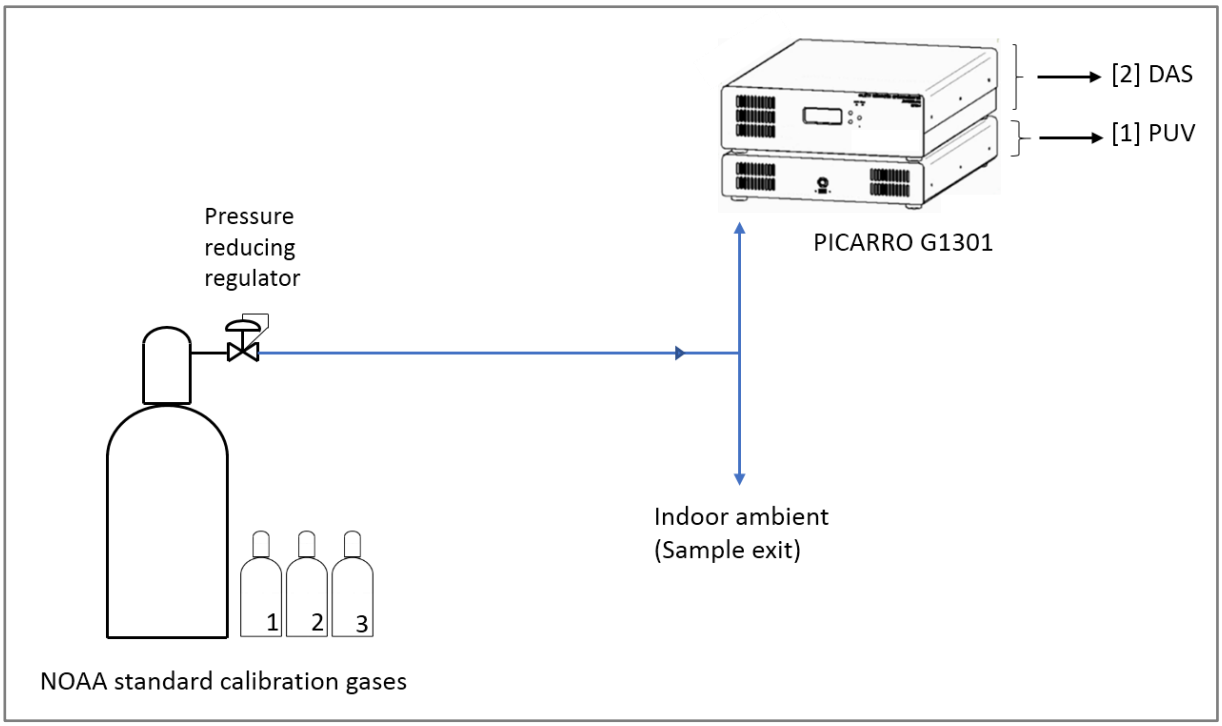

Figure 20. Calibration schematic process of the Picarro G1301.

In addition, linear regressions between NOAA's standard synthetic gases (Table 1) and the experimental values (i.e. those measured by the Picarro analyser) were used to determine their linear relationship through linear regression analysis in order to obtain the calibration equations for CO_2 and CH_4, which are the following:

$$CO_{2\,C} = 1.00341\ CO_2 - 0.17870 \quad [2]$$

$$CH_{4\,C} = 0.99197\ CH_4 + 0.01249 \quad [3]$$

where *C* indicates the corrected value.

4.5. Software employed

4.5.1. Matlab© (I)

This was used to linearly estimate the unknown coefficients of the multiple harmonic regression function (i.e. the explanatory variables) used to analyse CO_2 and CH_4 (i.e. the continuous response variable) temporal patterns.

4.5.2. Fortran (I, II, III, IV)

This was first used to separate diurnal from nocturnal data taking into account the GMT hour from the National Geographic Institute of Spain. Secondly, Fortran software was also used to implement the routines to obtain the trend (**I**, **II**, **III**), the growth rate (**I**, **II**, **III**), and the seasonal component (**I**, **II**, **III**) of the time series by using a harmonic equation (**I**), a kernel regression method (**II**) and a local regression method (**III**). Thirdly, it was used to obtain the continuous distribution functions (**IV**) as well as the distances, direction and recirculation factor of each back-trajectory (**IV**).

4.5.3. Statgraphics Centurion XVII (I, II, III, IV)

Used to conduct statistical analysis in all the original contributions.

4.5.4. Excel (I, II, III, IV)

Used to conduct statistical analysis and mathematical calculations.

4.5.5. METEX model (IV)

The Meteorological Data Explorer (METEX) web-model software, developed at the Centre for Global Environmental Research (CGER) is a powerful tool that allows for the online computation of air mass trajectories in just one submission (Zeng et al., 2010). The METEX model is a Lagrangian method based on the Petterssen method to calculate a parcel's movement (CGER METEX, 2020). The meteorological input data used to compute the backward trajectories were obtained from the Climate Forecast System version 2 developed at the Environmental Modeling Center at National Centers for Environmental Prediction (NCEP). It is a fully coupled model representing the interaction between the Earth's atmosphere, oceans, land, and sea ice. It became operational at NCEP in March 2011. This series uses data with a three-hour time resolution and a spatial resolution of 0.5x0.5 degrees at 27 different pressure levels ranging from 1 to 1000 hPa. Computation of back-trajectories using wind fields and pressure data allows us to know the approximate three-dimensional flow path of an air parcel (Hernández-Ceballos et al., 2013).

The current thesis computed 96-hourly kinematic back-trajectories arriving at the CIBA station between October 2010 and February 2016 at 500 m height a.g.l. by using the METEX air modelling software tool in order to analyse the impact of the Valladolid urban plume on the final CO_2 and CH_4 mixing ratio measured at CIBA. As stated in Lozano et al. (2012), the trajectory is simply the integration of the particle position vector in space and time that is

interpolated as the native horizontal coordinate system of meteorological data to an internal terrain coordinate following a vertical coordinate system during computation. The final position is computed from the average velocity at the initial position and the first-guess position (García-Mozo et al., 2017). METEX provides the coordinates (longitude and latitude) and height (in metres above ground level, a.g.l) of every trajectory calculated at 1-h intervals. Therefore, each 96 h trajectory is composed of 96 end-point positions. The 96 end-point positions are the position of the Lagrangian particles at a certain hour within the 96 h duration. The back-trajectories were then plotted on maps in order to visualize the atmospheric paths to the monitoring station. All data processing, statistical analyses and visualization were performed with Fortran, Statgraphics Centurion XVII and Sigmaplot 11 software.

4.5.6. Sigmaplot 11 (I, II, III, IV)

Used to depict the figures presented in all the original contributions.

4.6. Mathematical equations used

Different mathematical equations were applied to the dataset in order to separately analyse the trend, the growth rate, and the seasonal component of the time series; that is to say, the temporal patterns of the dataset.

4.6.1. Parametric equations

4.6.1.1. Harmonic equation (I)

A harmonic equation was employed to evaluate the trend, the seasonal cycle and the growth rate of the CO_2 and CH_4 mixing ratio data. The proposed equation comprises a polynomial term which express the long-term trend of the series and a sequence of four harmonics which express the seasonal cycle whilst retaining information about changes in amplitude. The first derivative of the polynomial trend expresses the growth rate of the series. The harmonic fitted curve used in contribution **I** to analyse temporal patterns is the following:

$$y = \sum_{i=0}^{3} a_i t^i + \sum_{j=1}^{4} \sum_{k=0}^{1} \left(b_{jk}\, t^k \cos(j2\pi t) + c_{jk}\, t^k \sin(j2\pi t) \right) \qquad [4]$$

where *y* reflects CO_2 or CH_4 mixing ratio data, *t* is time expressed as a fraction of year, *j* reflects the four harmonics used and *k* reflects the term in which amplitude is constant with time (*k=0*) and when it is variable over time (*k=1*).

The unknown coefficients of the multiple harmonic regression were linearly estimated running MATLAB© software. Independent variables were time (t, t^2, t^3) and the series of harmonics t^k $cos(j2\pi t)$ and t^k $sin(j2\pi t)$.

The sequence of four harmonics (j) provides information about the yearly cycle. On the one hand, the two first harmonics refer to annual behaviour. The first (wt) expresses annual behaviour and the second ($2wt$) reinforces this information, sharpening the peaks and troughs. On the other hand, the two last harmonics refer to seasonal behaviour. The third harmonic ($3wt$) expresses four-month changes, and the fourth ($4wt$) quarterly information.

4.6.1.2. Probability continuous distribution functions (IV)

A distribution function for a continuous random variable, is defined as the curve described by a mathematical equation which denotes the probability that the variable falls within a particular interval by means of areas under the curve (Everitt et al., 2010). All of the absolutely continuous functions used in contribution **IV** are skewed distributions and are described below.

4.6.1.2.1. Gamma distribution function

The gamma distribution is a generalization of the exponential distribution and is given by the following equation:

$$f(x) = \frac{(x/\beta)^{\alpha-1}\exp(-x/\beta)}{\beta\Gamma(\alpha)},\ x, \alpha, \beta > 0 \qquad [5]$$

where α represents the shape (i.e. degrees of freedom of the distribution) and β represents the scale parameter. The α and β calculation procedure is as follows:

$$D = \ln(\bar{x}) - \frac{1}{N}\sum_{i=1}^{N}\ln(x_i) \qquad [6]$$

$$\alpha = \frac{1+\sqrt{1+4D/3}}{4D} \qquad [7]$$

$$\beta = \left(\frac{\bar{x}}{\alpha}\right) \qquad [8]$$

4.6.1.2.2. Weibull distribution function

The Weibull distribution is another generalization of the exponential distribution expressed by equation 9:

$$f(x) = \left(\frac{\alpha}{\beta}\right)\left(\frac{x}{\beta}\right)^{\alpha-1}\exp\left[-\left(\frac{x}{\beta}\right)^{\alpha}\right],\ x, \alpha, \beta > 0 \qquad [9]$$

where *α* and *β* have the same meaning as for the gamma function and are calculated according to the method of moments:

$$\alpha = \left(\frac{\sigma_x}{\bar{x}}\right)^{-1.086} \quad (1 \leq \alpha \leq 10) \qquad [10]$$

$$\bar{x} = \beta\Gamma\left(1 + \frac{1}{\alpha}\right) \qquad [11]$$

4.6.1.2.3. Gumbel distribution function

The Gumbel distribution function is given by the following equation:

$$f(x) = \frac{1}{\beta}\exp\left\{-\exp\left[-\frac{(x-\zeta)}{\beta}\right] - \frac{(x-\zeta)}{\beta}\right\} \qquad [12]$$

This function presents a maximum at $x=\zeta$, and β is the scale factor. The estimation equations of both parameters are the following:

$$\zeta = \bar{x} - \gamma\beta \qquad [13]$$

where γ=0.57721 is Euler's constant (Wilks, 2019).

$$\beta = \frac{\sigma_x\sqrt{6}}{\pi} \qquad [14]$$

4.6.1.2.4. Inverse Gaussian distribution function

The inverse Gaussian distribution is described by:

$$f(x) = \sqrt{\frac{\lambda}{2\pi x^3}}\exp\left\{-\left[\frac{\lambda(x-\mu)^2}{2\mu^2 x}\right]\right\} \qquad [15]$$

where *λ* reflects the shape, and *μ* the scale parameter. Both parameters can be calculated in accordance with the Lo Brano et al. (2011) procedure:

$$\lambda = N\left[\sum_{i=1}^{N} x_i^{-1} - N^2\left(\sum_{i=1}^{N} x_i\right)^{-1}\right]^{-1} \qquad [16]$$

$$\mu = \frac{1}{N}\sum_{i=1}^{N} x_i \qquad [17]$$

4.6.1.2.5. Lognormal distribution function

The lognormal distribution function is a positively skewed function which is expressed by the following equation:

$$f(x) = \frac{1}{x\sigma_y\sqrt{2\pi}} \exp\left[-\frac{(\ln x - \mu_y)^2}{2\sigma_y^2}\right],\ x > 0 \quad [18]$$

where μy and σ_y^2, respectively, refer to the mean and standard deviation of the log-transformed variable y=ln(x) (Wilks, 2019).

4.6.1.2.6. Rayleigh distribution function

The Rayleigh distribution is a special and simplified case of the Weibull distribution where the shape parameter is assumed to be equal to two (Celik, 2004; Lo Brano et al., 2011). The Rayleigh distribution function is described by:

$$f(x) = \frac{x}{\beta^2} e^{-0.5\left(\frac{x}{\beta}\right)^2} \quad [19]$$

where ***β*** is the scale parameter, which is obtained according to the following expression:

$$\beta = \left(\frac{1}{2N}\sum_{i=1}^{N} x_i^2\right)^{\frac{1}{2}} \quad [20]$$

Since wind direction is a circular variable, circular statistics are required (Fernández-Guisuraga et al., 2016). The following three equations were used in the current thesis in order to obtain the distance, direction, and recirculation factor of the trajectories computed in original contribution **IV**.

4.6.1.3. Distance and direction trajectory analysis (IV)

The distance of every trajectory point B (x,y) to point A (x_1,y_1), which reflects the CIBA station, was obtained with the aid of point C, which reflects the North Pole. Points A, B and C together form a spherical triangle (Figure 21), where arcs *a* and *b* are part of the meridians. Arc *c*, which represents the distance between A and B, was calculated by taking into account the Earth's surface curvature by applying spherical trigonometry instead of Euclidean geometry. To fulfil this goal, the Sinnott equation was used by equation 21 (Snyder, 1987):

$$\sin\left(\frac{c}{2}\right) = \left\{\sin^2\left[\frac{(y-y_1)}{2}\right] + \cos y_1 \cos y \sin^2\left[\frac{(x-x_1)}{2}\right]\right\}^{1/2} \quad [21]$$

where y and y_1 are the latitude (in degrees) of each trajectory point and the CIBA station, respectively, x and x_1 are the longitude (in degrees) of each trajectory point and the CIBA station, respectively, and arc *c* is the distance (in m) between each trajectory point (B) and the CIBA station (A).

The longitude between the CIBA station (A) and each trajectory point (B) is obtained with the angle associated with point C by applying equation 22.

$$\cos(c) = \cos(b)\cos(a) + \sin(b)\sin(a)\cos(c) \quad [22]$$

The direction for each trajectory point was finally calculated from angle A.

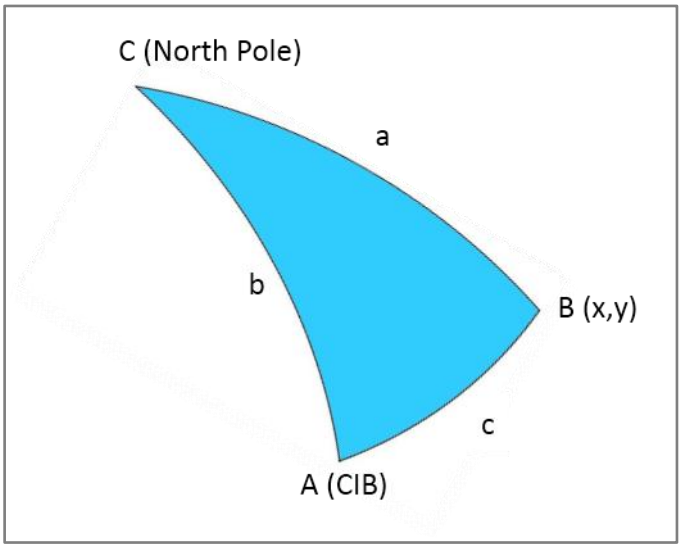

Figure 21. Spherical triangle formed by the CIBA station (A), one trajectory point (B), and the North Pole (C) to calculate the distance and direction of each trajectory point.

4.6.1.4. Recirculation factor (IV)

The recirculation factor is helpful for characterizing air pollution transport potential. The recirculation factor (RF) was calculated following the Allwine and Whiteman (1994) procedure. First, the wind run (S) was calculated as the total distance travelled by the air parcel in accordance with equation 23.

$$S = \sum_{i=1}^{24} S_i \quad [23]$$

where S_i is the distance between the consecutive hourly positions. Since trajectories are considered arcs of circumferences on the Earth's surface, the distances between the consecutive hourly positions could be obtained by applying the Sinnott expression (equation 21) and the Earth's radius (Synder, 1987). The recirculation factor (RF) could then be calculated by using equation 24.

$$RF = 1 - \frac{L}{S} \quad [24]$$

where, the resulting transport distance (*L*) is the minimum distance between the beginning and end of each trajectory. RF values vary between 0 and 1. A high RF value indicates that a site is prone to recirculation.

4.6.2. Non-parametric equations

4.6.2.1. Kernel regression functions (II)

The fitting smoothing function employed to calculate the average CO_2 and CH_4 mixing ratio, *y*, is defined by the following expression proposed by Henry et al. (2002):

$$y\,(t,h) = \frac{\sum_{i=1}^{N} K\left(\frac{t-t_i}{h}\right) y_i}{\sum_{i=1}^{N} K\left(\frac{t-t_i}{h}\right)} \qquad [25]$$

where *t* is time expressed in days, *h* is bandwidth expressed in days, *N* is the number of observations, *K* is the kernel function, and y_i reflects the mixing ratio in a specific time period t_i, expressed in days.

The kernel function determines the shape of the data while h determines their interval calculation (Everitt et al., 2010). In the kernel estimation, greater weight is given to mixing ratio data y_i observed at times t_i closer to time *t* where the average mixing ratio y(*t, h*) is obtained, whereas less weight is given to distant mixing ratio observations (Wand et al., 1995). The different kernel functions analysed in the current thesis are the following:

4.6.2.1.1. Epanechnikov kernel function

The Epanechnikov kernel is defined by:

$$K\left(\frac{t-t_i}{h}\right) = \left(\frac{3}{4}\right)\left(1 - \left(\frac{t-t_i}{h}\right)^2\right) \qquad -1 \le \frac{t-t_i}{h} \le 1 \qquad [26]$$

4.6.2.1.2. Biweight kernel function

The biweight kernel is defined by:

$$K\left(\frac{t-t_i}{h}\right) = \left(\frac{15}{16}\right)\left(1 - \left(\frac{t-t_i}{h}\right)^2\right)^2 \qquad -1 \le \frac{t-t_i}{h} \le 1 \qquad [27]$$

4.6.2.1.3. Gaussian kernel function

The Gaussian kernel is calculated by:

$$K\left(\frac{t-t_i}{h}\right) = (2\pi)^{-1/2} \exp\left(-0.5\left(\frac{t-t_i}{h}\right)^2\right) \qquad -\infty \leq \frac{t-t_i}{h} \leq \infty \qquad [28]$$

4.6.2.1.4. Rectangular kernel function

The rectangular kernel is obtained by:

$$K\left(\frac{t-t_i}{h}\right) = \left(\frac{1}{2}\right) \qquad -1 \leq \frac{t-t_i}{h} \leq 1 \qquad [29]$$

4.6.2.1.5. Triangular kernel function

The triangular kernel is expressed by:

$$K\left(\frac{t-t_i}{h}\right) = 1 - \left|\frac{t-t_i}{h}\right| \qquad -1 \leq \frac{t-t_i}{h} \leq 1 \qquad [30]$$

4.6.2.1.6. Tricubic kernel function

The tricubic kernel is expressed by:

$$K\left(\frac{t-t_i}{h}\right) = \left(\frac{70}{81}\right)\left(1 - \left|\frac{t-t_i}{h}\right|^3\right)^3 \qquad -1 \leq \frac{t-t_i}{h} \leq 1 \qquad [31]$$

4.6.2.2. Local regression equations (III)

4.6.2.2.1. Local linear regression equation (III)

The local linear regression function employed in contribution **III** may be stated as follows:

$$y = a_0 + a_1 t \qquad [32]$$

where *t* is time expressed as a fraction of years, a_0 is obtained by applying equation 33, and a_1 by applying equation 34:

$$a_0 = y'_w - a_1 t'_w \qquad [33]$$

$$a_1 = \frac{\sum_{i=1}^{N} w_i (t_i - t'_w)(y_i - y'_w)}{\sum_{i=1}^{N} w_i (t_i - t'_w)^2} \qquad [34]$$

where w_i are the weights, defined by the Epanechnikov function due to its simplicity, y_i is the mixing ratio in a time period t_i, t'_w reflects the time mean value, and y'_w the mixing ratio mean value. The fitting variable is only the time.

4.6.2.2.2. Local quadratic regression equation (III)

The local quadratic regression equation employed in contribution **III** may be expressed as follows:

$$y = b_0 + b_1 t + b_2 t^2 \quad [35]$$

where *t* is time expressed as a fraction of years, and b_0, b_1 and b_2 are the regression coefficients given by equation 36:

$$b = (X^T W X)^{-1} X^T W y \quad [36]$$

where *y* is the matrix of the mixing ratio data, *W* is the diagonal matrix containing the weights calculated by using the Epanechnikov function, and matrices *X* and *b* are defined as follows:

$$X = \begin{pmatrix} 1 & t_1 & t_1^2 \\ 1 & t_2 & t_2^2 \\ \cdots & \cdots & \cdots \\ 1 & t_n & t_n^2 \end{pmatrix} \quad [37]$$

$$b = \begin{pmatrix} b_0 \\ b_1 \\ b_2 \end{pmatrix} \quad [38]$$

The fitting variables in this method are the independent variables (time), their squares, and their cross-products.

4.7. Statistical techniques (I, II, III, IV)

4.7.1. Fisher Least Significant Difference test (I)

Since the Picarro (G1301) analyser collects data from three different height levels (i.e. 1.8, 3.7 and 8.3 m a.g.l.), the differences between the data of the three levels were analysed by employing Fisher's least significant difference (LSD) test with 95% confidence. This test helps to identify the dataset whose means are statistically different. The analysis was performed using the Statgraphics Centurion XVII software (Statpoint Technologies, Warrenton, USA). No statistical differences were found between the three levels, either for diurnal or nocturnal data with a confidence interval of 95%.

4.7.2. Linear regressions (I, III, IV)

Simple linear regressions describe the linear relationship between two variables, namely "x" and "y", where "x" is the independent, or predictor variable, and "y" is the dependent or predictand continuous variable (Wilks, 2019). In this mathematical procedure, the line

producing the least error for predictions of "y" given observations of "x" is chosen (Wilks, 2019). Linear regressions were employed to obtain CO_2 and CH_4 monthly mean trend values (mixing ratio values vs time) in contribution **I**. Contribution **III** applied linear regressions to the semi-hourly mixing ratios for the percentile values to characterize CO_2 and CH_4 diurnal and nocturnal scenarios. Contribution **IV** detrends CO_2 and CH_4 time series to calculate the main statistics and to fit them to different distribution functions. Finally, contribution **IV** determines the CO_2 and CH_4 tercile and seasonal trend and intercept values by fitting linear regressions.

4.7.3. Numerical summary measures (II, III, IV)

A list of simple robust and non-robust summary measures has been used in contributions **II**, **III** and **IV** without major computational requirements. The numerical summaries listed in this section can be divided into measures of location, spread, symmetry, and peakedness (Wilks, 2019). For each section, robust and non-robust statistics were used. It should be noted that (non) robust statistics are those statistical procedures and tests that (do not) work reasonably well even when the assumptions on which they are based are slightly transgressed (Everitt et al., 2010). The descriptive statistics listed below give rough and general information about data distribution and are commonly used to compare different datasets and to analyse whether they are characteristically similar or very different (Walford, 2011).

4.7.3.1. Location

These measures refer to the central tendency or general magnitude of the data values (Wilks, 2019). The statistics referring to the location used in the current thesis are listed below.

4.7.3.1.1. Mean (non-robust)

The mean is the central value of a dataset and is calculated as follows (Wilks, 2019):

$$\bar{x} = \frac{1}{n}\sum_{i=1}^{N} x_i \qquad [39]$$

where n is the number of data and x_i are each discrete data within the dataset.

4.7.3.1.2. Median (robust)

The median (Q_2) is the most common robust measure of central tendency (Wilks, 2019). The median represents the value that separates the upper half of the data from the lower half.

4.7.3.2. Spread

Statistics referring to the degree of dispersion around the central value (Wilks, 2019). The closer an observation is to the central value the less deviation it has (Everitt et al., 2010). The statistics that refer to the spread employed in the current thesis are set out below.

4.7.3.2.1. Minimum (non-robust)

Statistic referring to the minimum value of the dataset (Wilks, 2019).

4.7.3.2.2. Maximum (non-robust)

Statistic referring to the maximum value of the dataset (Wilks, 2019).

4.7.3.2.3. Standard deviation (non-robust)

The standard deviation is the conventional measure of scale of a dataset which measures the amount of variation or dispersion of a dataset. The standard deviation is expressed as follows (Wilks, 2019):

$$s = \sqrt{\frac{1}{n-1}\sum_{i=1}^{N}(x_i - \bar{x})^2} \qquad [40]$$

where n is the number of data, x_i are each discrete data within the dataset, and $\bar{x}$ is the mean of the dataset.

4.7.3.2.4. Upper quartile (robust)

The upper quartile (Q3) represents the data above which the 25% highest data in a dataset are found, i.e. it is the middle value between the median (Q2) and the maximum value of the dataset (Wilks, 2019).

4.7.3.2.5. Lower quartile (robust)

The lower quartile (Q1) represents the data below which the 25% lowest data in a dataset are found, i.e. it is the middle value between the median (Q2) and the minimum value of the dataset.

4.7.3.2.6. Interquartile range (robust)

The most common and simplest robust measure of spread is the interquartile range (IQ), which is a good index of the spread in the central part of a dataset since it simply specifies the range of the central half of the data. The fact that the interquartile range only considers the third and

first quartile makes this measure quite resistant to outliers. It is calculated as follows (Wilks, 2019):

$$IQ = Q_3 - Q_1 \quad [41]$$

where Q_3 and Q_1 are the upper and the lower quartile, respectively.

4.7.3.3. Symmetry

The statistics listed below reveal the balance distribution of the data around the centre value (Wilks, 2019). The two statistics used to refer to the symmetry are the following:

4.7.3.3.1. Standard skewness (non-robust)

Standard skewness is defined as the third moment of descriptive statistics and reflects the lack of symmetry in a probability distribution (Walford, 2011). A distribution presents positive (negative) skewness when it has a long tail to the right (left) meaning that there are less (more) numbers greater than the mean (Everitt et al., 2010; Walford, 2011). A large skewness value reflects that the values at one extreme exert a disproportionate influence (Walford, 2011). Standard kurtosis is obtained by applying equation 42 (Wilks, 2019).

$$\gamma = \frac{1}{n-1}\sum_{i=1}^{n}\left(\frac{x_i - \bar{x}}{s}\right)^3 \quad [42]$$

where *n* is the number of data, x_i are each discrete data, $\bar{x}$ is the mean, and *s* is the sample standard deviation.

4.7.3.3.2. Yule-Kendall index (robust)

One robust alternative for calculating the skewness of a distribution data is by calculating the Yule-Kendall index (equation 43), which is computed by comparing the distance between the median and each of the two quartiles (Wilks, 2019). A right (left) skewness is characterized by a positive (negative) Yule-Kendall index value, which means that the distance between the median is greater from the upper (lower) quartile than from the lower (upper) quartile (Wilks, 2019).

$$\gamma_{YK} = \frac{Q_1 - 2\,Q_2 + Q_3}{IQ} \quad [43]$$

where Q_1 is the lower quartile, Q_2 the median, Q_3 the upper quartile, and *IQ* the interquartile range.

4.7.3.4. Peakedness

The two statistics used to refer to the peakedness shape of the data are the following:

4.7.3.4.1. Standard kurtosis (non-robust)

Standard kurtosis is defined as the fourth moment of descriptive statistics and is a method to quantify whether one dataset is more or less peaked than another (Walford, 2011). For normal distribution, the kurtosis is known as mesokurtic, while distributions with higher values are known as leptokurtic, with those with lower values being referred to as platykurtic distributions (Westfall, 2014). Standard kurtosis is obtained by applying equation 44 (McAlevey, 2018).

$$\mathrm{k} = \frac{1}{\mathrm{n}-1}\sum_{\mathrm{i}=1}^{\mathrm{n}}\left(\frac{\mathrm{x_i}-\bar{\mathrm{x}}}{\mathrm{s}}\right)^4 \qquad [44]$$

where *n* is the number of data, x_i are each discrete data, $\bar{x}$ is the mean, and *s* is the sample standard deviation.

4.7.3.4.2. Robust kurtosis (robust)

A simple procedure for calculating the robust kurtosis in a distribution data is by employing equation 45 proposed by Sachs (1978) based on quartiles and decile statistics. For the normal distribution, the kurtosis presents a value of 0.263, and is considered a mesokurtic distribution, while distributions with higher values are referred to as platykurtic and those with lower values are known as leptokurtic (Sachs, 1978).

$$\mathrm{k_R} = \frac{\mathrm{Q_3}-\mathrm{Q_1}}{2(\mathrm{DZ_9}-\mathrm{DZ_1})} \qquad [45]$$

where Q_3 is the upper quartile, Q_1 the lower quartile, DZ_9 the 9th decile, and DZ_1 the 1st decile.

4.7.4. Terciles analysis

Tercile calculation involves calculating a dataset division that produces three equal parts of the total dataset in a series of continuous values. Contribution **IV** used a tercile data division in order to analyse and compare their trend and intercept values.

4.8. Graphical summary techniques (I, II, III, IV)

4.8.1. Box plots (I, III)

Boxplots are very widely used graphics to present a quick sketch of data distribution (Wilks, 2019). Boxplots show a large amount of information at a glance (e.g. the full range of the data, the symmetry of the data or the resistance to any outliers that might be present in the dataset)

(Wilks, 2019). In this type of graph, each box represents the interquartile range. The band in the box corresponds to the median value whereas the bottom (top) line of the box shows the lower quartile (upper quartile) value. The whiskers depict the range from the 10th to the 90th percentiles, while isolated dots indicate the 5th and 95th percentiles (i.e. the outliers of the dataset). A schematic diagram of the box plots is shown in Figure 22.

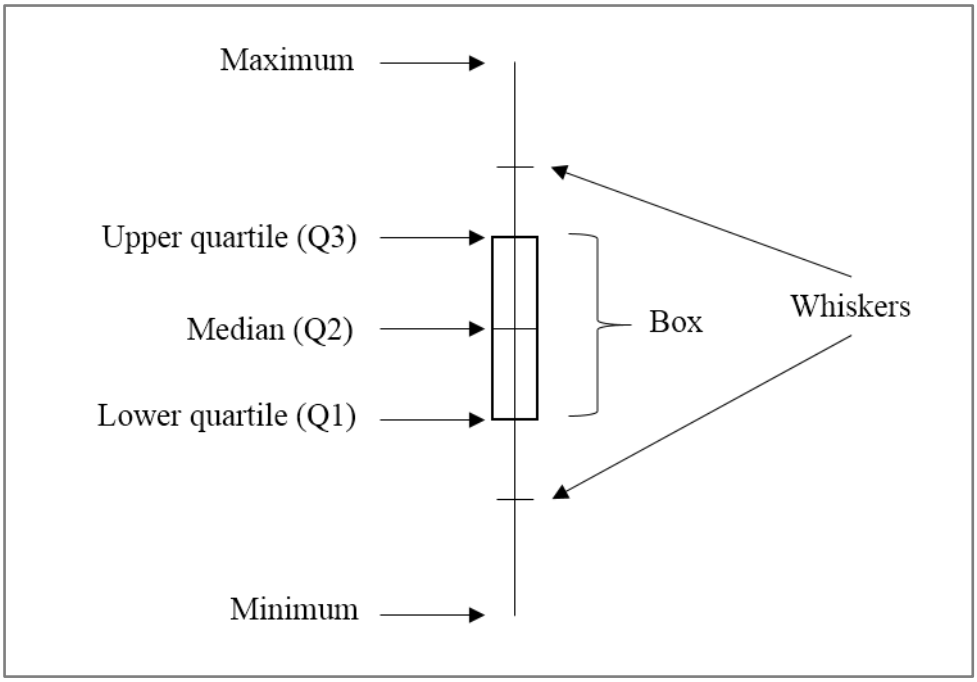

Figure 22. Box plot schematic diagram (Wilks, 2019).

4.8.2. Mixing ratio rose plots (IV)

Although not shown in the original contribution, mixing ratio rose plots were used in contribution **IV** to identify surface wind direction sectors in which the 90th CO_2 and CH_4 mixing ratio percentile values were higher. This was done in order to clarify the possible influence of the Valladolid urban plume on the final CO_2 and CH_4 measurements collected at the CIBA station.

4.8.3. Histograms (IV)

Histograms are accurate and easy representations of numerical data distribution. They are an estimation of the probability distribution of a continuous variable. The data range is divided into class intervals and the number of data falling into each interval is counted (Gramacki, 2017; Larry, 2006). The heights of the bars in the histogram are proportional to the count in each bin (Larry, 2006). Histogram plots are extremely useful tools for analysing nonlinear variables such as wind direction. Since wind direction changes continuously, it needs to be described in a statistical way as a random variable. The CO_2 and CH_4 mixing ratio histogram used in **IV** (not shown in the original contribution) consists of a series of rectangles whose widths were defined

taking into account the 16-wind surface direction sectors considered, and whose heights reveal the proportion of the whole dataset depicted in each bar in percentages (i.e. the relative frequency) (Wilks, 2019). Local maxima identification of the most frequent wind surface direction sectors was performed using histograms in contribution **IV** (not shown in the original contribution).

4.8.4. Percentile analysis

Percentile calculation involves calculating a dataset division that produces 100 equal parts of the total dataset in a series of continuous values (Everitt et al., 2010). A monthly and a semi-hourly graphical percentile evolution was carried out in contribution **III** in order to analyse the evolution of CO_2 and CH_4 over time and compare it with the seasonal cycle. Furthermore, some percentiles are useful to depict the box-plot graphs in all the contributions **(I, II, III,** and **IV)**. Finally, CO_2 and CH_4 episodes and their seasonal cycle evolution were determined through a percentile analysis in contribution **IV**.

4.8.5. Contour plots

Contour plots are topographical maps drawn from data involving observations on three variables. One variable is represented on the horizontal axis, the second on the vertical axis, while the third is represented by isolines (i.e. lines of constant value). These plots are helpful in data analysis, especially when searching for maxima or minima in the dataset (Everitt et al., 2010). Determining an optimal bandwidth procedure (contribution **II**) was based on the use of contour plots. Different bandwidth combinations, reflecting the trend (h1) in the x axis and seasonality (h2) in the y axis were tested depending on the R^2 values (the isolines) calculated between experimental and theoretical CO_2 and CH_4 mixing ratio values. Large h1 values combined with small h2 values and vice-versa, as well as intermediate values of both bandwidths were analysed. Bandwidth values ranged between 100 and 1000 days, with intervals of 100 days, for h1 and were in the range of 20 to 160 days for h2, with intervals of 20 days from level to level. The isolines plotted in the contour plot display the spatial distribution of R^2 values by applying the bandwidths established for the trend (h1) and for the seasonal component (h2). Each isoline shows a curve in which the R^2 value is constant. By using R^2 values as the statistic to determine the bandwidths, the arbitrariness of the method is substantially reduced. When the lines are close to one another, they reflect major changes in R^2 values. In contrast, when they are further apart, the change is more gradual, and R^2 values are more stable within this region. Hence, the region in which no abrupt changes in isolines was detected was chosen as the optimal bandwidth for the dataset. As a result of the contour analysis, a bandwidth of 500 days for determining the trend and the growth rate and a

bandwidth of 80 days for determining the seasonal component was considered when the kernel and the local regression methods were used to analyse temporal series evolution (contributions **II** and **III**).

4.9. Validation methods

4.9.1. Pearson product-moment coefficient of linear correlation (r-values) (II, III, IV)

This is a measure of association between two variables, "x" and "y". The Pearson product-moment coefficient of linear correlation is usually known as the "Pearson correlation coefficient" or simply as "r-values". One way to view the Pearson correlation coefficient is as the ratio of the sample covariance of the two variables to the product of the two standard deviations. The Pearson correlation coefficient is neither robust nor resistant (Wilks, 2019). It is not robust because a strong but nonlinear relationship between the two variables "x" and "y" may not be recognized. It is not resistant since it can be extremely sensitive to one or a few outlying point pairs. The calculation procedure for r-critical values is fully explained in **IV**. Pearson correlation coefficient values were calculated following equation 46.

$$\text{Correl}\,(x,y) = \frac{\sum_{i=1}^{N}(x_i-\bar{x})\,(y_i-\bar{y})}{\sqrt{\sum_{i=1}^{N}(x_i-\bar{x})^2\ \sum_{i=1}^{N}(y_i-\bar{y})^2}} \qquad [46]$$

where x_i are the experimental values, y_i the theoretical values, and the $\bar{x}$ and $\bar{y}$ coefficients, respectively, the mean values of experimental and theoretical values.

4.9.2. r- critical values (II, III, IV)

The r-critical values represent the value that a Pearson correlation coefficient value (r-value) must exceed in a sample of size n to be statistically significant at the p-value considered. The critical value determination then depends on sample size. Larger samples will be less subject to irregular sampling variations, such that the calculated critical values decline for a large amount of data: that is, smaller maximum deviations from the fitted theoretical distribution are tolerated for larger sample sizes. The r-critical values are the minimum required to reject the null hypothesis (Wilks, 2019). To calculate the r-critical values, the t-critical values for different p-values should first be obtained by using the t-Student inverse cumulative distribution function (Rouaud, 2017). r-critical values can then be calculated by using equation 47 (Sachs, 1978).

$$r = \frac{t}{\sqrt{t^2+n-2}} \qquad [47]$$

where *t* is the t-critical value, *n* is the number of data, and 2 is the degree of freedom, since we assume a two-tail distribution.

4.9.3. Coefficient of determination (R^2 values) (I, III)

The coefficient of determination is defined as the proportion of the variance in the dependent variable that is predictable from the independent variable. Contributions **I** and **III** used the R^2 values in order to determine the goodness of the hypothesis, since it provides a measure of how well observed outcomes are replicated by the functions, based on the proportion of outcomes explained by the functions. Contribution **II** used the R^2 values to determine the optimal bandwidth values for analysing the CO_2 and CH_4 temporal patterns. In addition, R^2 values were used in contribution **II** as the goodness of fit indicator to analyse the efficacy of each function kernel so as to examine the trend and the seasonal component of the time series. The R^2 values were calculated as the square of the sample Pearson product-moment coefficient of linear correlation (r-values) between the observed outcomes (the experimental data obtained with the Picarro analyser) and the observed predictor values (the theoretical values).

5. List of Original Contributions

The current thesis is based on four original contributions, which are referred to in the text with Roman numerals **(I-IV)** published in different international indexed journals. Those contributions are listed below:

I Fernández-Duque, B.; Pérez, I.A.; Sánchez, M.L.; García, M.Á.; Pardo, N., 2017. Temporal patterns of CO_2 and CH_4 in a rural area in northern Spain described by a harmonic equation over 2010–2016. *Science of the Total Environment*, 593-594, 1–9. doi: 10.1016/j.scitotenv.2017.03.132

II Fernández-Duque, B.; Pérez, I.A.; García, M.A.; Pardo, N.; Sánchez, M.L., 2019. Annual and seasonal cycles of CO_2 and CH_4 in a Mediterranean Spanish environment using different kernel functions. *Stochastic Environmental Research and Risk Assessment*, 33, 915–930. doi:10.1007/s00477-019-01655-5

III Fernández-Duque, B.; Pérez, I.A.; García, M.A.; Pardo, N.; Sánchez, M.L., 2020a. Local regressions for decomposing CO_2 and CH_4 time-series in a semi-arid ecosystem. *Atmospheric Pollution Research*, 11, 213–223. doi: 10.1016/j.apr.2019.10.012

IV Fernández-Duque, B.; Pérez, I.A.; García, M.Á.; Pardo, N.; Sánchez, M.L., 2020b. Statistical urban plume analysis using observations and air mass modelling at a rural station in the northern Spanish plateau. *Air Quality Atmosphere and Health*, 13, 1343–1350 . doi: 10.1007/s11869-020-00889-5

6. Original Contributions

6.1. Harmonic function for describing CO_2 and CH_4 temporal patterns: Original Contribution I

Fernández-Duque, B.; Pérez, I.A.; Sánchez, M.L.; García, M.Á.; Pardo, N. (2017) Temporal patterns of CO_2 and CH_4 in a rural area in northern Spain described by a harmonic equation over 2010–2016. Science of the Total Environment, 593-594: 1–9. doi: 10.1016/j.scitotenv.2017.03.132.

Análisis de los patrones temporales de CO_2 y CH_4 en un emplazamiento rural del Norte de España a través de una ecuación armónica durante 2010-2016

Resumen

Esta contribución pretende mejorar el conocimiento actual sobre la evolución del CO_2 y CH_4 en términos de tendencias, tasa de crecimiento y variaciones estacionales a nivel troposférico. Para ello, se midieron las concentraciones en seco del CO_2 y CH_4 durante cinco años y medio (del 15 de octubre de 2010 al 29 de febrero de 2016) a tres alturas distintas (1,8; 3,7 y 8,3 m.) con ayuda de un analizador Picarro en el Centro Investigación de la Baja Atmósfera (CIBA), ubicado en un emplazamiento rural de la meseta norte castellana. A fin de tener un mejor conocimiento de los patrones atmosféricos entre el día y la noche, la serie general de datos se subdividió en una serie diurna y una serie nocturna. La ecuación matemática propuesta para analizar los patrones temporales de la serie de datos fue una ecuación armónica, formada por un polinomio, que expresaba la tendencia de los datos y por una serie de armónicos, que expresaban el ciclo estacional. Las series diurna y nocturna mostraron un comportamiento diferente entre sí para ambos gases. Ambos gases revelaron un aumento en sus tasas de crecimiento durante los 5,5 años analizados. El CO_2 mostró una tendencia de crecimiento más acelerada en otoño, mientras que las tendencias del CH_4 fueron superiores durante el invierno. Finalmente, las amplitudes de la serie nocturna fueron superiores a las de la serie diurna, excepto en invierno para ambos gases y en otoño para el CH_4.

Palabras clave: meseta norte castellana, gases de efecto invernadero, series de armónicos, serie diurna y serie nocturna.

6.2. Kernel functions for describing CO_2 and CH_4 temporal patterns: Original Contribution II

Fernández-Duque, B.; Pérez, I.A.; García, M.A.; Pardo, N.; Sánchez, M.L. (2019) Annual and seasonal cycles of CO_2 and CH_4 in a Mediterranean Spanish environment using different kernel functions. Stochastic Environmental Research and Risk Assessment, 33: 915–930. doi: 10.1017/s00477-019-01655-5.

Ciclos anuales y estacionales de CO_2 y CH_4 en un entorno mediterráneo español a través del uso de diferentes ecuaciones de kernel

Resumen

Dicha contribución se basa en datos semihorarios de concentraciones de CO_2 y CH_4 registrados con un analizador Picarro G1301 entre 2010 y 2016 en el Centro de Investigación de la Baja Atmósfera (CIBA). Los principales objetivos del estudio fueron estudiar los patrones temporales del CO_2 y CH_4 mediante el uso de 6 funciones kernel así como analizar la idoneidad de cada una de las funciones para la serie de datos analizada. Las 6 funciones empleadas fueron: Epanechnikov, Gaussiana, cuártica, triangular, tricúbica y rectangular. La selección óptima del ancho de banda es crucial cuando se emplean funciones kernel. Por ello, esta contribución desarrolló un método sencillo para determinar simultáneamente el ancho de banda óptimo para analizar la tendencia y la estacionalidad de la base de datos a través del uso de gráficos de contorno utilizando los valores de R^2 como estadístico robusto en la toma de decisiones. El incremento lineal de la tasa de crecimiento para ambos gases se atribuyó principalmente al ciclo de la biosfera terrestre y de cambios en el régimen de la circulación de la atmósfera. Por su parte, el ciclo estacional reveló una variación cíclica con mínimos en el verano para ambos gases debido al mínimo biológico (CO_2) y a las mayores concentraciones de OH (CH_4). Los dos máximos nocturnos hallados para el CO_2, uno en primavera y otro en otoño, se vincularon con el aumento de las precipitaciones en ambas estaciones. En cuánto al CH_4, el máximo se encontró en invierno cuando las concentraciones de OH son mínimas. Finalmente, la función cuártica resultó ser ligeramente superior para analizar la tendencia y la Gaussiana y la triangular para analizar el ciclo estacional.

Palabras clave: tendencia, ciclo estacional, rural, funciones de kernel, ancho de banda y gráficos de contorno.

6.3. Local regression functions for describing CO_2 and CH_4 temporal patterns: Original Contribution III

Fernández-Duque, B.; Pérez, I.A.; García, M.A.; Pardo, N.; Sánchez, M.L. (2020) Local regressions for decomposing CO_2 and CH_4 time-series in a semi-arid ecosystem. Atmospheric Pollution Research, 11: 213–223. doi: 10.1016/j.apr.2019.10.012.

Regresiones locales para descomponer una serie temporal de CO_2 y CH_4 en un ecosistema semiárido

Resumen

Las regresiones locales se han utilizado ampliamente para descomponer series de datos atmosféricos. Esta tercera contribución se basa en la hipótesis de que las regresiones locales lineales son capaces de explicar la evolución temporal del CO_2 y el CH_4 en un ecosistema semiárido de la meseta norte castellana de la misma manera que lo harían las regresiones locales cuadráticas. Así, esta contribución pretende analizar la evolución temporal del CO_2 y el CH_4 a través de regresiones locales lineales y cuadráticas y comparar los resultados obtenidos con ambos métodos. Las concentraciones mínimas para ambos gases se encontraron a finales de verano, mientras que las máximas se encontraron en invierno. Al aplicar el método de regresión local lineal se obtuvieron unas tasas de crecimiento de 1.98 ppm año^{-1} para el CO_2 y de 11 ppb año^{-1} para el CH_4. Alternativamente, al aplicar el método de regresión local cuadrático se obtuvieron unas tasas de crecimiento de 2.24 ppm año^{-1} para el CO_2 y de 10.34 ppb año^{-1} para el CH_4. Los coeficientes de correlación de Pearson (r-valor) mostraron valores aceptables para ambos métodos (0.21-0.40) teniendo en cuenta la amplia base de datos con la que cuenta el estudio. Los resultados obtenidos indicaron que tanto el método lineal como el cuadrático fueron capaces de analizar satisfactoriamente la evolución de los patrones temporales de CO_2 y CH_4 sin resultar ninguno de los dos métodos superior.

Palabras clave: regresión local lineal, regresión local cuadrática, ancho de banda, series destendenciadas y r-valor.

6.4. Valladolid urban plume influence on the final CO_2 and CH_4 mixing ratios at CIBA: Original Contribution IV

Fernández-Duque, B.; Pérez, I.A.; García, M.Á.; Pardo, N.; Sánchez, M.L. (2020) Statistical urban plume analysis using observations and air mass modelling at a rural station in the northern Spanish plateau. Air Quality, Atmosphere & Health, 13: 1343–1350. doi: 10.1007/s11869-020-00889-5.

Análisis estadístico del penacho urbano a través de las observaciones y el modelado de masas de aire en una estación rural en la meseta Norte de España

Resumen

La influencia de los penachos urbanos en las concentraciones registradas en las estaciones de monitorización rurales es un tema escasamente abordado hasta la fecha. Un mayor conocimiento de la influencia de fuentes locales y regionales en las concentraciones finales de CO_2 y CH_4 atmosférico proporcionaría a los agentes políticos herramientas para una mejor toma de decisiones a la hora de elaborar políticas eficaces de mitigación contra el cambio climático. La principal motivación de esta contribución consiste en analizar el impacto del penacho urbano de Valladolid en las concentraciones finales de CO_2 y CH_4 registradas mediante un aparato de precisión (Picarro G1301) en una estación rural de la meseta norte castellana (CIBA). Para ello, se analizó la relación entre las concentraciones finales de CO_2 y CH_4 y la dirección del viento en superficie a fin de identificar posibles fuentes contaminantes. De igual modo se analizó la relación entre las concentraciones finales y la dirección del viento en altura mediante el empleo del modelo lagrangiano METEX para complementar los resultados encontrados en superficie. Las mayores concentraciones se detectaron en los sectores de dirección Sur para ambos gases poniendo de manifiesto el efecto del penacho urbano de Valladolid (localizado en dicho sector) en las concentraciones finales de CO_2 y CH_4. Finalmente, se ajustaron 6 funciones de distribución a los datos experimentales de CO_2 y CH_4 obteniendo ajustes satisfactorios con todas ellas, aunque ligeramente superiores para las distribuciones Gamma, Gumbel y Lognormal.

Palabras clave: modelado de masas de aire, CO_2, CH_4, modelo METEX, funciones de distribución y retrotrayectorias.

7. General results

7.1. CO_2 and CH_4 temporal analysis (I, II, III)

7.1.1. Global evolution

Different behaviour between diurnal and nocturnal data was found, with the highest values appearing during the night, both for CO_2 and CH_4. Table 2 shows slightly higher global mean values when the harmonic and the local functions were employed. These differences are greater in the case of CH_4. However, no important differences between all the functions employed were found.

Table 2. Mean values for all the functions used in the study.

Mathematical function	CO_2 (ppm)		CH_4 (ppb)	
	Daytime	Night-time	Daytime	Night-time
Harmonic	399.24	404.83	1906.63	1913.27
Epanechnikov kernel	396.65	402.64	1893.29	1904.09
Biweight kernel	396.62	402.60	1893.25	1903.67
Gaussian kernel	396.86	402.89	1893.86	1906.62
Gaussian (-3,3) kernel	396.86	402.89	1893.86	1906.62
Gaussian (-1,1) kernel	396.67	402.70	1893.35	1904.69
Rectangular kernel	396.69	402.73	1893.40	1904.98
Triangular kernel	396.62	402.61	1893.17	1903.94
Tricubic kernel	396.64	402.60	1893.33	1903.60
Local linear	399.65	405.89	1905.82	1919.66
Local quadratic	399.48	405.59	1904.05	1917.45

7.1.2. Trend evolution

Trend mean values were well-defined, positive and consistent over time, regardless of which mathematical function was chosen (Table 3). However, as regards the local method, some graphical discrepancies between the linear and the quadratic approach were found at the ends of the dataset **(III)**. Slightly lower mean trend values were obtained with the harmonic equation. Again, the highest values were found in the nocturnal record.

Table 3. Trend mean values for all the functions used in the study.

Mathematical function	CO_2 (ppm)		CH_4 (ppb)	
	Daytime	Night-time	Daytime	Night-time
Harmonic	392.30	398.18	1873.51	1882.21
Epanechnikov kernel	399.27	405.54	1903.03	1917.33
Biweight kernel	399.17	405.44	1902.28	1916.44
Gaussian kernel	398.81	404.92	1900.76	1914.12
Gaussian (-3,3) kernel	398.81	404.92	1900.76	1914.13
Gaussian (-1,1) kernel	399.09	405.26	1901.56	1915.76
Rectangular kernel	399.06	405.20	1901.32	1915.55
Triangular kernel	399.16	405.44	1902.15	1916.51
Tricubic kernel	399.16	405.42	1902.29	1916.28
Local linear	399.74	406.01	1906.44	1920.41
Local quadratic	399.50	405.54	1904.27	1917.44

Taking into account a statistical approach concerning the trend values, an increase in the central data trend (i.e. the mean and the median) over the study period should be pointed out. Moreover, greater data dispersion was seen for measurements taken during the middle period (2010-2014), since the standard deviation and interquartile range were higher in this period. Furthermore, symmetry indicators such as the Yule-Kendall index, showed a general right-skewness distribution, which means there are more data between the median and the upper quartile. As regards peakedness, almost negative standard kurtosis values were found for the data series, showing that our data distribution presents lighter and flatter tails than the normal distribution (DeCarlo, 1997). Robust kurtosis values above 0.263 were considered as negative robust kurtosis (Sachs, 1978). Negative robust kurtosis values were found for both CO_2 and CH_4 in most years, indicating that data distribution for the study period presents a wider peak (flatness) than normal distributions **(II)**.

7.1.3. Growth rate evolution

Growth rate values were obtained by calculating the first derivative of the trend. An increasing graphical growth rate pattern over the years was obtained with the harmonic function **(I)**. However, the kernel functions revealed an increasing graphical pattern only from 2010 to 2014, which was then followed by a decreasing graphical pattern **(II)**. As regards the local quadratic method, it showed a general increasing pattern over time although with some oscillations in the borders **(III)**. Positive growth rate values were found with slope mean values of around 2

ppm year^{-1} for CO_2 and 8 ppb year^{-1} considering all the functions listed in Table 4, except for the Gaussian function when it is limited for the interval calculation (-3,3), and which showed lower growth rate values. The same graphical behaviour was depicted for daytime and night-time records for both gases. Generally higher nocturnal growth rate values were obtained for the nocturnal dataset.

Table 4. Growth rate mean values for all the functions used in the study.

Mathematical function	CO_2 (ppm year^{-1})		CH_4 (ppb year^{-1})	
	Daytime	Night-time	Daytime	Night-time
Harmonic	2.32	2.15	11.90	10.32
Epanechnikov kernel	1.69	1.81	6.73	6.83
Biweight kernel	1.75	1.83	7.18	7.13
Gaussian kernel	0.88	0.97	3.45	3.48
Gaussian (-3,3) kernel	0.89	0.99	3.48	3.51
Gaussian (-1,1) kernel	1.58	1.69	6.09	6.25
Rectangular kernel	1.52	1.62	5.76	5.92
Triangular kernel	1.73	1.83	7.05	7.03
Tricubic kernel	1.75	1.84	7.12	7.11
Local linear	1.98	1.97	12.56	9.45
Local quadratic	2.06	2.42	11.38	9.30

7.1.4. Seasonal evolution

CO_2 evolution showed a maximum in the coldest period of the year (typically in late November-December), followed by another maximum in spring (late April – early May) which was only detectable for nocturnal records. Minimum mixing ratio values were obtained in summer (in August). As regards the CH_4 cycle, this was simpler and less pronounced than the CO_2 cycle. The highest mean mixing ratio values occurred during the winter season (December), while the lowest values occurred during the summer season (July). In addition, during the coldest months (i.e. late autumn, winter, and early spring), monthly values for the median, the first and the third quartile were above the same statistics calculated for all observations. CH_4 mixing ratios were more confined within the interquartile range than the CO_2 mixing ratio values **(III)**. Furthermore, a different behaviour in the amplitude evolution was inferred when analysing CO_2 and CH_4; with higher nocturnal CO_2 amplitudes **(I, II),** although no major differences were inferred between diurnal and nocturnal CH_4 amplitude results **(I, II)**. Furthermore, the kernel regression function revealed amplitude values that were twice their respective values when

the harmonic equation was used. Moreover, an increase in CO_2 autumnal amplitude was found during the night **(I)**. Finally, the maximum CO_2 value occurred earlier over the whole study period **(I)**, while an increase in the minimum CO_2 value over time was also found **(III)**.

7.2. Back-trajectory analysis (IV)

7.2.1. Influence of air mass origin on CO_2 and CH_4 levels

Higher mixing ratio values, considering all the raw data, were detected for both gases in the southern sectors (urban sectors), and were around 5 ppm higher for CO_2 and around 31 ppb higher for CH_4 in urban sectors. Furthermore, a directional analysis conducted through a histogram analysis revealed a peak located at around 220º associated with frequent surface wind direction from the southern sectors. This peak proved to be a prevailing wind direction in the sampling area. After detrending mixing ratios with simple linear regressions, 90th percentile values (i.e. episodes) were calculated for the 16-surface wind direction sectors established. CO_2 influence sectors were specifically found for the ESE, SE, and SSE sectors, with a mean value that was 8 ppm higher than the remaining sectors. With regard to CH_4, SE and SSE wind sectors showed mixing ratio values nearly 60 ppb higher than for the remaining sectors. Since the 90th percentile values revealed higher detrended mixing ratios for the southern sectors for both gases a possible influence of the city of Valladolid (located 24 km southeast to the CIBA) on the final CO_2 and CH_4 measurements was inferred. Thus, two different wind direction sectors were considered in order to analyse Valladolid's influence by computing the back-trajectories using the METEX model: [1] on the one hand, urban trajectories, which were expected to be influenced by the city of Valladolid urban plume, [2] on the other hand, rural trajectories which were not expected to be influenced by any major local sources in the area. The mean back-trajectory for the urban and for the rural sectors showed a westerly component due to the synoptic flow affecting the Iberian Peninsula. However, when the back-trajectories impacted the Peninsula, the rural mean back-trajectory formed an Atlantic arc over the Cantabrian range while the urban mean back-trajectory reached the Iberian Peninsula through the south-south-western wind surface sectors.

7.2.2. Statistical back-trajectory analysis

Almost all the mean statistical values for the urban sectors were below the mean statistical values for the rural sectors, both for CO_2 and for CH_4. However, as regards CO_2, the mean standard deviation for the whole study period and the mean interquartile range were around 2 ppm higher for urban sectors. The mean, median and interquartile range increased by around 2 ppm from 2011 to 2014 for the urban sectors, while the interquartile range decreased by

around 4 ppm for the same period in the rural sectors. Finally, the robust kurtosis increased for the same interval period for urban sectors, contrary to what occurred in rural sectors, although these changes were not above 0.1 ppm in any case since they are detrended values. Moreover, both sectors presented slightly leptokurtic distributions. As regards CH_4, the mean values for the whole study period for the standard deviation, interquartile range and Yule Kendall index were higher for urban sectors. As for CO_2 results, CH_4 robust kurtosis mean values showed leptokurtic data distributions (i.e. data are more concentrated with regard to the mean value and the two tails than a normal distribution, which reveals a higher occurrence of outliers), although they were close to the mesokurtic distributions for CH_4 data. Finally, CO_2 and CH_4 presented right-skewed distributions for urban and rural sectors, i.e. there are more mixing ratio data above the mean value. A mean mixing ratio for the whole study period of 406.34 ppm for CO_2 was calculated for urban sectors, compared to the 401.55 ppm calculated for rural sectors. As regards CH_4, a mean value of 1936.69 ppb for urban sectors and 1905.64 ppb for rural sectors was obtained. In almost all cases, tercile analysis showed slightly higher CO_2 slope (mixing ratio vs time) and intercept values for urban sectors. As regards CH_4 urban slope values, they were more than twofold, five-fold and nearly nine-fold their corresponding rural values for the first, second, and third tercile, respectively. As for seasonal analysis, the highest slope and intercept values were almost always found in the urban sectors. Urban intercept values were around 7 ppm for CO_2 and nearly 10 ppb for CH_4 higher than their corresponding values in rural sectors. Finally, it should be noted that the rural mean back-trajectory impacted the Iberian Peninsula after 68 hours travelling, whereas the urban mean back-trajectory impacted the Peninsula after just 56 hours travelling. However, urban back-trajectories travelled greater daily distances. As regards recirculation factor values, although most statistics were lower for urban sectors, the maximum recirculation factor value and its range were higher.

7.3. Validation indicators (I, II, III, IV)

R^2 values, r-values and r-critical values were used as validation indicators to evaluate the goodness of the techniques used in the different contributions. As regards contribution **I**, R^2 values were used to evaluate the monthly trend fit analysis. As a result, R^2 values around 1 for CO_2 and around 0.97 for CH_4 were obtained, showing no major differences between either CO_2 and CH_4 or between diurnal or nocturnal data fit. Furthermore, contribution **I** evaluated the annual amplitude growth rate evolution by again using R^2 values and showed a virtually perfect positive correlation for amplitude evolution over time. As regards contribution **II**, R^2 values, r-values and r-critical values were used as validation methods to evaluate the accuracy of each kernel function used. As a result, all the kernels studied were statistically significant,

with a p-value < 0.001. However, slightly better fits were obtained with the biweight kernel, although a worse fit was obtained with the Gaussian function since it employs the total real number line. Similar R^2 values for the Gaussian and the Gaussian limited to (- 3,3) were found. In contrast, R^2 values increased when the Gaussian was limited to (- 1,1) giving a better data fit, while computational time was cut by half. As regards seasonality, the Gaussian and the triangular kernel gave a better data fit. On the other hand, the worse fit was obtained with the rectangular and the Gaussian kernel limited to (-3,3). Shortening the interval calculation for the Gaussian kernel to (-1,1) did not prove as effective as for the trend. A better data fit was obtained for CO_2 data, both for the trend and the seasonality results. However, while slightly higher R^2 values were found for the diurnal trend values, no major differences were found for the diurnal and nocturnal seasonal values. Graphically, most of the kernel functions overlap, although two different groups were detected: [1] the first comprised the Gaussian and the Gaussian limited (-3,3), and [2] the remaining functions. As regards the growth rate graphical output, the same two groups from the trend graphical output were found, although there was also a third group formed by the rectangular and Gaussian kernel limited (-1,1) **(II)**. With regard to contribution **III**, r-values were calculated in order to assess the accuracy of the trend and the seasonal component by using the local linear and local quadratic method. As a result, virtually the same r-values (around 0.30) were obtained both for the trend or the seasonal component with the two methods. All the r-values were statistically significant, with a p-value < 0.001. The highest r-value was obtained for the CO_2 trend estimation by applying the quadratic method, whereas the lowest r-value was obtained for the CH_4 trend estimation with the linear method. Furthermore, slight statistical differences (p-value < 0.05) between the initial (T1) and the smoothed trend (T2) were found, except for CH_4 and diurnal CO_2 data when the quadratic method was used **(III)**. Finally, contribution **IV** evaluated the goodness of fit of each distribution function by means of the r-values, which proved highly satisfactory for p-values = 0.001. Results indicated that CO_2 and CH_4 data best fitted the Gumbel, the Erlang and the lognormal distributions, whereas some discrepancies were noticeable with the Gamma and Rayleigh distributions. Better fits were found for CO_2 data as well as for rural data.

8. General discussion

8.1. Temporal pattern evolution

8.1.1. Global CO_2 and CH_4 evolution

The mean annual mixing ratio at the CIBA station from 2010 to 2016 was 399.24 ± 5.05 ppm for CO_2 and 1906.63 ± 25.70 ppb for CH_4 during the daytime, and 404.83 ± 6.28 ppm (CO_2) and 1913.27 ± 24.32 ppb (CH_4) during the night-time. The mean concentrations found for CO_2 closely follow global values, 394.90 ppm, considering monthly data, while CH_4 concentrations at CIBA, which represent 1816.49 ppb, are above global mean values (NOAA, 2016). In general terms, it should be mentioned that the lowest mixing ratio values are linked with large-scale hemisphere and global background mixing ratio evolution, whereas the highest values are usually linked with local emissions (Pérez et al., 2020). More specifically, the highest CH_4 mixing ratio values reported at the CIBA station are partially due to the greater sensitivity from CH_4 emission sources at the monitoring station. Moreover, the highest nocturnal values were the result of stable nocturnal conditions and greater temperature inversions. By contrast, the convection mixing conditions during the daytime accounted for the lowest CO_2 and CH_4 values. In addition, most of the measurements taken during the study period lay in a central range, between the 30th and 60th percentile, showing few outliers in data distribution, and reflecting regular cycles at the CIBA station. The percentile analysis indicated good symmetry in the frequency distributions, since the 50th percentile value did not differ much from the average value. Finally, it should be noted that CO_2 presented more noticeable seasonal differences, which could be because of the greater variability in raw CO_2 data, due partially to the fact that the biological activity response depends on a large number of variables, whereas raw CH_4 data are more stable.

The CIBA station also revealed sharp differences between day and night. The lowest CO_2 and CH_4 mixing ratios were found during the day whereas the highest values were found at night, in agreement with Martins et al. (2016) and with other Northern Hemisphere mean values (Pu et al., 2014). These differences are most marked in the growing season (Pérez et al., 2009c). During the daytime, at the CIBA station, more intense solar radiation and thermal turbulence induces stronger vertical mixing (Fang et al., 2014) as well as the expansion of the boundary layer, which reaches its maximum height in the middle of the day (809 m), contributing to the dilution (García et al., 2016) and dispersion of both gases and decreasing their mixing ratio (Domínguez-López et al., 2015; Hernández-Ceballos et al., 2015b). CO_2 uptake and higher photochemical reactions during the day are also considered to be important causes of the

lowest CO_2 and CH_4 concentrations, respectively (Lee et al., 2012). As regards CH_4, the more intense vertical mixing during the daytime drives CH_4 transport into higher atmospheric layers where chemical reactions with OH, chlorine, and excited oxygen are more active, thereby increasing atmospheric dilution, as reported by Ginzburg et al. (2011), and thus decreasing the CH_4 mixing ratio. However, at night, radiation loss at ground level leads to a shallow stable boundary layer (Fang et al., 2013; Hernández-Paniagua et al., 2015), which reaches 405 m at CIBA, trapping CO_2 and CH_4 emissions between the ground and the top of the boundary layer and increasing their mole fraction values (Fang et al., 2013; García et al., 2012). Atmospheric mixing is low (Haszpra et al., 2008) and turbulent processes decrease. The stable atmospheric stratification conditions at night dampen vertical dispersion and favour the accumulation of locally-emitted pollutants. Frequent strong thermal inversions also play an important role in trapping CO_2 and CH_4 emissions between the ground and the top of the boundary layer, thus increasing their mole fraction values (Pérez et al., 2009b). As regards the CO_2 nocturnal maximum, night-time respiration is another important source contributor (Lee et al., 2012). In the case of CH_4, higher concentrations might be explained by the prevalence of easterly and northerly winds in the area at night. Bearing in mind that Palencia is to the northeast, that Valladolid is to the southeast and that there is an urban landfill in the south-southeast sector, the highest CH_4 concentrations during the night-time are in agreement with the main CH_4 sources in the surrounding area (García et al., 2008; 2016; Sánchez et al., 2014). Additionally, García et al. (2008) reported lower wind speed overnight, which may favour the accumulation of emissions from local sources, as also stated (Hernández-Ceballos et al., 2015b).

To analyse the CO_2 and CH_4 temporal evolution recorded at the CIBA station from 2010 to 2016, the current thesis conveniently detrended and deseasonalised the time series from the observed values, as recommended by Nakazawa et al. (1997) in order to capture the intrinsic dynamics of the time series that can be associated to different phenomena (Chham et al., 2019). As the presence of trends in the time series prevents any periodicities from being identified, removing these trends is a prerequisite for identifying periodicities (Bianchi et al., 2019). Once the CO_2 and CH_4 series is decomposed, the trend term reveals whether the mixing ratio increased or decreased over the period analysed, while the periodic term indicates which processes occur within the time series (Bianchi et al., 2019). A brief discussion concerning the temporal patterns is given below.

8.1.2. CO_2 and CH_4 trend analysis

The long term (i.e. the trend) of the equations used in the current thesis informs us about the inter-annual changes in a time series. The positive and almost linear trends reported for both

gases were also described by Buchholz et al. (2016). The greater increasing trend reported during autumn was linked with higher autumn temperatures in recent years, as a main consequence of climate change, which leads to increased respiration rates, in agreement with Piao et al. (2008) and Zhang and Zhou (2013). Furthermore, as regards CH_4 trend results, anthropogenic causes have a major impact on autumn and winter emissions.

CO_2 mean mole fractions at CIBA were around 399 ppm (392 ppm when applying the harmonic function) during the daytime and 405 ppm (398 ppm with the harmonic function) during the night-time. These values concur with global CO_2 values, which were around 395 ppm for the same period (NOAA, 2017a). As regards CH_4, daytime mole fractions were approximately 1902 ppb (1874 ppb with the harmonic function) and around 1916 ppb (1882 ppb with the harmonic function) during the night-time. These results were in agreement with CH_4 mole fraction values for latitudes above 30º N, which were over 1900 ppb in 2015 (Pérez et al., 2017), and with global CH_4 mole fraction values, which were around 1800 ppb for the same study period (NOAA, 2017b).

The upward trend reported for both gases can easily be explained on a global scale by the high annual increase in fossil fuel emissions, particularly in the northern temperate region (Anderson et al., 2016; Piao et al., 2017). CO_2 mixing ratio trends at different background sites in China have significantly increased over the past decade, with the rapid economic development and extensive increase in energy consumption likely to be the main causes (Cheng et al., 2019). On a smaller scale, the bulk of the Spanish economy is based on sectors that release large amounts of CO_2 into the atmosphere (Gutiérrez et al., 2008), contributing to the increasing CO_2 mean trend values over time. Furthermore, CH_4 emissions are the second main source of greenhouse gas emissions in Spain, as reported by Gutiérrez et al. (2008). The increasing trend pattern inferred over time at the CIBA station was already described by García et al. (2016) and may partially be linked to a rise in anthropogenic emissions from industrial activities and from the urban landfill near the monitoring station.

8.1.3. CO_2 and CH_4 growth rate analysis

As stated by Zhu and Yoshikawa-Inoue (2015), research into the growth rate requires a long recording period. The current thesis analysed a database spanning five and a half years which, according to Barlow et al. (2015), is sufficient since they consider periods of over a year and a half to be a good growth rate indicator. The positive CO_2 and CH_4 slopes, which agree well with the increases occurring worldwide, are mainly the result of emissions that have continued to grow rapidly in recent years. The range of average growth rate values, considering neither the Gaussian kernel when it is limited to the interval calculation (-3, 3), nor when it is not limited,

was narrow. However, both when limited to (- 3,3) and when not limited, the Gaussian function showed very different results compared to the other kernel functions. Yet when the Gaussian was limited to (-1,1), values doubled and approached those of the other functions, thereby improving the data fit.

CO_2 mean results yielded a positive linear increase of 1.65 ppm $year^{-1}$ during the daytime and 1.74 ppm $year^{-1}$ during the night-time, with a net growth rate (whole series) of 1.69 ppm $year^{-1}$ when considering all the mathematical functions employed. The net CO_2 growth rate obtained was slightly lower than the mean CO_2 growth rate value found for different stations worldwide (Table 5). However, differences among the three mathematical functions used can be inferred. The local linear regression function reported a net CO_2 growth rate value of 1.98 ppm $year^{-1}$, which is in line with the 2.02 ppm $year^{-1}$ mean CO_2 growth rate value for all the studies presented in Table 5. It should be noted that, whereas the harmonic and the local quadratic regression estimated a slightly higher net CO_2 growth value, the kernel regressions estimated a lower net CO_2 growth value, with the local linear regression being the method which best approximated the mean values reported in Table 5. However, regardless of the mathematical function employed, CO_2 growth rate values were more accelerated in later years, which might be the result of a rise in anthropogenic emissions from fossil fuel consumption, which has increased globally from 1920 until the present (Le Quéré et al., 2016). Moreover, local CO_2 emissions of anthropogenic activities in the surrounding area contribute to these values, although the contribution is only small compared to global background values. The nocturnal increase could be partially attributed to changes in climatology, such as the impact of heat and drought on vegetation, which leads to decreased vegetation CO_2 uptake through photosynthesis and increases in the respiration rate (Artuso et al., 2009; Heimann and Reichstein, 2008). Chamard et al. (2003) noticed a correlation between a faster CO_2 growth rate and a slower uptake by the biosphere, as we also observed (see Figure 1b and Figure 2a in contribution **III**).

Table 5. CO_2 growth rate values at different sites (modified from Pérez et al., 2017).

Site	Growth rate (ppm year^{-1})	Period	Reference
Mt. Cimone, Italy	1.66	1979-1991	Cundari et al. (1995)
Lampedusa, Italy	1.9	1992-2007	Artuso et al. (2009)
Egham, UK	2.45	2000-2012	Hernández-Paniagua et al. (2015)
Mace Head, Ireland	1.9	2000-2011	Hernández-Paniagua et al. (2015)
Cabaw, The Netherlands	2.00	2005-2009	Vermeulen et al. (2011)
Beromünster, Switzerland	2.58	2012-2016	Satar et al. (2017)
Hegyhátsál, Hungary	1.4	1981-1986	Haszpra et al. (2008)
	2.1	2003-2007	
Pallas, Finland	2.5	1996-2000	Aalto et al. (2002)
Pakistan	2.097	2002-2012	ul-Haq et al. (2017)
Central Siberia, Russia	2.02	2006-2013	Timokhina et al. (2015)
Seven sites in China	1.7-3.6	2003-2006	Zhang et al. (2008)
Northeast China	1.7	2003-2010	Wu et al. (2012)
Shangdianzi, China	2.7-3.8	2009-2013	Fang et al. (2016)
Tsukuba, Japan	2.0	1992-2003	Inoue et al. (2006)
Rishiri, Japan	2.1	2007-2012	Zhu and Yoshikawa-Inoue (2015)
Mt. Bachelor, Oregon	1.48	2012-2014	McClure et al. (2016)
Point Barrow, Alaska	1.44	1983-1985	Tans et al. (1989)
Maitri (Antarctica)	1.3	2002-2003	Jain et al. (2005)
Different sites in the Northern Hemisphere	2.04	1997-2006	Liu et al. (2015)
Globally averaged measures	1.9	2013-2014	WMO Greenhouse Gas Bulletin (2015)
	2.06	2004-2014	

For CH_4, a mean growth rate of 7.52 ppb year^{-1} for diurnal data, and 6.94 ppb year^{-1} for nocturnal outputs was found, meaning a net growth rate of 7.23 ppb year^{-1} considering all the data series. The CIBA station net growth rate value doubled the one reported at Mt. Zeppelin (Table 6) partially due to the remote location of the Norway station as well as the difference in the time period analysed. Moreover, as pointed out by Sánchez et al. (2014), the contribution of livestock in the region may be one reason why the mean growth rate is greater at the CIBA station compared to some non-disturbed areas. However, the impact of livestock in the region is not as strong as at the Beromünster tower in Switzerland (Table 6), which explains the higher CH_4 growth rate values in comparison with the CIBA values. Despite these exceptions, the net growth rate obtained at the CIBA station was in agreement with those obtained at most sampling sites worldwide. It should be noted that the kernel functions (except the Gaussian

not limited and limited to -3,3) were those which most approximated the mean CH_4 growth rate values reported at different sites worldwide (Table 6). The harmonic and local regression functions reported higher values than those reported in Table 6. Moreover, daytime and night-time series seem to be mainly influenced by the increase in local anthropogenic emissions from industrial activities, fuel burning and fugitive emissions from the urban landfill near the CIBA station. In addition, the ever-expanding human population has led to increased amounts of organic waste that release CH_4 into the atmosphere through anaerobic decomposition, thereby contributing to the observed rise (Haszpra et al., 2008). One final point to take into account is a decreasing CH_4 pattern, mainly from 2015 to 2016 and which agrees with global CH_4 growth rate values, since a decrease of around 3 ppb $year^{-1}$ was obtained on a global scale (NOAA, 2017c). Kim et al. (2015) also showed consistent changes in the global growth rate of annual CH_4 mole fractions, with ups and downs from 1980 to 2010, although the reasons are not yet fully understood.

Table 6. CH_4 growth rate values at different sites (modified from Pérez et al., 2017).

Reference	Site	Growth rate (ppb $year^{-1}$)	Period
Vermeulen et al. (2011)	Cabaw, The Netherlands	7.4	2005-2010
Satar et al. (2017)	Beromünster, Switzerland	9.79	2012-2016
Pedersen et al. (2005)	Mt. Zeppelin, Norway	3.34-3.63	1998-2005
Fang et al. (2016)	Shangdianzi, China	6-10	2009-2013
Nisbet et al. (2014)	Globally averaged	6	2007-2013
Bergamaschi et al. (2013)	30 sites worldwide	6.0	2007-2010

8.1.4. CO_2 and CH_4 seasonal cycle

Seasonal cycles showed considerable inter-annual variability with harmonic cycles, which is typical of remote locations, according to Hernández-Paniagua et al. (2015), as well as periodic behaviour and regular variations. The current thesis highlights that the evolution of CO_2 and CH_4 was clearly affected during the day and throughout the year.

8.1.4.1. CO_2 and CH_4 seasonal evolution

As regards CO_2 and CH_4 seasonal behaviour, it should be noted that the lowest mixing ratios for both greenhouse gases were found in the summer season. The minimum mixing ratio values occurred when hemispheric CO_2 uptake draws down global CO_2 mixing ratios and when CH_4 is oxidised by OH radicals through the hemisphere (Cheng et al., 2019; Pérez et al., 2020). Al-Anzi et al. (2016) also explained this behaviour because of the higher planetary boundary layer that reinforces pollutant transport and the dispersion process. During this season, solar radiation is also higher, producing good dilution from surface and thus a decrease in CO_2 and

CH_4 concentrations (García et al., 2012; Pérez et al., 2009b). Moreover, atmospheric transport flows should also be considered when seeking to understand seasonal patterns. Clean air masses approaching the monitoring station from the Atlantic are more frequent in summer, which explains CO_2 and CH_4 troughs during this season (García et al., 2016). The opposite is found for the winter season, when gases are confined within the shallow planetary boundary layer, which reaches its minimum yearly value (458 m during the daytime and 380 m during the night-time) due to lower atmospheric dispersion. Furthermore, fossil fuel burning for heating during winter also has an important effect in terms of increasing the final mixing ratio values. As regards CO_2 values, lower CO_2 uptake through photosynthesis in winter should not be ignored. Nor should plant respiration which, as stated by Pérez et al. (2016), is greater in winter. In addition, the lower production of OH radicals during winter also contributes to maximum values being reached during this season. Finally, Artuso et al. (2009) found an important influence of industrialized western Europe at the Lampedusa station from 1992 to 2007 in winter, when the vegetation sink is less effective. The same air mass origin during winter was attributed to our sampling site, since García et al. (2016) reported that the main pollutant sources lie in Europe, thereby explaining the higher CO_2 mole fractions during winter. Furthermore, different seasonal behaviour was inferred for CO_2 and CH_4.

As regards the CO_2 seasonal cycle, it is mainly dominated by the physiological activity of plants and soil respiration. On the one hand, diurnal CO_2 mixing ratios are highest in winter (maximum in December with 403 ppm) and lowest in summer (August 391 ppm). The CO_2 daytime cycle was characterized by a decline from December to August and a subsequent rise. CO_2 mixing ratios decrease more rapidly as of spring due to more intense photosynthetic activity. Coniferous trees and Mediterranean shrubs surrounding the site are particularly vigorous from May to July, promoting photosynthesis as the days grow longer and explaining the lowest CO_2 values found in August. The lowest CO_2 mixing ratio values during the summer may also be related with the intense summer heat during this season that induces alternating wind currents (Notario et al., 2014). This is in line with the findings reported by Oney et al. (2017), who found that the biosphere over the Swiss plateau tends to become a net CO_2 source when temperatures are above 20ºC (Berhanu et al., 2017). The peak in December might be due to the cumulative effects of CO_2 emission via root respiration, as suggested by Wu et al. (2012). This pattern was consistent with those of many northern hemispheric locations (e.g., Wu et al., 2012; Zhang et al., 2008). In addition, nocturnal CO_2 mole fractions increased from August to April, and then strongly decreased from May to August. This cycle was in line with that reported by Barichivich et al. (2013). Thus, two nocturnal CO_2 peaks are detected. The first is found in spring (April: 412 ppm) when the increase in temperature and precipitation regime lead to the period of maximum vegetation growth (Sánchez et al., 2005). Thus, respiration processes (Lee

et al., 2012; Pérez et al., 2016) and CO_2 soil emissions (Buragiene et al., 2015) play an important role, leading to higher mixing ratio values at night. Furthermore, this CO_2 maximum is related with strong temperature inversions at the sampling site, which help to trap CO_2 emissions in the highly stable stratified mixing layer during the night-time, particularly during the growing season and autumn (García et al., 2012). Pérez et al. (2009b) documented the influence of the Valladolid plume over the site in spring, and reported an increased gas concentration. The second maximum occurs in autumn (November, 406 ppm), as reported by Sánchez et al. (2003). These authors attribute this fact to local soil disturbances caused by ploughing the soil while preparing the land for seeding and to an increase in the amount of precipitations, as also pointed out by García et al. (2008). According to Sun et al. (2014), this peak seems to be linked to increased ecosystem productivity as well as soil microbial activity and respiration processes (Kirschke et al., 2013), which are greater during the cold season (Dalsøren et al., 2016; Hernández-Paniagua et al., 2015). Moreover, at this time of year the Palencia plume has an impact on the site although it has less of an impact on the CIBA station than the Valladolid plume due to Palencia's smaller population, its greater distance from the station and the lower amounts of industrial emissions (Pérez et al., 2009a; b; 2012). Furthermore, this second peak is also related with local emissions from vehicles, industrial activities and domestic heating, as suggested by García et al. (2016). The two CO_2 nocturnal peaks detected were also previously found by Chamard et al. (2003) who reported two maxima on the same dates (the first peak was detected in mid-May and the second in mid-November) on the island of Lampedusa (Italy) from 1992 to 2001. Furthermore, a cycle with two maxima was also described by Hatakka et al. (2003) for CO_2 mole fractions at Pallas, Finland, from 1997 to 2003. Finally, the nocturnal CO_2 minimum was found in summer (August 394 ppm), as occurs during the daytime, and was linked to a biological minimum attributed to slight plant and soil agricultural activities which, together with higher temperatures and low soil moisture, lead to lower respiration rates. Lower anthropogenic emissions during the summer due to the absence of heating and the reduction in traffic and industrial activities should also be considered (García et al., 2012). The CO_2 seasonal cycle described in the current thesis agrees with the CO_2 seasonal values reported for different observatories in the Northern Hemisphere (Table 7). It is important to bear in mind that a differentiation between diurnal and nocturnal values was analysed in the current thesis: hence, two maxima should be considered; one in November/December, and the other (only detectable in the night record) in April. Table 7 shows how the peak located in March/April is detectable at many of the sites analysed, whilst the November/December peak was mostly linked to sites surrounded by agricultural vegetation, as is the case with the main vegetation system at the CIBA station. Finally, the minimum CO_2 value was mainly located in August for all sites.

As regards CH_4 seasonal evolution, a simpler and less pronounced cycle was reported, revealing positive values from summer to winter, and negative values from winter to summer, for both daytime and night-time records. Meteorological conditions play an important role in the CH_4 cycle, since higher temperatures induce greater levels of OH radicals, which are the main CH_4 natural sink. Furthermore, the greater dispersion and convective processes occurring during the summer should be also considered. Thus, the CH_4 maximum was reached in December (around 1940 ppb) while the CH_4 minimum was found in July (around 1880 ppb). Additionally, biomass burning that begins around October in the upper Spanish plateau might influence the CH_4 cycle, as Fang et al. (2013) have suggested for other sites. In general terms, it should be noted that the CH_4 pattern described at CIBA is in line with most research campaigns conducted at different sites in the Northern Hemisphere, as reflected in Table 8, even with different types of climate pattern and vegetation cover. However, although the CIBA cycle was in line with that observed at the Mauna Loa Observatory (MLO), it should be noted that mixing ratio values at CIBA were higher than those at MLO due to the greater sensitivity from emission sources at CIBA. Sánchez et al. (2014) reported almost 200 kt $year^{-1}$ CH_4 emissions due to livestock in the region, which partially explains the higher CH_4 values at the CIBA station. Furthermore, OH radical concentration decreases with latitude in the Northern Hemisphere (Kim et al., 2015). MLO is located closer to the equator, such that the photochemical effect is stronger, causing lower CH_4 mole fractions than at the CIBA station.

8.1.4.2. Amplitude evolution

The difference between the maximum and minimum value (peak-to-trough) is defined as the amplitude of a cycle. This parameter may be considered as a biological activity indicator (Barlow et al., 2015) although it is also influenced by local sources/sinks (Li et al., 2014).

Despite an increase in the minimum CO_2 value over time being inferred, an increasing trend in the seasonal CO_2 amplitude was observed, in agreement with other observations in the Northern Hemisphere (Graven et al., 2013; Sánchez et al., 2010) such as those reported by Graven et al. (2013), Barichivich et al. (2013), and Keeling et al. (1996) at the Point Barrow station (71ºN, Alaska). As Graven et al. (2013) stated, increases in CO_2 amplitude in northern latitudes are strongly linked with the terrestrial biosphere. This amplitude increase could be linked with the increasing global warming pattern that has brought forward the onset of spring

Table 7. CO_2 evolution over different Northern Hemisphere sites (modified from Pérez et al., 2016).

Reference	Site and height a.s.l. (m)	Month (maximum)	Month (minimum)	Amplitude (ppm)	Measurement height (m)	Climate pattern	Underlying surface
Curcoll et al. (2019)	Estany Llong Lake (Spain), 2003	March	August	13.2	Flasks (3.5)	Atlantic	Mountain meadow of Festuca sp. and Nardus sp. and coniferous trees
Vermeulen et al. (2011)	Cabaw (The Netherlands), - 0.7	January	August	<25	20-200	Atlantic with soft summer	Intensively and extensively managed grassland
Uglietti et al. (2011)	Jungfraujoch (Switzerland), 3580	March	August	8.7	15	High mountain	Rock
Satar et al. (2016)	Beromünster (Switzerland), 797	March	August	13.1	Five different heights on a 212.5 m tower (12.5, 44.6, 71.5, 131.6 and 212.5).	Temperate oceanic climate	Agricultural crops
Haszpra et al. (2008)	Hegyhátsál (Hungary), 248	December	August	30	96	Temperate continental	Agricultural fields, pastures and forest patches
Eneroth et al. (2005)	Pallas (Finland), 565	February	August	15-20	7	Sub-Arctic	Pines, spruces and birches.
Tiwari et al. (2013)	Cape Rama (India), 60	November	July	<8	6 (flask)	Monsoon	Free vegetation

Table 7. Cont.

Reference	Site and height a.s.l. (m)	Month (maximum)	Month (minimum)	Amplitude (ppm)	Measurement height (m)	Climate pattern	Underlying surface
Fang et al. (2015)	LAN station (China), 160	December	August	~ 19	10	Humid subtropical monsoon	Hilly lands and farming areas with a dense vegetation coverage
Xia et al. (2015)	LAN station (China), 160	January	August	19.4	Flask	Humid subtropical monsoon	Hilly lands and farming areas with a dense vegetation coverage
Pu et al. (2014)	LAN station (China), 160	December and May	August	7.7		Humid subtropical monsoon	Hilly lands and farming areas with a dense vegetation coverage
Zhou et al. (2005)	Mount Waliguan (China), 3816	April	August	10	5(flask)-80	High mountain	Sparse vegetation, arid, grassland and desert
Zhu and Yoshikawa-Inoue (2015)	Mt. Rishiri (Japan), 35	April	August	19.7	4	Continental and maritime	Boreal forests
Murayama et al. (2003)	Japan, 1420	April	Mid August-mid September	<30	Four different heights on a 27 m tower (27, 18, 8.8 and 2.0)	Continental climate with no dry season and hot summers.	Deciduous broad-leaves such as birches and oaks. The ground surface is covered with bamboo grass.

Table 7. Cont.

Reference	Site and height a.s.l. (m)	Month (maximum)	Month (minimum)	Amplitude (ppm)	Measurement height (m)	Climate pattern	Underlying surface
Inoue et al. (2006)	Alert (Canada), 200	May	August-September	15	Flask	Polar tundra	Ice, slate and shale
Inoue et al. (2006)	Tsukuba (Japan), 25	April	August	12	200	Temperate without dry season	Grass
Higuchi et al. (2003)	Cold Bay (Alaska), 21	April	August	13	Flask	Subpolar oceanic	
Higuchi et al. (2003)	Fraserdale (Canada), 210	March-April	August	20	40	Boreal forest	Tall grass and small willow trees
Lintner et al. (2006)	Mauna Loa (Hawaii), 3397	May	September	6	7-27	High mountain	
Wada et al. (2007)	Minamitorishima (North Pacific), 9	May	September	7	10	Tropical savanna	

Table 8. CH_4 evolution over different Northern Hemisphere sites (modified from Pérez et al., 2016).

Reference	Site and height a.s.l. (m)	Month (maximum)	Month (minimum)	Amplitude (ppb)	Measurement height (m)	Climate pattern	Underlying surface
Artuso et al. (2007)	Lampedusa (Italy), 45	February-March	August	30	3	Semi-arid	Rocky, poor in vegetation
Vermeulen et al. (2011)	Cabaw (The Netherlands), -0.7	January	June, August	<150	20-200	Atlantic with soft summer	Intensively and extensively managed grassland
Haszpra et al. (2008)	Hegyhátsál (Hungary), 248	December	August	114	96	Temperate continental	Agricultural fields, pastures and forest patches
Kim et al. (2015)	Ulaan Uul (Mongolia), 1007	December-January	June-July	30	Flask	Boreal	
Kim et al. (2015)	Mauna Loa (Hawaii), 3397	November	August	31	Flask	High mountain	
Zhang and Zhou et al. (2013)	Mt. Waliguan (China), 3816	Spring/winter	August	200	80	High mountain	Sparse vegetation and arid and semiarid grassland
Zhang and Zhou et al. (2013)	Mauna Loa (Hawaii), 3397	November	August	<35	11.5	High mountain	
Zhang and Zhou et al. (2013)	Niwot Ridge (Colorado), 3523	December	July	<35		High mountain	

(Burrows et al., 2011), lengthening the vegetation growing season (Barichivich et al., 2013) in northern latitudes (Jeong et al., 2011; Piao et al., 2011). Earlier and longer growing seasons are generally associated with increased ecosystem carbon sequestration because more days are available for carbon uptake and biomass growth (Richardson et al., 2010). However, a number of studies have shown that earlier spring growth induces soil water depletion. This counteracts higher early spring carbon assimilation by enhancing mid-summer drought conditions (Angert et al., 2005; Buermann et al., 2007; Ciais et al., 2005; Hu et al., 2010; Ma et al., 2012; Peng et al., 2011; Piao et al., 2011; White and Nemani, 2003; Zhang et al., 2008) at mid to high northern latitudes, thereby inhibiting CO_2 plant uptake due to water stress (Barichivich et al., 2013). Thus, the increase in the minimum CO_2 value over time could be the result of drier and hotter summers, which induce stress in the vegetation (Angert et al., 2005) and therefore reduce plant productivity (Ahlström et al., 2015; Barichivich et al., 2013; Buermann et al., 2007; Piao et al., 2011). According to Graven et al. (2013) fossil fuels, wildfires and ocean CO_2 fluxes contribute barely a few percent to seasonal CO_2 amplitude trends, although changes in transport may cause important secondary effects. However, further studies are needed to confirm such a hypothesis since, as Forkel et al. (2016) stated, a quantitative explanation of the amplitude of the trend evolution is still lacking. This could be partially due to the shorter records from other ground monitoring stations, which rarely extend back to the 1950s (Graven et al., 2013). Mean CO_2 amplitude at the CIBA station during the daytime was 7.81 ppm and 11.45 ppm during the night-time. These results were in agreement with most of the amplitude values reported in Table 7 at different sites in the Northern Hemisphere. However, some discrepancies were found with certain locations analysed in Table 7, due to different local features, such as Hegyhátsál, the LAN station, Mt. Rishiri, and Fraserdale. The magnitude difference between the CIBA station and the Hegyhátsál site could be partially related with the lower planetary boundary layer height at Hegyhátsál, which is typically 50–200 m during the night versus the 405 m during the night at the CIBA station, which contributes to the formation of large amplitude values (Haszpra et al., 2008). As regards the LAN station (China), it should be noted that the heating seasons in China last for several months. Therefore, fossil fuel combustion for heating might result in more CO_2 emissions, which would account for the higher CO_2 amplitude values reported. Finally, a latitudinal decreasing amplitude pattern toward the south in the Northern Hemisphere should not be ignored (Zhu and Yoshikawa-Inoue, 2015). According to Graven et al. (2013), the higher the latitude in the Northern Hemisphere the greater the CO_2 amplitude changes that were reported. In this sense, seasonal CO_2 amplitude north of 45°N represented around 0.9 ± 0.1% $year^{-1}$ over the past 50 years, whereas the seasonal CO_2 amplitude increase was smaller between 35° and 45°N and was not distinguishable south of 35°N (Graven et al., 2013).

As regards CH_4 amplitude, a decreasing pattern over time was noticed although no major differences between daytime (41.54 ppb) and night-time (41.75 ppb) amplitude values were detected. The mean value of CH_4 amplitude found in the current thesis is in line with most of the sites analysed in Table 8, except for those located in intensive agricultural systems (e.g. Haszpra et al., 2008; Vermeulen et al., 2011; Zhang and Zhou, 2013) due to high CH_4 emissions at those sites. Maximum CH_4 amplitude values appeared in spring and winter, which could be attributed to the strong temperature inversions in these seasons at the CIBA station. The lowest amplitudes occur in summer, which may be associated to photochemical reactions.

8.2. Mathematical equations for analysing temporal patterns

Harmonic, kernel and locally weighted regressions proved to be useful mathematical equations for smoothing scatter diagrams to allow any structure to be seen more clearly in order to analyse CO_2 and CH_4 temporal patterns over the upper Spanish plateau. However, it is important to briefly discuss some important decisions to be taken when applying these methods in any time series.

8.2.1. Harmonic regression

As Table 9 shows, many authors have previously applied harmonic functions to describe the behaviour of pollutants in the troposphere. Nakazawa et al. (1997) suggested that the data trend should be fitted by a polynomial term of suitable degree, whereas the seasonal cycle may be described by a series of harmonic terms. Thus, the current thesis developed a function considering a third-degree polynomial to better fit the experimental data, plus a series of four harmonics to describe the CO_2 and CH_4 mixing ratio evolution in terms of annual and inter-annual changes. The two first harmonics refer to annual behaviour. The first, expresses annual behaviour and the second reinforces this information, sharpening the peaks and troughs. The two last harmonics give the seasonal evolution. The third harmonic refers to four-month changes, and the fourth to quarterly information. The main contribution of the equation proposed was to consider the amplitude of each harmonic as a constant and as a variable term along the time series since, to the best of our knowledge, the variable term has not been widely studied. Researchers who have employed four harmonics have not considered the amplitude variable over time (see Table 9), resulting in a worse fit of the data, since CO_2 and CH_4 concentrations are time-dependent variables. In contrast, those who have developed a harmonic equation in which amplitude depends on time have not considered four harmonics (see Table 9), which implies a loss of interannual information in the cycle. It is important to note that the term in which the amplitude is constant with time represents the general features of the seasonal cycle, and accounts for around 87% of the seasonal cycle (Sánchez et al.,

2010). However, the term in which the amplitude is variable along the time series reinforces the information of the constant term, thereby providing a better data fit and offering more accurate results. Thus, considering the amplitude constant and variable over time is crucial.

Table 9. Harmonic equations used in different studies worldwide (modified from Pérez et al., 2017).

Site	Trend	Harmonic part	Time	Reference
CIBA station, Spain	Linear	One harmonic	Constant and variable	Sánchez et al. (2008)
CIBA station, Spain	Linear	Two harmonics	Constant and variable	Sánchez et al. (2010)
Lampedusa, Italy	Exponential	Two harmonics	Constant	Chamard et al. (2003)
Lampedusa, Italy	Exponential	Two harmonics	Constant	Artuso et al. (2009)
Northeast China	Linear	Two harmonics	Constant and variable	Wu et al. (2012)
Different sites in the Northern Hemisphere	Linear	Two harmonics	Constant and variable	Liu et al. (2015)
Pallas, Finland	Linear	Three harmonics	Constant	Aalto et al. (2002)
Tsukuba, Japan	Fourth order	Three harmonics	Variable	Inoue et al. (2006)
Cabaw, The Netherlands	Linear	Four harmonics	Constant	Vermeulen et al. (2011)
Central Siberia, Russia	Linear	Four harmonics	Constant	Timokhina et al. (2015)
Point Barrow, Alaska	Linear	Four harmonics	Constant	Tans et al. (1998)
Mt. Waliguan, China	Second order	Four harmonics	Constant	Fang et al. (2013)
Shangdianzi, China	Second order	Four harmonics	Constant	Fang et al. (2016)
Eastern North Carolina (1992-1997)	Second order	Four harmonics	Constant	Bakwin et al. (1998)
Northern Wisconsin (1994-1997)	Second order	Four harmonics	Constant	Bakwin et al. (1998)

8.2.2. Kernel regressions

The kernel and local regression functions compensate the influence of neighbouring data by assigning higher values to data which are nearby and smaller values to data that are further away (Krisp et al., 2009). In order to employ the kernel and locally weighted regression, the

optimal bandwidth and kernel function must first be chosen (Hernández-Ceballos et al., 2019). However, there are no standards concerning such selections (Hernández-Ceballos et al., 2019).

8.2.2.1. Chosen bandwidth

The bandwidth is the distance around a case at which its influence is felt, and plays the role of the smoothing parameter fitting the data (de Haan, 1999; Hernández-Ceballos et al., 2019). Unfortunately, there is no single best method that can be universally applied to optimally determine the bandwidth (De Smith et al., 2007; Gramacki, 2018; Krisp et al., 2009) although one of the most widely used is a trial-and-error method (Fan et al., 2003; Hernández-Ceballos et al., 2019; Krisp et al., 2009). Krisp et al. (2009) consider that providing visual techniques to detect spatial patterns in data is essential vis-à-vis visually finding the most appropriate bandwidth for each particular dataset by detecting features of interest. For that reason, Krisp et al. (2009) based the chosen bandwidth on the display of maps so as to visually analyse the effect of different ranges of bandwidth values by using kernel regression equations.

Based on Krisp et al. (2009), the current thesis proposed a method drawing on contour plots to find the optimal bandwidth. The isolines plotted in the contour plot display the R^2 values between the theoretical mixing ratios obtained with the kernel regression equation and observations for each bandwidth combination. Each isoline shows a curve in which the R^2 value is constant. By applying a trial and error bandwidth selection, large bandwidth values were first tested. Their values were then reduced until fluctuations in the R^2 values disappeared in the contour plot. Thus, and as recommended by many authors (e.g. Carlos et al., 2010; Fan et al., 2003; Krisp et al., 2009; Wasserman, 2006), a data-driven choice, which kept the aim of the study closely in mind, was considered in order to establish bandwidth values. In this case, the trend bandwidth value (h1) should show annual changes, and the seasonal bandwidth value (h2) should show changes within a season. As Krisp et al. (2009) point out, experience with the data greatly improves the chosen bandwidth. Thus, Graven et al. (2012), who considered a period of 730 days and Pérez et al. (2017) who employed a bandwidth of 1000 days to detrend the data, were considered as a starting point. The bandwidth value was therefore established based on the experience combined with a trial and error test and taking into account a statistical parameter (R^2 values), which made the method more feasible by substantially reducing its arbitrariness. The h1 and h2 values were therefore chosen in the region where the contour lines were furthest apart, showing no abrupt changes in the isolines and where R^2 values are more stable.

Bandwidth values ranged between 100 and 1000 days for h1 and between 20 and 160 days for h2. Choosing high bandwidth values suppressed some details of the dataset. In other words, the estimate created substantial bias (Krisp et al., 2009). Hernández-Ceballos et al. (2019) do not recommend the use of large bandwidth values since this might introduce noise into the dataset. In contrast, when we used small bandwidth values, irregular and wiggly isolines were obtained, making it impossible to establish a stable area for R^2 values in the contour plot. The same oscillatory behaviour when applying small bandwidth values was obtained by Fan et al. (2003) and Krisp et al. (2009) due to the more significant impact of local data on the kernel estimation, which resulted in estimations that displayed substantial variance and which were dominated by noise. Even though Wand et al. (1995) stated that the larger the h, the better the estimation, we obtained smoother shapes in the contour plot for intermediate values. The inflexion point for our dataset was therefore established by choosing a 500-day bandwidth for h1 and 80 days for h2. This bandwidth finally chosen was in agreement with Krisp et al. (2009) and Peña et al. (2001), who consider intermediate bandwidth values to be the best solution in terms of reaching a compromise between bias and variance. Moreover, the h1 and h2 values proposed in the current thesis seem to be reasonable, since h1 (500-days) is around one and a half years which, according to Barlow et al. (2015), is a good indicator to express annual changes, and h2 (80 days) represents virtually one whole season. These values agree well with the results of Pérez et al. (2017), who considered a bandwidth of 500 days for h1 and 60 days for h2. According to this method, a region of possible bandwidth combination could be suggested rather than a single unique point, in line with Rodríguez-Cortés et al. (2015), who considered an interval of optimal bandwidth values after testing different bandwidth combinations. However, due to the narrow interval calculation for h1 (100 days) and h2 (20 days), no major changes were obtained for alternative surrounding h1 and h2 values, in agreement with Grange et al. (2016), who reported that within a central range of bandwidths the final output is quite insensitive to the scaling values.

8.2.2.2. Kernel regression function

Many authors (e.g. Fan et al., 2003; Peña et al., 2001; Wasserman, 2006) consider the choice of the kernel function to be of minor importance compared to the choice of the bandwidth. Fan et al. (2003) consider that as long as kernel functions are symmetric and unimodal, any kernel function performs nearly the same when the optimal bandwidth is chosen. It is important to note that all the kernel functions employed in contribution **II** are symmetric and that all of them, except the rectangular kernel, are also unimodal. Thus, in line with Fan et al. (2003) all of them should behave in the same way if the optimal bandwidth has been chosen. However, the choice of the kernel function is extremely important since it is the weighting function and is also

linked with the degree of smoothness (Table 10). It should be noted that all the kernel functions employed have finite support [−1, 1], while the Gaussian kernel has much longer effective support, since all the observations have non-zero weight. Thus, even with the same bandwidth, the Gaussian kernel can approximate the density in a different way, since it uses a different amount of information (Härdle, 1991).

Table 10. Characteristics of the kernel functions employed in contribution **II** (Peña et al., 2001; Wand et al., 1995; Wilks, 2019).

Kernel function	[a]K(u)	Support [u for which K(u) > 0]	Efficiency	Degree of smoothness
Epanechnikov	$(3/4)\ (1-u^2)$	$-1 < u < 1$	1.0000	1
Biweight	$(15/16)\ (1-u^2)^2$	$-1 < u < 1$	0.9939	2
Gaussian	$(2\pi)^{-1/2}\exp\ (-\ 0.5u^2)$	$-\infty < u < \infty$	0.9512	∞
Rectangular	1/2	$-1 < u < 1$	0.9295	0
Triangular	$1 - \lvert u\rvert$	$-1 < u < 1$	0.9859	1
Tricubic	$(70/81)\ (1 - \lvert u\rvert^3)^3$	$-1 < u < 1$	0.9870	3

[a]$u= [(t-t_i)/h]$

However, the functions in the data fit were verified in order to check how well the theoretical data describe the measurements (Fan et al., 2003). First, the r-values of all the kernel functions employed were higher than the r-critical values for the dataset and were statistically significant at a 0.001 level. Second, R^2 values were employed to study how close the estimated value, obtained with kernel functions, was to the experimental data. All the kernels were reliable and fitted the data correctly, in line with Fan et al. (2003) and García-Portugués et al. (2014) who reported minimal differences among different kernel functions when the optimal bandwidth was chosen. Furthermore, according to de Haan (1999), when an optimal bandwidth has been chosen for one type of kernel function, the same bandwidth for other kernels will show similar smoothing characteristics, and it is possible to switch between kernels without reconsidering the optimal bandwidth. However, slight differences among the kernels used were found. These are described below:

First, as regards the trend and the growth rate data, although most of the functions overlap their distributions in the graphical output, the Gaussian and the Gaussian limited to (- 3,3) behave differently from the rest of the functions. It should be borne in mind that the Gaussian kernel considers all of the observations unlike the rest of the kernel functions employed. Since the statistical weight outside the interval (-3,3) for the Gaussian kernel is nearly 0, both functions are virtually the same. Moreover, the Gaussian kernel is the function that fits the data the worst, which is partially due to the lower efficiency of this kernel (Table 10). Furthermore, because the Gaussian kernel employs all of the observations, it is computationally expensive.

Slightly better adjustments were obtained with the biweight kernel, in line with Hernández-Ceballos et al. (2019) and Peña et al. (2001), who also consider it to be a good kernel option. Furthermore, and in line with Table 10, the biweight kernel is the one that combines the highest efficiency (Wand et al., 1995; Wilks, 2019) with the highest degree of smoothing, which makes this kernel the most effective (Müller, 1988; Peña et al., 2001). These results concur with those obtained by Rodríguez-Cortés et al. (2015), who advocate the importance of the kernel function chosen in the data fit.

Second, as regards the seasonal component, the Gaussian kernel provided the best description for CO_2 daytime and CH_4 night-time data, whereas the triangular function provided a better fit for CH_4 daytime and CO_2 night-time results. In contrast, the rectangular function provided the worst data fit in almost all the cases, which might partially be due to the lowest efficiency of the kernel and to its lowest degree of smoothness (Table 10). Wand et al. (1995) point to the scant use of the rectangular kernel due to the fact that its density estimate is constant, which results in a poor data fit. Finally, it should not be ignored that the rectangular kernel exhibit jumps at the endpoints of its support (Müller, 1988), which also decreases the data fit.

Third, similar R^2 values for the Gaussian and the Gaussian limited to (-3,3) were found for the trend, growth rate and seasonal component, whereas R^2 values increased when using the Gaussian limited to (-1,1), which gave a better data fit. In addition, by shortening the Gaussian kernel to (-1,1), computational time was reduced by half without any loss of accuracy in data fitting, since observations in the range of (- 1,1) receive a weight of between 0.4 and 0.2, while observations in the range of (- 3,3) decrease their statistical weight to 0.0039 and are virtually 0 for the remaining observations (Casas, 2010).

Finally, R^2 values were higher for daytime than for night-time records. Moreover, the CO_2 data fit is better than the CH_4 data fit, which is in agreement with the results presented by Pérez et al. (2017).

8.2.3. Local weighted regressions

As regards the local weighted method, the Epanechnikov kernel was employed because of its simplicity and low computational effort, since only a fraction of the observations in the neighbourhood of the calculation points were considered. The linear method explained as much variation in CO_2 and CH_4 temporal patterns as the quadratic method did (see Tables 5 and 7 in contribution **III**). Hence, although authors such as Breaker et al. (2016) and Cleveland

et al. (1990) suggest that quadratic regressions might offer a better fit for data that have a curvature in their pattern, the results presented here point to a similar model fit for both methods. Since the linear method is easier to run computationally, while still being able to accurately reproduce data patterns as well as provide adequate smoothed points and an acceptable data fit, it might eventually replace the quadratic regression method.

8.2.4. Analysis among the mathematical equations employed for analysing the temporal patterns

Although the mathematical functions employed in the current thesis fit the experimental data well, some differences among them should be pointed out in terms of [1] smoothness, [2] computational cost and time calculation, [3] ease of use, and [4] data accuracy. Firstly, smoother trend curves were obtained with the harmonic function as well as with the Gaussian kernel since all the data contribute to the calculations, while the remaining kernel functions and the local weighted functions only consider data inside the bandwidth. Since the kernel and local regression functions are based on local calculations, they are more sensitive to gaps in the time series. Furthermore, the border effect of kernel and local functions causes less smooth graphical outputs at the start and end of the series. Secondly, the harmonic method proved to be the quickest in its computation although it considers all of the data in contrast to the kernel and the local, which only consider an interval calculation. The kernel method took longer than the harmonic regression and, particularly, the Gaussian kernel when it is not limited and when it is limited to (-3,3). However, as previously pointed out, shortening the Gaussian interval calculation to (-1,1) proved to be highly effective since, although it makes this function as costly in computational terms as the rest of the kernels analysed, it reduces computational time. In any case, the local regressions, and particularly the local quadratic regression, proved to be the slowest function method. In the same line, the harmonic function required the lowest computational resources, whereas the local quadratic regression was the most costly in computational terms. Thirdly, the harmonic regression function emerged as the easiest to implement, whereas the local quadratic regression was the most complicated due to the matrix calculation. Finally, although all the functions fit the dataset well, the harmonic functions revealed their superiority, since they gave the highest R^2 values. As regards the kernel and local regression functions, all the functions reported very similar but lower R^2 than those reported by the harmonic function.

8.3. Valladolid urban plume analysis

Although the CIBA station is a regional background site, scattered anthropogenic emissions could partly lead to the increase in the CO_2 and CH_4 mixing ratios. In addition, as stated by Cheng et al. (2019), local sources or regional transport might contribute to the presence of

CO_2 and CH_4 episodes (i.e. high mixing ratio values). Thus, an air mass analysis is recommended in order to ascertain the possible influence of the urban plume of the nearby city of Valladolid on the final CO_2 and CH_4 mixing ratio measured at the CIBA station.

8.3.1. CO_2 and CH_4 episode determination

In order to identify the CO_2 and CH_4 mixing ratio episodes which occurred during the study period, a statistical method based on the percentile calculation was applied, in line with other authors (e.g. Bianchi et al., 2019; Dimitriou, 2015; Domínguez-López et al., 2015; Hernández-Ceballos et al., 2015a; Lozano et al., 2012; Mitsakou et al., 2008). Calculating the 90^{th} percentile value as a threshold enabled rapid identification of the highest values over the time series (Hernández-Ceballos et al., 2015a; Lozano et al., 2012; San Miguel et al., 2019), which were considered episodes. Only episodes were considered for analysing the possible influence of the Valladolid urban plume on the final CO_2 and CH_4 mixing ratio values measured at the CIBA station. Once in the atmosphere, the primary process favouring the transport and dispersion of substances is wind regimes (Hernández-Ceballos et al., 2019). As stated by Liu et al. (2000), wind direction determines the travel direction of an air specie and the receptor affected at a given time.

Firstly, in order to determine the possible influence of the Valladolid urban plume on the final CO_2 and CH_4 mixing ratio measured at the CIBA station, episodes were plotted in a mixing ratio rose plot that linked the mixing ratio values with their incoming wind surface direction measured at the Medina de Rioseco weather station, in line with the method followed by Plaza et al. (2016). As stated by Yi and Hwang (2014), polar plots are useful graphs that give us an initial approximation to identifying the most likely sources, since they are located in the wind directions with the highest mixing ratio values. The highest mixing ratio values for both gases were obtained for the southern wind direction sectors, which coincides with the location of the city of Valladolid. Thus, the southern sectors were labelled as urban sectors, since the Valladolid plume could be noticed, and the remaining sectors were labelled as rural sectors, since no important sources were found.

Secondly, it should be noted that areas were not only affected by emissions where the emissions occurred but also by the contribution of air mass transport (Adame et al., 2012; Calvo et al., 2012; Cheng et al., 2019; Di Gilio et al., 2015). Calculating back-trajectories over a region provides useful guidance in estimating the transport and dispersion of air masses (Hernández-Ceballos et al., 2019; Toledano et al., 2007). Thus, in an effort to confirm the possible influence of sources from southern sectors, back-trajectories at 500 m height for the

previous 96-h were computed at the CIBA station, linking the back-trajectory paths with the final CO_2 and CH_4 mixing ratio measured at the station. Back-trajectories were calculated separately for rural and urban sectors using the METEX model so as to gain an overview of the features of long-range transport between the two wind sectors, in line with Dimitriou et al. (2017a). The current thesis used the kinematic operational model which, according to Stohl (1998), is more accurate than other operational methods such as the isobaric or isentropic methods (García-Mozo et al., 2017; Hernández-Ceballos et al., 2013). The kinematic operational model, which is widely used (e.g. García-Mozo et al., 2017; Hernández-Ceballos et al., 2013; 2015a; 2019; Lozano et al., 2012; Sorribas et al., 2015), considers that an air parcel trajectory is given by the vertical pressure velocity and horizontal wind component (Pérez et al., 2017). Moreover, Fraile et al. (2006) point out that the origin of an air parcel impacting a particular site is influenced by the altitude height considered in the back-trajectory calculation. The current thesis computed back-trajectories at 500 m a.g.l., since many authors have deemed this height to be the best for charting the behaviour of air masses circulating within the planetary boundary layer (PBL) (Adame et al., 2012; Domínguez-López et al., 2015; Hernández-Ceballos et al., 2013; 2016; Lozano et al., 2012). Furthermore, Domínguez-López et al. (2015) do not recommended calculating back-trajectories at atmospheric levels below 500 m a.g.l. due to the small NCEP file resolution. Finally, it should be noted that the backward time covered also influences the final results (Donnelly et al., 2017; Hernández-Ceballos et al., 2015) since too short a time may miss the emission sources and important air mass route crossings while too long a time introduces uncertainty into the analysis and produces misleading results. Isakar et al. (2016) consider that a week may be too long for integration time, and suggest shorter exposition times so as to obtain more detailed conclusions, particularly with regard to anthropogenic activities near the sampling site. In general, computing back-trajectories of over five days in length is not recommended due to the great uncertainty involved in the backward calculation procedure. Thus, the current thesis computed 96-hourly back-trajectories, since many authors consider this to be sufficient to cover air mass movement in the Iberian Peninsula and surrounding areas and to represent synoptic air flows without introducing too much noise (e.g. Borge et al., 2007; Dimitriou et al., 2017b; Domínguez-López et al., 2015; Lozano et al., 2012; San Miguel et al., 2019).

8.3.2. Influence of air mass origin on CO_2 and CH_4 levels

Mean trajectories for the study period were obtained in order to simplify data analysis (Domínguez-López et al., 2014; Hernández-Ceballos et al., 2013; 2015a; Lozano et al., 2012; San Miguel et al., 2019). Furthermore, due to the large number of back-trajectories computed, the influence of each trajectory's error calculation on the uncertainty in the overall results was minimized (Hernández-Ceballos et al., 2013). All the back-trajectories contained in the

southern sectors were then averaged to show the mean urban back-trajectory whereas the remaining back-trajectories (those not lying in the southern sectors) were averaged to show the mean rural back-trajectory. Urban trajectories were expected to be influenced by the city of Valladolid urban plume, whereas rural trajectories are not influenced by any major local sources in the area. The pathway drawn by the mean back-trajectory allowed for a more refined interpretation of air mass arrival in the study area (Adame et al., 2012). As stated by García-Mozo et al. (2017), differences between mixing ratio values provide a distinction between local and external contributions, giving a clearer idea of the origin of the mixing ratio measured at the station. The contrast between the lowest mixing ratios found for the rural sectors and the highest mixing ratios found for the urban sectors could be explained in terms of [1] the trajectories' paths, [2] the time and distance travelled by the back-trajectories, and [3] the recirculation factor.

[1] It is important to note that the air parcels of both wind sectors have a westerly component, mainly due to the influence of the Azores anticyclone located between 30 and 45° N, to the west of the Iberian Peninsula (Fernández-Raga et al., 2010). The Azores anticyclone induces nearly zonal trajectories from the west to the east, typical of mid-latitude Northern Hemisphere sites (Adame et al., 2015; Hernández-Ceballos et al., 2016; Notario et al., 2014), which explains the high frequency of westerly air mass arrivals at the monitoring station. Furthermore, many authors have also highlighted the effect of the orography (e.g. Hernández-Ceballos et al., 2015a; 2016; 2019; Izquierdo et al., 2017; Pérez et al., 2018a; Valverde et al., 2016) on the transport, accumulation and dispersal of air substances. The mountain ranges surrounding the monitoring station led to restrictions in the movement of the arriving flow. The western direction is free from orographic barriers, while the eastern direction presents a more complex topography. The Iberian and Central ranges substantially condition the airflow reaching the site, while the Cantabrian range exerted less of an effect (Pérez et al., 2015a). Despite the initial westerly air flow for the rural and urban sectors, some differences between the two sectors could be inferred.

The mean rural trajectory comes from the Atlantic Ocean, and enters through the north of the Iberian Peninsula via the Cantabria Sea. This finding is in agreement with Notario et al. (2014) who also detected frequent air trajectories coming from the North, with an annual occurrence of around 20% in Castilla La Mancha (Spain). The arrival of northern circulations over the Iberian Peninsula is mainly related with two different synoptic configurations: (1) the presence of an intensive low system over western Europe, from the Mediterranean area to Scandinavia, which is usually reinforced by the Azores anticyclone, and (2) the presence of an intensive

high system over the British Isles connecting the north with the south of western Europe (Hernández-Ceballos et al., 2013). The western and northern origin of the rural mean back-trajectory exerts an important influence on the lowest mixing ratio detected for the rural sectors since, as stated by many authors (e.g. Alonso-Blanco et al., 2018; Donnelly et al., 2017; Fernández-Camacho et al., 2016; García et al., 2012; Ghasemifard et al., 2019; Kim et al., 2015; Lozano et al., 2012; Pérez et al., 2018c; Srivastava et al., 2015), trajectories with an oceanic or marine origin load low levels of pollutants. Moreover, the eastern North Atlantic was listed as one of the cleanest regions in the Northern Hemisphere according to a study of air mass modelling at the Mace Head station in Ireland (Pérez et al., 2015b). In the same line, northern advections (Lozano et al., 2012) are also considered to be clean air flows which lead to low final mixing ratios. Finally, it should be pointed out that in the rural sectors there were no important anthropogenic sources in close vicinity to the CIBA, which also explains the lower mixing ratio values found in those sectors.

The mean urban back-trajectory comes from the west, and travels from the Atlantic Ocean and west of the Iberian Peninsula, entering through the southern sectors. Since urban trajectories also have an initial flow from the Atlantic Ocean, they would be expected to carry clean air (Ghasemifard et al., 2019). However, the mean urban air trajectory changed direction in the last 24-hours prior to reaching the CIBA station, and headed towards the southern sectors. Even at the CIBA station, where the wind flow is not influenced by mountainous relief, wind twist angles also exert an influence due to the combined effects of the Coriolis force (owing to the Earth's rotation), the friction force generated by the Earth's surface roughness, and the pressure gradient force (Liu et al., 2019). Under their influences, the wind direction twists along height, leading to a spiral-shaped wind flow, which is commonly known as the Ekman spiral (Liu et al., 2019). Since back-trajectories were computed at 500 m height a.g.l., the Ekman spiral effect is noticeable. As height increased, there is a directional clockwise shift in the Northern Hemisphere (Hernández-Ceballos et al., 2016). Liu et al. (2019) showed that wind direction can veer up to 60º clockwise over the first 1000 m in height. Taking this deviation into account, the air flow corresponding to the previous day impacting the CIBA station, as regards urban sectors, which show a SSW origin (cyan line in Figure 23), would have a SE origin after correcting the twist angle of 60º in an anti-clockwise direction, as pointed out by Liu et al. (2019). Since the city of Valladolid is located in the SE wind sector, the Valladolid urban plume is expected to increase the final CO_2 and CH_4 mixing ratio values recorded at the station. Moreover, this continental flow is expected to be linked to lower wind speed values (Pérez et al., 2018b) and therefore higher final mixing ratio values. These results were in line with those reported by other authors (e.g. García et al., 2016; Lozano et al., 2012; Pérez et al., 2018a) who stated that local trajectories (i.e. trajectories confined within the Peninsula) are normally

characterized by stagnant conditions, leading to higher mixing ratio values. Finally, it should be mentioned that Pérez et al. (2009b) obtained higher results for the Richardson number for the Valladolid sector, which implies lower mixing with the environment and, therefore, less dilution effect resulting in higher mixing ratios in the southern wind sectors.

[2] As pointed out by Likuku (2006), the time required for air masses to travel before reaching a specific site is strongly correlated with the final mixing ratio recorded (Lozano et al., 2012). In this sense, the rural mean back-trajectory requires more time and a greater distance to impact the Iberian Peninsula. Thus, as Adame et al. (2015) stated, the pollutant mixing ratio for rural sectors was diluted along its longer path over the Atlantic, leading to lower mixing ratios. Moreover, the longer straight trajectories, normally linked with ocean trajectories (Notario et al., 2014), imply higher wind speed values (Pérez et al., 2018b), thus increasing the dispersive conditions and leading to relatively good air quality (Baldasano et al., 2014; Dimitriou et al., 2018), which also explains the lower final mixing ratios in rural sectors. As regards the urban sectors, the higher mean distance travelled by the mean back-trajectory was expected to induce a greater dilution effect due to its mixing with ambient air (Adame et al., 2015; Fiedler et al., 2009), leading to lower mixing ratio values, in contrast to the highest mixing ratios found for the urban sectors. The influence of Valladolid on the final CO_2 and CH_4 mixing ratios detected in the urban sectors could explain this fact, reinforcing the initial hypothesis concerning the presence of urban emissions coming from southern directions matching the city of Valladolid (around 300,000 inhabitants) and located 24 km SE of the CIBA station, as also pointed out by Pérez et al. (2015c). This concurs with Notario et al. (2014), who stated that air pollution emissions from urban and industrial areas have a regional or even a global effect. Furthermore, as regards CH_4, according to Ghasemifard et al. (2019) anthropogenic sources are the main sources of CH_4 contribution in Western Europe. The monitoring station is also influenced by the urban landfill which lies in the same direction as Valladolid, some 20 km from the station and whose fugitive emissions were around 7.11 kt $year^{-1}$ for 2011 (Sánchez et al., 2014). Hernández-Paniagua et al. (2015) also linked the presence of a local landfill with high CO_2 and CH_4 mixing ratios at Egham in the UK. It should not be forgotten that the CIBA station is located in a region where livestock plays an important role (García et al., 2016; Sánchez et al., 2014). Sánchez et al. (2014) reported almost 200 kt $year^{-1}$ CH_4 emissions due to livestock in the region, which partially explains the higher CH_4 values at the CIBA station. Although the urban mean back-trajectory travelled a longer distance than the rural mean back-trajectory when considering the 96-h computed, it should be noted that a shorter time and distance is required by the urban mean back-trajectory to reach the Iberian Peninsula. This means that the urban air mass has less mixing over the clean Atlantic Ocean whilst, in contrast,

it spends more time within the Iberian Peninsula, dragging more continental pollutants (Pérez et al., 2009b) and contributing to the highest CO_2 and CH_4 mixing ratio values in the southern sectors.

[3] Recirculation is an event in which polluted air is initially carried away from the source, and later returns to the initial point, leading to higher mixing ratio values. Recirculation depends on changes in wind direction (Kumar et al., 2013), which influences pollutant dispersion (Dekhtyareva et al., 2016). The lower the recirculation factor values, the lower the expected mixing ratio results. Despite the lower mean and median recirculation values found for southern sectors compared to rural sectors, the curve path of the mean urban back-trajectory for the last 24-hours before impacting the CIBA station (Figure 23) indicates air mass recirculation (van Drooge et al., 2016). The SE wind sector was linked to the lowest wind speed and, as stated by Surkova (2013), recirculation is more active where wind speed is low, leading to the accumulation of emission products around the source. This agrees with the more complex behaviour of the Valladolid urban plume, which exhibits a meandering trajectory as well as recirculation processes, as reported by Pérez et al. (2011). This partially accounts for the higher mixing ratio values found for the southern sectors. Finally, maximum and range values were higher for urban sectors, which could be due to the presence of sporadic episodes with high mixing ratio values from urban sectors.

Statistical analysis of the urban and rural sectors also reflected the strength of the Valladolid urban plume and its effects on the final CO_2 and CH_4 mixing ratios measured at the CIBA station. On the one hand, CO_2 and CH_4 standard deviation and interquartile values showed greater data dispersion around the mean values for the urban sectors, which could explain the presence of sporadic episodes with high mixing ratio values in the urban sectors. The highest slope and intercept mixing ratio values for the urban sectors also reflect the influence of the Valladolid urban plume. It should be noted that the slope refers to the trend which mainly reflects the anthropogenic causes contributing to the already mentioned increase in greenhouse gases in recent years (Bergamaschi et al., 2013; Haszpra et al., 2008). These results are in line with those found by Pérez et al. (2009b), who reported mixing ratio median values that were 8 ppm higher in the Valladolid sector compared to the rest of sectors. This influence seems to be more evident for CH_4, which can be explained by fugitive emissions from the nearby city of Valladolid landfill. Finally, the six distribution functions employed in our dataset to analyse the CO_2 and CH_4 mixing ratio at the CIBA station fit the experimental data well (p-values = 0.001). However, some differences were seen among the functions used. The best data fit was obtained using the Gamma distribution, whereas the worst data fit was obtained when using the Inverse Gaussian, regardless of the sector or gas under study.

Moreover, as Celik (2004) and Jamil et al. (1995) showed, a similar behaviour between the Rayleigh and the Weibull distributions was detected for our dataset. Due to this similar behaviour, there is no reason to prefer one method over another. Furthermore, the best fit was obtained for the rural sectors due to the more confined CO_2 and CH_4 values, whereas urban sectors are characterized by the presence of CO_2 and CH_4 episodes (i.e. high mixing ratio values), which explain the worse data fit obtained. To conclude, as Menon et al. (2018) state, the statistical distribution function to which the experimental data can fit depends on the location, the pollutant features and the meteorological synoptic situations.

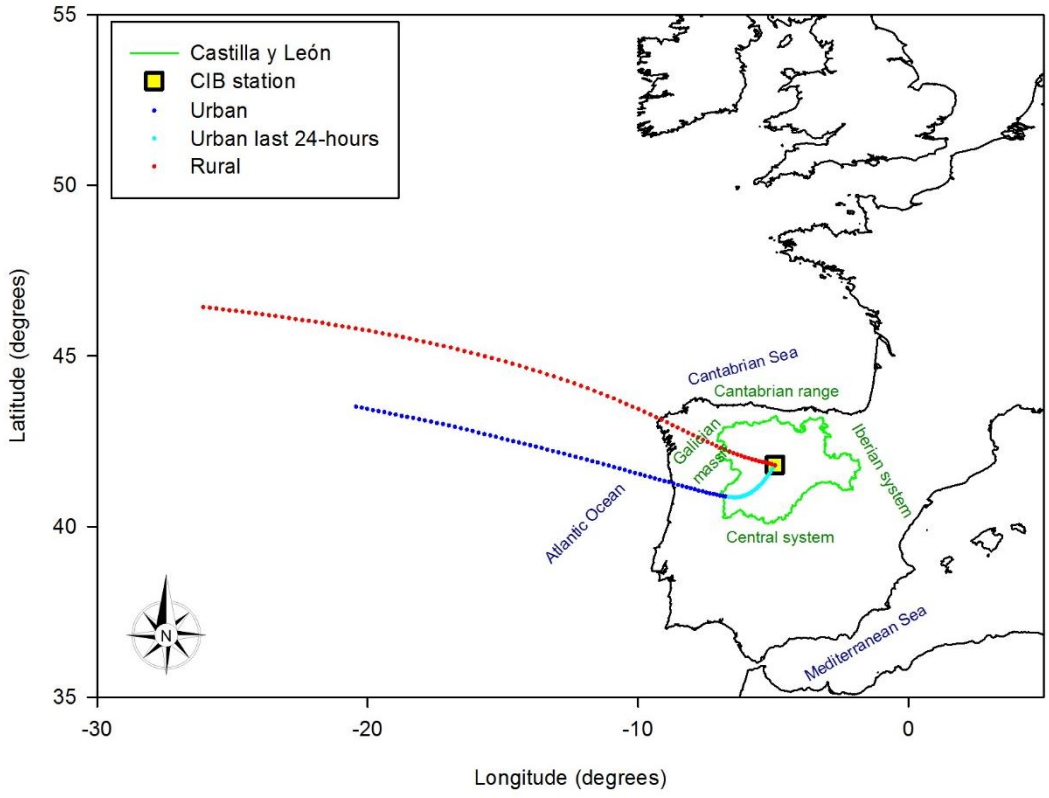

Figure 23. Urban and rural mean back-trajectories at 500 m a.s.l. computed with the METEX model at the CIBA station during the period Oct 2010–Feb 2016.

Finally, it should be pointed out that the computation of back-trajectories together with surface wind observations sought to combine regional and local approaches which, together with the geographical distribution of the sources, allowed a possible identification of the sources responsible (Hernández-Ceballos et al., 2014a; b). It is important to take into account that air modelling tools (Donnelly et al., 2017; Katsoulis, 1999) give a rough approximation of air mass history since calculating air mass trajectories is based purely on meteorological fields which only show the movement path of air masses (Hernández-Ceballos et al., 2019; Webster et al., 2012). Therefore, observations are crucial for assessing and improving the quality of plume transport results (Schumann et al., 2011).

9. Conclusions / Conclusiones

9.1. Conclusions

The main goal of the current thesis is to characterize the temporal patterns of a five and half year CO_2 and CH_4 mixing ratio time series over the upper Spanish plateau using different mathematical functions. Briefly, a linear growth rate evolution showed increases of around 2 ppm $year^{-1}$ for CO_2 and 7 ppb $year^{-1}$ for CH_4, which are partially due to anthropogenic emissions from fossil fuel consumption and other industrial activities on a global and local scale. Moreover, regular intra-annual variations for the CO_2 and CH_4 evolution were reported. Only one maximum was found for CO_2 in December for diurnal records, whereas at night two maximums were found; the first in April and the second in November linked to the increase in precipitation, which increases the respiration rate due to greater vegetation development. The minimum CO_2 mixing ratio was observed in late summer, both for diurnal or nocturnal records, when vegetation uptake reaches its maximum activity. As regards CH_4, peaks were found in December when OH concentration is minimum, and troughs were found in July when OH concentration is maximum. These cycles were the result of many overlapping factors mainly related with biological ecosystem changes (soil humidity, respiration process, amount of precipitation), anthropogenic local sources (urban plumes, urban landfill and surrounding agricultural activities), and atmospheric patterns (height of the planetary boundary layer or turbulent processes). Finally, major differences between day and night-time records were also detected. The lowest mixing ratio values were found during the daytime, partially due to thermal turbulence and higher planetary boundary layer height, which increases dispersion processes. In contrast, the highest values at night were linked to stable stratification, lower planetary boundary layer height and thermal inversions that trap emissions near the ground. Focusing on CO_2, the influence of the terrestrial ecosystem was apparent, and contributed to lower values during the daytime due to photosynthesis, and higher values at night-time due to soil and plant respiration. As regards CH_4, minimum mixing ratio values were found during the day when OH production was maximum, contrary to what occurred at night.

In addition, the results presented in the previous sections point to the following conclusions, which are aligned with the six specific objectives considered for the current thesis.

I The harmonic function composed of a third-degree polynomial plus a series of four harmonics proved to be optimal for describing CO_2 and CH_4 mixing ratio evolution in terms of annual and inter-annual changes. The main contribution of the equation

proposed was that the amplitude of each harmonic was considered as a constant and as a variable term with time since, to the best of our knowledge, the variable term with time has not been widely employed when four harmonics are considered. Although the term in which the amplitude is constant with time represents the general features of the seasonal cycle, the term in which the amplitude is variable over time reinforces the information. This endows the data with a better fit and offers more accurate results, since CO_2 and CH_4 mixing ratios are time-dependent variables. Thus, considering both constant and variable amplitude over time is crucial.

II Selecting the optimal bandwidth proves key in kernel regressions in terms of achieving good data interpretation. The current thesis recommends choosing the bandwidth based on the special characteristics of the dataset and not based on the typical values used in the literature. Thus, a novel procedure based on a visual selection of bandwidth values using contour plots was proposed. The method combined good theoretical properties since it was based on a statistical parameter (R^2 values) with strong practical performance, low computational resources and low calculation speed, whilst also proving easy to use. One of the most notable contributions of the method proposed was that it allowed two optimal bandwidths to be determined at the same time; one for considering the trend and the other for considering the seasonal component. However, although the method proved to be optimal, further inquiry is needed to gain a more precise bandwidth determination.

III No major differences affecting temporal pattern interpretation were found among the six kernel functions employed. However, slightly better fits were obtained with the biweight kernel since it is the one that combines the greatest efficiency with the highest degree of smoothness. In contrast, the rectangular function provided the worst data fit in almost all cases, which might partially be due to the lowest efficiency of the kernel and to its lowest degree of smoothness. Moreover, the rectangular kernel presents jumps at the endpoints of its support, thereby also decreasing its data fit. The differences between the kernels for the seasonal component were lower than those for the trend, which could be due to the more regular intra-annual variations. Since R^2 values were very similar for the six kernels, we recommend using those which involve less computational effort. It is important to point out that all the kernels employed entail virtually the same computational effort, except the Gaussian kernel, which needs additional run-time since it employs all the observations. Shortening the

interval calculation to (- 3,3) did not prove successful either in terms of decreasing calculation speed or for an increase in R^2 values, since the statistical weight outside the interval (-3,3) is nearly 0. As a result, this function is nearly the same as when the interval calculation is not limited. However, when the interval calculation was limited to (-1,1), R^2 values increased substantially and approached the values obtained with the other kernel functions for the trend and growth rate. In addition, time calculation was reduced by half without losing accuracy in data fitting since observations outside the (- 1,1) range receive a very low statistical weight for the observations. As regards the seasonal component, R^2 did not improve. As a result, in general terms limiting the interval calculation to (- 1,1) significantly increased the flexibility of the Gaussian kernel, making its calculation computationally feasible.

IV

The use of the Epanechnikov weight when applying local linear and quadratic regressions led to easier and lower computational implementation, making it feasible to run our long time series. However, running the quadratic regression was computationally more expensive than running the linear method. The results presented in the current thesis indicate that both the linear and the quadratic method capture the CO_2 and CH_4 temporal pattern evolution well and that neither emerged as superior. Thus, the local linear method might eventually replace the local quadratic method given its simpler operation and the less expensive calculations involved.

V

Some differences among the three mathematical regression functions employed were found in terms of [1] smoothness, [2] computational cost and time calculation, [3] ease of use, and [4] data accuracy. Firstly, smoother trend curves were obtained with the harmonic and the Gaussian kernel function since all the data contribute to the calculations, whereas the remaining kernel functions and the local weighted functions are based on local calculations and are therefore more sensitive to gaps in the time series. Furthermore, the border effect of kernel and local functions causes less smooth graphical outputs at the start and end of the series. Secondly, the harmonic method proved to be the quickest in its computation and the one that requires fewest computational resources. The kernel method requires more time calculation than the harmonic regression. This is also particularly true of the Gaussian kernel method when it is not limited or when it is limited to (-3,3). In any case, local regressions, and particularly the local quadratic regression, required the highest computational resources and time calculation. Thirdly, the harmonic regression

function proved to be the easiest to implement, whereas the local quadratic regression was the most complicated due to the matrix calculation involved. Finally, although all the functions fit the dataset well, the harmonic function revealed its superiority due to the highest R^2 values obtained. As regards the kernel functions and the local regression functions, all the functions reported very similar R^2, although these were lower than those reported by the harmonic function.

VI

The contrast between the lowest mixing ratios found for the rural sectors and the highest mixing ratios for the urban sectors was explained by the trajectories' paths, and by the time and distance travelled by the back-trajectories until they impacted the CIBA station. Although an initial westerly flow was observed for both sectors, a different path between urban and rural back-trajectories was found when they impact the Iberian Peninsula, since urban trajectories showed a south-southwesterly component, whereas rural sectors showed a northerly component. Urban trajectories spent longer travelling over the Iberian Peninsula, which results in more pollutants being dragged than in rural trajectories, which have a more oceanic and marine character and are therefore expected to be cleaner. Furthermore, the recirculation of the urban mean back-trajectory in the final 24 h before impacting the CIBA station should not be ignored, as this might increase the pollutant levels dragged. The highest mixing ratios found for the urban sectors therefore reflect the influence of the Valladolid urban plume. Furthermore, the METEX model proved to be a quick and easy technique that requires few computational resources for analysing the influence of the Valladolid urban plume on the final CO_2 and CH_4 levels measured at the rural CIBA station.

Overall, the current thesis has demonstrated the effectiveness of applying harmonic, kernel and local weighted regressions to describe the temporal variability of CO_2 and CH_4 in a Mediterranean background station of the northern Spanish plateau between 2010 and 2016, thereby fulfilling the main objective of this doctoral thesis. However, the mathematical functions used should not be seen as competitors. In fact the current thesis considers it interesting to employ more than one function so as to ensure results are consistent and free from bias. In addition, the combination of CO_2 and CH_4 observations, wind surface data and the computation of back-trajectories emerged as a very useful method for understanding urban plume effects on CO_2 and CH_4 temporal patterns. The results obtained in the current thesis are crucial vis-à-vis understanding the processes that govern CO_2 and CH_4 cycles, which is essential for implementing an effective climate policy to deal with climate change. Although these types of

studies are site-dependent due to the specific local conditions occurring over each site, they are necessary in order to better understand the evolution of mixing ratio change over certain areas, particularly those collected at background stations, such as the CIBA station. Further investigation, coupled with a denser monitoring network, is needed to better understand and assess the evolution of these gases over time. Thus, we consider it important to extend the use of the statistical methods employed in the current thesis in order to determine the temporal patterns of these gases in other areas. Their application may improve current knowledge of temporal patterns worldwide and help to gain a better insight into how gases evolve in the low atmosphere. In addition, the results presented here could be greatly improved by extending the data series. Hence, maintaining the CIBA monitoring station proves crucial in terms of providing a better understanding and assessment of how these gases evolve over time.

9.2. Conclusiones

El objetivo principal de la presente tesis fue caracterizar los patrones temporales de una base de datos de concentraciones de CO_2 y CH_4 que abarca 5,5 años en un emplazamiento ubicado en la meseta norte castellana mediante el empleo de diferentes funciones matemáticas. El incremento encontrado de las tasas de crecimiento de 2 ppm año^{-1} para el CO_2 y de 7 ppb año^{-1} para el CH_4 se debió en gran parte a las emisiones antropogénicas a escala global y/o local. Por otro lado, se detectaron variaciones intraanuales periódicas en la evolución de ambos gases. En el caso del CO_2 sólo se detectó un máximo en diciembre para los datos diurnos mientras que para los datos nocturnos se detectaron dos máximos, uno en abril y otro en noviembre vinculados ambos al aumento del régimen hídrico que llevó consigo un aumento en la tasa de respiración debido al mayor desarrollo de la vegetación. Las concentraciones mínimas de CO_2 se observaron a finales de verano, tanto en los datos diurnos como en los nocturnos, cuando la absorción de CO_2 por parte de la vegetación alcanza sus mayores tasas. En lo referente al CH_4, los máximos se encontraron en diciembre cuando la concentración de OH es mínima, mientras que las concentraciones de CH_4 fueron mínimas en el mes de julio cuando la concentración de OH es máxima. Los ciclos de CO_2 y CH_4 fueron el resultado de varios factores superpuestos como son los cambios en los ecosistemas biológicos (humedad en el suelo, tasas de respiración o régimen hídrico), fuentes locales antropogénicas (penachos urbanos o actividades antrópicas circundantes) y cambios atmosféricos (altura de la capa límite de la atmosfera o presencia de procesos turbulentos). De igual modo cabe destacar el diferente comportamiento entre los registros diurnos y nocturnos para ambos gases. Los valores más bajos de concentración se encontraron durante el día, debido en parte a la turbulencia térmica y a la mayor altura de la capa límite de la atmósfera aumentando con ello los procesos dispersivos. Por el contrario, los valores más elevados de concentración se detectaron durante la noche debido en parte a la estable estratificación que se produce en dicha parte del día, una menor altura de la capa límite de la atmósfera y a las mayores inversiones térmicas que atrapan las emisiones producidas cerca del suelo. Centrándonos en el CO_2, la influencia de los ecosistemas terrestres es aparente, contribuyendo a los valores más bajos durante el día debido a los procesos fotosintéticos, mientas que los valores más altos registrados durante la noche se debieron a la respiración del suelo y de las plantas. En cuanto al CH_4, los valores mínimos de concentración detectados durante el día se deben a la máxima producción de radicales OH durante dicha parte del día, al contrario de lo que ocurre durante la noche.

A continuación, se resumen las principales conclusiones presentadas en los apartados anteriores y que se encuentran alineadas con los seis objetivos específicos de la presente tesis doctoral.

I La función armónica compuesta por un polinomio de tercer grado y una serie de cuatro armónicos resultó ser óptima para describir la evolución de los patrones temporales de las concentraciones de CO_2 y CH_4. La principal contribución de la ecuación propuesta fue que la amplitud de cada armónico se consideró como un término constante y otro variable con el tiempo, ya que, hasta dónde sabemos el término variable con el tiempo no ha sido ampliamente utilizado en este tipo de funciones cuando se consideran 4 armónicos como en nuestro caso. A pesar de que el término en el que la amplitud es constante en el tiempo representa las características generales del ciclo estacional, el término en el que la amplitud es variable con el tiempo refuerza dicha información logrando con ello un mejor ajuste de los datos y ofreciendo resultados más precisos ya que las concentraciones de CO_2 y CH_4 varían en función del tiempo. Por lo tanto, considerar la amplitud con términos constantes y variables en el tiempo es vital.

II La selección del ancho de banda óptimo resulta clave en las regresiones de kernel para una buena interpretación de los datos. La presente tesis recomienda elegir el ancho de banda en función de las características especiales del conjunto de datos disponible y no en función de los valores típicos utilizados en la literatura. Por lo tanto, se propuso un procedimiento novedoso basado en la selección visual de los valores de ancho de banda mediante el empleo de gráficos de contorno. El método propuesto se basa en un parámetro estadístico (R^2) requiriendo bajos recursos computacionales, baja velocidad de cálculo y de fácil uso. Una de las aportaciones más destacadas del método propuesto es que permite determinar dos anchos de banda simultáneamente, uno para considerar la tendencia y otro para considerar el componente estacional. Sin embargo, aunque el método demostró ser óptimo, se necesitan más investigaciones al respecto para lograr una determinación más precisa del ancho de banda.

III No se encontraron diferencias significativas que afecten a la interpretación de los patrones temporales de CO_2 y CH_4 al aplicar las 6 funciones de kernel al conjunto de datos. Sin embargo, se obtuvieron ajustes ligeramente superiores con la función

cuártica ya que es la función que combina la mayor eficiencia con el mayor grado de suavidad. En cambio, la función rectangular proporcionó el peor ajuste en casi todos los casos, lo que podría deberse a la menor eficiencia del núcleo y a su menor grado de suavidad. Además, la función rectangular presenta saltos en los extremos de su intervalo de cálculo lo que dificulta el ajuste a los datos experimentales. Las diferencias entre las funciones empleadas para analizar el ciclo estacional fueron menores que las encontradas para analizar la tendencia, lo que podría deberse a la mayor regularidad de las variaciones intraanuales. Dado que los valores de R^2 fueron muy similares para las 6 funciones, recomendamos utilizar aquellas que implican un menor esfuerzo computacional. En este sentido, cabe destacar que prácticamente todas las funciones empleadas conllevan el mismo esfuerzo computacional, excepto la función Gaussiana que necesita un tiempo de ejecución adicional ya que considera todas las observaciones para el cálculo. Reducir el intervalo de cálculo a (-3,3) para no tener en cuenta todas las observaciones en el cálculo no llevó consigo una disminución en la velocidad del cálculo ni un aumento en los valores de R^2, ya que el peso estadístico fuera del intervalo de cálculo (-3,3) es casi 0, por lo que dicha función se comporta prácticamente igual que la Gaussiana cuando su intervalo de cálculo no se encuentra limitado. Sin embargo, cuando el intervalo de cálculo se limitó a (-1,1), los valores de R^2 aumentaron notablemente y se acercaron a los valores obtenidos con las otras funciones de kernel reduciéndose además el tiempo de cálculo a la mitad. Por ello, en términos generales podemos concluir que limitar el intervalo de cálculo en la función Gaussiana a (-1,1) aumenta significativamente la flexibilidad de dicha función haciendo su cálculo computacionalmente más factible.

IV

El empleo del peso de Epanechnikov al aplicar las regresiones locales lineales y cuadráticas llevo consigo una implementación computacional más sencilla facilitando su uso en series temporales tan extensas como la nuestra. Sin embargo, cabe destacar que la regresión local cuadrática es computacionalmente más costosa que la regresión local lineal. Los resultados obtenidos en la contribución **III** pusieron de manifiesto que tanto el método lineal como el cuadrático fueron capaces de analizar satisfactoriamente la evolución de los patrones estacionales del CO_2 y el CH_4 sin resultar ninguno de ellos superior. Por lo tanto, las regresiones locales lineales podrían eventualmente reemplazar a las regresiones locales cuadráticas debido a su mayor simplicidad y al menor coste computacional.

V

Al analizar los tres grandes grupos de funciones matemáticas empleadas para analizar los patrones temporales del CO_2 y el CH_4 se encontraron algunas diferencias en términos de [1] suavidad, [2] tiempo de cálculo y coste computacional, [3] facilidad de uso y [4] precisión de los resultados. En primer lugar, la función armónica y el núcleo Gaussiano son las dos únicas funciones de las analizadas en la presente tesis que consideran el conjunto total de observaciones y no sólo un intervalo como hacen el resto. Este hecho lleva consigo que las curvas de tendencia obtenidas con ambas funciones sean más suaves que con el resto de las funciones que al basarse en cálculos locales son más sensibles a posibles huecos en la serie temporal. Además, el efecto de borde de las funciones de kernel y locales también provoca que los resultados gráficos obtenidos con dichas funciones sean menos suaves al principio y al final de la serie. En segundo lugar, la función armónica resultó ser el método de cálculo más rápido y el que requiere menos recursos computacionales. Las funciones de kernel requieren un mayor tiempo computacional, especialmente el núcleo Gaussiano cuando no está limitado o cuando lo está de (-3,3). En cualquier caso, las regresiones locales resultaron ser las funciones que requieren mayores recursos computacionales y mayores tiempos de cálculo, especialmente las regresiones locales cuadráticas. En tercer lugar, la función armónica resultó ser la más fácil de implementar, mientras que la regresión local cuadrática fue la más complicada debido al cálculo matricial implícito. Finalmente, aunque todas las funciones se ajustaron correctamente al conjunto de datos analizados, destacar la superioridad de las funciones armónicas, reflejando valores de R^2 más elevados que el resto de las funciones. En cuanto a las funciones de kernel y las regresiones locales, todas ellas reportaron valores de R^2 muy similares entre ellas, pero menores a las reportadas por la función armónica.

VI

El contrastre encontrado entre las concentraciones mínimas de los sectores rurales y las concentraciones máximas de los sectores urbanos tiene su explicación en los recorridos de las retrotrayectorias, así como el tiempo y la distancia recorrida por estas hasta impactar en la estación del CIBA. Si bien se observó un flujo de aire inicial procedente del Oeste tanto para los sectores rurales como para los urbanos, al impactar en la Península Ibérica las retrotrayectorias medias de ambos sectores se comportaron de manera muy diferente, mostrando un componente sur-suroeste para los sectores urbanos y un componente Norte para los sectores rurales. De igual modo, la retrotrayectoria media urbana invirtió más tiempo de transporte en la Península Ibérica, lo que se traduce en el arrastre de más contaminantes que la

retrotrayectoria media rural que tiene un carácter oceánico y marino y por tanto más limpia. Además, no se debe ignorar la recirculación de la retrotrayectoria media urbana en las 24 horas antes de impactar en el CIBA, ya que esto podría incrementar los niveles de los contaminantes arrastrados. Por tanto, se puede concluir que las concentraciones máximas de CO_2 y CH_4 encontradas en los sectores urbanos fueron el resultado del reforzamiento del penacho urbano de Valladolid y sus efectos en la estación del CIBA. Finalmente, el modelo METEX demostró ser una técnica rápida y sencilla que requiere escasos recursos computacionales para analizar la influencia del penacho urbano de Valladolid en los niveles finales de CO_2 y CH_4 medidos en la estación rural del CIBA.

A modo de colofón, la presente tesis ha demostrado la efectividad de aplicar regresiones armónicas, de kernel y locales ponderadas para describir la variabilidad temporal de CO_2 y CH_4 en una estación de fondo de la meseta norte castellana entre 2010 y 2016 alcanzando de esta forma el principal objetivo de la tesis. Pese a las diferencias encontradas entre las diferentes funciones matemáticas empleadas, estas no deben ser vistas como competidoras, de hecho, consideramos interesante emplear más de una función para asegurar que los resultados arrojados sean consistentes y reducir posibles sesgos. Además, la combinación de las observaciones de CO_2 y CH_4, los datos de velocidades del viento en superficie y en altura (a través del cálculo de retrotrayectorias) resultó ser una metodología útil para comprender los efectos del penacho urbano de la ciudad de Valladolid en los patrones temporales de CO_2 y CH_4. Los resultados obtenidos en la presente tesis sirven para comprender los procesos que gobiernan los ciclos de CO_2 y CH_4, lo cual es fundamental para implementar políticas eficaces de mitigación contra el cambio climático. A pesar de que este tipo de estudios dependen del lugar de estudio debido a las condiciones locales específicas de cada emplazamiento, son necesarios para comprender mejor la evolución de los patrones estacionales de las concentraciones de ambos gases en determinados emplazamientos, especialmente en las estaciones de fondo, como es la estación del CIBA. Debe destacarse la necesidad de llevar a cabo más estudios de este tipo, así como ampliar la red de estaciones de monitorización para analizar la evolución de estos gases a lo largo del tiempo. Por tanto, consideramos importante extender el uso de los métodos estadísticos empleados en la presente tesis para determinar los patrones temporales de estos gases a otras áreas de estudio y lograr una mayor comprensión de la evolución de estos gases en la troposfera. Finalmente, los resultados aquí presentados podrían verse enormemente mejorados si se ampliase la serie de datos disponible, por lo que mantener la estación del CIBA es vital para analizar la evolución del CO_2 y el CH_4 a lo largo del tiempo.

10. References*

Aalto, T., Hatakka, J., Paatero, I., Tuovinen, J.-P., Aurela, M., Laurila, T., Holmén, K., Trivett, N., Viisanen, Y. 2002. Tropospheric carbon dioxide concentrations at a northern boreal site in Finland: basic variations and source areas. *Tellus B Chemical and Physical Meteorology*, 54(2), 110–126. doi: 10.3402/tellusb.v54i2.16652

Adame, J.A., Hernández-Ceballos, M.A., Bolívar, J.P., De la Morena, B. 2012. Assessment of an air pollution event in the southwestern Iberian Peninsula. *Atmospheric Environment*, 55, 245–256. doi: 10.1016/j.atmosenv.2012.03.010

Adame, J.A., Valentí-Pía, M.D., Gil-Ojeda, M. 2015. Impact evaluation of potential volcanic plumes over Spain. *Atmospheric Research*, 160, 39–49. doi: 10.1016/j.atmosres.2015.03.002

Agrawal, S.K. 2019. Energy conservation and efficiency by energy efficient motor in India. *International Journal of Engineering and Advanced Technology*, 9(1), 3917–3926. doi: 10.35940/ijeat.A1321.109119

Ahlström, A., Raupach, M.R., Schurgers, G., Smit, B., Arneth, A., Jung, M., Reichstein, M., Canadell, J.G., Friedlingstein, P., Jain, A.K., Kato, E., Poulter, B., Sitch, S., Stocker, B.D., Viovy, N., Wang, Y.P., Wiltshire, A., Zaehle, S., Zeng, N. 2015. The dominant role of semi-arid ecosystems in the trend and variability of the land CO_2 sink. *Science*, 348 (6237), 895–899. doi: 10.1126/science.aaa1668

AIP. 2020. The Discovery of Global Warming. https://history.aip.org/climate/co2.htm#N_11a_. Accessed 23 October 2020.

Al-Anzi, B., Abusam, A., Khan, A.R. 2016. Evaluation of temporal variations in ambient air quality at Jahra using multivariate techniques. *Environmental Technology & Innovation*, 5, 225–232. doi: 10.1016/j.eti.2016.04.003

Allwine, K.J., Whiteman, C.D. 1994. Single-station integral measures of atmospheric stagnation, recirculation and ventilation. *Atmospheric Environment*, 28, 713–721. doi: 10.1016/1352-2310(94)90048-5

Almeida, C.T., Oliveira-Júnior, J.F., Delgado, R.C., Cubo, P., Ramos, M.C. 2017. Spatiotemporal rainfall and temperature trends throughout the Brazilian Legal Amazon, 1973–2013. *International Journal of Climatology*, 37(4), 2013–2026. doi: 10.1002/joc.4831

Alonso-Blanco, E., Castro, A., Calvo, A.I., Pont, V., Mallet, M., Fraile, R. 2018. Wildfire smoke plumes transport under a subsidence inversion: Climate and health implications in a distant urban area. *Science of the Total Environment*, 619–620, 988–1002. doi: 10.1016/j.scitotenv.2017.11.142

Anderson, T.R., Hawkins, E., Jones, P.D. 2016. CO_2, the greenhouse effect and global warming: from the pioneering work of Arrhenius and Callendar to today's Earth System Models. *Endeavour*, 40(3), 178–187. doi: 10.1016/j.endeavour.2016.07.002

Angert, A., Biraud, S., Bonfils, C., Henning, C.C., Buermann, W., Pinzon, J., Tucker, C.J., Fung, I. 2005. Drier summers cancel out the CO_2 uptake enhancement induced by warmer springs. *Proceedings of the National Academy of Sciences of the United States of America,* 102(31), 10823–10827. doi:10.1073/pnas.0501647102

Arioli, M.S., D'Agosto, M.D.A., Amaral, F.G., Cybis, H.B.B. 2020. The evolution of city-scale GHG emissions inventory methods: A systematic review. *Environmental Impact Assessment Review,* 80, 106316. doi:10.1016/j.eiar.2019.106316

Artuso, F., Chamard, P., Piacentino, S., Sferlazzo, D.M., De Silvestri, L., di Sarra, A., Meloni, D., Monteleone, F. 2009. Influence of transport and trends in atmospheric CO_2 at Lampedusa. *Atmospheric Environment*, 43, 3044–3051. doi: 10.1016/j.atmosenv.2009.03.027

Bakwin, P.S., Tans, P.P., Hurst, D.F., Zhao, C. 1998. Measurements of carbon dioxide on very tall towers: results of the NOAA/CMDL program. *Tellus, Series B: Chemical and Physical Meteorology,* 50(5), 401–415. doi: 10.3402/tellusb.v50i5.16216

Baldasano, J.M., Soret, A., Guevara, M., Martínez, F., Gassó, S. 2014. Integrated assessment of air pollution using observations and modelling in Santa Cruz de Tenerife (Canary Islands). *Science of the Total Environment*, 473–474, 576–588. doi: 10.1016/j.scitotenv.2013.12.062

Balsalobre, D., Álvarez, A., Cantos, J. M. 2015. Public budgets for energy RD&D and the effects on energy intensity and pollution levels. *Environmental Science and Pollution Research,* 22(7), 4881–4892. doi:10.1007/s11356-014-3121-3

Bamberger, I., Oney, B., Brunner, D., Henne, S., Leuenberger, M., Buchmann, N., Eugster, W. 2017. Observations of atmospheric methane and carbon dioxide mixing ratios: tall-tower or mountain-top stations? *Boundary-Layer Meteorology*, 164(1), 135–159. doi: 10.1007/s10546-017-0236-3

Barichivich, J., Briffa, K.R., Myneni, R.B., Osborn, T.J., Melvin, T.M., Ciais, P., Piao, S., Tucker, C. 2013. Large-scale variations in the vegetation growing season and annual cycle of atmospheric CO_2 at high northern latitudes from 1950 to 2011. *Global Change Biology*, 19(10), 3167–3183. doi:10.1111/gcb.12283

Barlow, J.M., Palmer, P.I., Bruhwiler, L.M., Tans, P. 2015. Analysis of CO_2 mole fraction data: first evidence of large-scale changes in CO_2 uptake at high northern latitudes. *Atmospheric Chemistry and Physics*, 15, 13739–13758. doi: 10.5194/acp-15-13739-2015

Beck, J., Bock, M., Schmitt, J., Seth, B., Blunier, T., Fischer, H. 2018. Bipolar carbon and hydrogen isotope constraints on the Holocene methane budget. *Biogeosciences*, 15(23), 7155–7175. doi: 10.5194/bg-15-7155-2018

Bennouna, Y.S., Cachorro, V.E., Mateos, D., Burgos, M.A., Toledano, C., Torres, B., de Frutos, A.M. 2016. Long-term comparative study of columnar and surface mass concentration aerosol properties in a background environment. *Atmospheric Environment*, 140, 261–272. doi: 10.1016/j.atmosenv.2016.05.061

Bergamaschi, P., Krol, M., Meirink, J.F., Dentener, F., Segers, A., Van Aardenne, J., Monni, S., Vermeulen, A.T., Schmidt, M., Ramonet, M., Yver, C., Meinhardt, F., Nisbet, E.G., Fisher, R.E., O'Doherty, S., Dlugokencky, E.J. 2010. Inverse modeling of European CH_4 emissions 2001–2006. *Journal of Geophysical Research*, 115, D22309. doi: 10.1029/2010JD014180

Bergamaschi, P., Houweling, S., Segers, A., Krol, M., Frankenberg, C., Scheepmaker, R.A., Dlugokencky, E., Wofsy, S.C., Kort, E.A., Sweeney, C., Schuck, T., Brenninkmeijer, C., Chen, H., Beck, V., Gerbig, C. 2013. Atmospheric CH_4 in the first decade of the 21st century: inverse modeling analysis using SCIAMACHY satellite retrievals and NOAA surface measurements.

Journal of Geophysical Research: Atmospheres, 118 (13), 7350–7369. doi:10.1002/jgrd.50480

Berhanu, T.A., Szidat, S., Brunner, D., Satar, E., Schanda, R., Nyfeler, P., Battaglia, M., Steinbacher, M., Hammer, S., Leuenberger, M. 2017.Estimation of the fossil fuel component in atmospheric CO_2 based on radiocarbon measurements at the Beromünster tall tower, Switzerland. *Atmospheric Chemistry and Physics*, 17(17), 10753–10766. doi: 10.5194/acp-17-10753-2017

Bianchi, S., Plastino, W., Brattich, E., Djurdjevic, V., Longo, A., Hernández-Ceballos, M.A., Sarvan, D., Ajtić, J. 2019. Analysis of trends, periodicities, and correlations in the beryllium-7 time series in Northern Europe. *Applied Radiation and Isotopes*, 148, 160–167. doi: 10.1016/j.apradiso.2019.03.038

Boffino, L., Conejo, A.J, Sioshansi, R., Oggioni, G. 2019. A two-stage stochastic optimization planning framework to decarbonize deeply electric power systems. *Energy Economics*, 84. 104457. doi: 10.1016/j.eneco.2019.07.017

Borge, R., Lumbreras, J., Vardoulakis, S., Kassomenos, P., Rodríguez, E. 2007. Analysis of long-range transport influences on urban PM_{10} using two-stage atmospheric trajectory clusters. *Atmospheric Environment*, 41, 4434–4450. doi: 10.1016/j.atmosenv.2007.01.053

Brancher, M., Griffiths, K.D., Franco, D., de Melo Lisboa, H. 2017. A review of odour impact criteria in selected countries around the world. *Chemosphere*, 168, 1531–1570. doi: 10.1016/j.chemosphere.2016.11.160

Bravo, M., Mira, T., Soler, M.R., Cuxart, J. 2008. Intercomparison and evaluation of MM5 and Meso-NH mesoscale models in the stable boundary layer. *Boundary-Layer Meteorology*, 128(1), 77–101. doi: 10.1007/s10546-008-9269-y

Breaker, L.C., Loor, H.R., Carroll, D. 2016. Trends in sea surface temperature off the coast of Ecuador and the major processes that contribute to them. *Journal of Marine Systems*, 164, 151–164. doi: 10.1016/j.jmarsys.2016.09.002

Buchholz, R.R., Paton-Walsh, C., Griffith, D.W.T., Kubistin, D., Caldow, C., Fisher, J.A., Deutscher, N.M., Kettlewell, G., Riggenbach, M., Macatangay, R., Krummel, P.B.,

Langenfelds, R.L. 2016. Source and meteorological influences on air quality (CO, CH_4 and CO_2) at a Southern Hemisphere urban site. *Atmospheric Environment*, 126, 274–289. doi: 10.1016/j.atmosenv.2015.11.041

Buermann, W., Lintner, B.R., Koven, C.D., Angert, A., Pinzon, J.E., Tucker, C.J., Fung, I.Y. 2007. The changing carbon cycle at Mauna Loa Observatory. *Proceedings of the National Academy of Sciences*, 104(11), 4249–4254. doi: 10.1073/pnas.0611224104

Buragienė, S., Šarauskis, E., Romaneckas, K., Sasnauskienė, J., Masilionytė, L., Kriaučiūnienė, Z. 2015. Experimental analysis of CO_2 emissions from agricultural soils subjected to five different tillage systems in Lithuania. *Science of the Total Environment*, 514, 1–9. doi:10.1016/j.scitotenv.2015.01.090

Burgos, M.A., Mateos, D., Cachorro, V.E., Toledano, C., de Frutos, A.M. 2016a. Aerosol properties of mineral dust and its mixtures in a regional background of north-central Iberian Peninsula. *Science of the Total Environment,* 572, 1005–1019. doi: 10.1016/j.scitotenv.2016.08.001

Burgos, M.Á. 2016b. Estudio de las propiedades en columna y superficie del aerosol atmosférico en la zona centro-norte de la Península Ibérica: énfasis en aerosol desértico. *Universidad de Valladolid*. doi: 10.35376/10324/23046.

Burrows, M.T., Schoeman, D.S., Buckley, L.B., Moore, P., Poloczanska, E.S., Brander, K.M., Brown, C., Bruno, J.F., Duarte, C.M., Halpern, B.S., Holding, J., Kappel, C.V., Kiessling, W., O´Connor, M.I., Pandolfi, J.M., Parmesan, C., Schwing, F.B., Sydeman, W.J., Richardson, A. J. 2011. The pace of shifting climate in marine and terrestrial ecosystems. *Science,* 334(6056), 652–655. doi:10.1126/science.1210288

Calvo, A.I., Pont, V., Olmo, F.J., Castro, A., Alados-Arboledas, L., Vicente, A.M.,Fernández-Raga, M., Fraile, R. 2012. Air masses and weather types: A useful tool for characterizing precipitation chemistry and wet deposition. *Aerosol and Air Quality Research*, 12(5), 856–878. doi: 10.4209/aaqr.2012.03.0068

Carlos, H.A., Shi, X., Sargent, J., Tanski, S., Berke, E.M. 2010. Density estimation and adaptive bandwidths: A primer for public health practitioners. *International Journal of Health Geographics*, 9(3), 1–8. doi:10.1186/1476-072X-9-39

Casas, G. 2010. Estimaciones via Kernel. https://es.scribd.com/doc/57531637/Estimaciones-via-Kernel. Accessed 2 November 20.

Celik, A.N. 2004. On the distributional parameters used in assessment of the suitability of wind speed probability density functions. *Energy Conversion and Management*, 45(11-12), 1735–1747. doi: 10.1016/j.enconman.2003.09.027

CGER METEX. 2020. http://db.cger.nies.go.jp/metex/index.html. Accessed 23 October 2020.

Chamard, B.P., Thiery, F., Di Sarra, A., Ciattaglia, L., De Silvestri, L., Grigioni, P., Monteleone, F., Piacentino, S. 2003. Interannual variability of atmospheric CO_2 in the Mediterranean: measurements at the island of Lampedusa. *Tellus: Series B*, 55, 83–93. doi: 10.1034/j.1600-0889.2003.00048.x

Chatfield, C. 1995. Problem solving: a statistician´s guide, 2nd edn. *Texts in Statistical Science*. Chapman & Hall, Boca Ratón Florida, 325 pp.

Chen, X., Shuai, C., Wu, Y., Zhang, Y. 2020. Analysis on the carbon emission peaks of China's industrial, building, transport, and agricultural sectors. *Science of the Total Environment*, 709. 135768. doi: 10.1016/j.scitotenv.2019.135768

Cheng, L., Ji, D., He, J., Li, L., Du, L., Cui, Y., Zhang, H., Zhou, L., Li, Z., Zhou, Y., Miao, S., Zhengyu, G., Wang, Y. 2019. Characteristics of air pollutants and greenhouse gases at a regional background station in Southwestern China. *Aerosol and Air Quality Research*, 19(5), 1007–1023. doi: 10.4209/aaqr.2018.11.0397

Cheng, S., An, X., Zhou, L., Tans, P.P., Jacobson, A. 2017. Atmospheric CO_2 at Waliguan station in China: Transport climatology, temporal patterns and source-sink region representativeness. *Atmospheric Environment*, 159, 107–116. doi: 10.1016/j.atmosenv.2017.03.055

Cheng, S., Zhou, L., Tans, P.P., An, X., Liu, Y. 2018. Comparison of atmospheric CO_2 mole fractions and source–sink characteristics at four WMO/GAW stations in China. *Atmospheric Environment*, 180, 216–225. doi: 10.1016/j.atmosenv.2018.03.010

Chham, E., Milena-Pérez, A., Piñero-García, F., Hernández-Ceballos, M.A., Orza, J.A.G., Brattich, E., El Bardouni, T., Ferro-García, M.A. 2019. Sources of the seasonal-trend behaviour and periodicity modulation of ^{7}Be air concentration in the atmospheric surface layer observed in southeastern Spain. *Atmospheric Environment*, 213, 148–158. doi: 10.1016/j.atmosenv.2019.06.011

Ciais, P., Peylin, P., Bousquet, P. 2000. Regional biospheric carbon fluxes as inferred from atmospheric CO_2 measurements. *Ecological Applications, 10*(6), 1574–1589. doi:10.2307/2641225

Ciais, P., Reichstein, M., Viovy, N., Granier, A., Ogee, J., Allard, V., Aubinet, M., Buchmann, N., Bernohofer, C., Carrara, A., Chevallier, F., De Noblet, N., Friend, A.D., Friedlingstein, P., Grunwald, T., Henesch, b., Keronen, P., Knohl, A.,Krinnen, G., Loustau, D., Manca, G., Matteucci, G., Miglietta, F., Ourcival, J.M., Papale, D., Pilegaard, K., Rambal, S., Seufert, G., Soussana, J.F., Sanz, M.J., Schulze, E.D., Vesala, T., Valentini, R. 2005. Europe-wide reduction in primary productivity caused by the heat and drought in 2003. *Nature*, 437. doi:10.1038/nature03972

Cleveland, W.S. 1979. Robust locally weighted regression and smoothing scatterplots. *Journal of the American Statistical Association*, 74(368), 829–836.

Cleveland, R.B., Cleveland, W.S., McRae, J.E., Terpenning, I. 1990. STL: a seasonal-trend decomposition procedure based on loess. *Journal of Official Statistics*, 6(1), 3–73.

Conangla, L., Cuxart, J. 2006. On the turbulence in the upper part of the low-level jet: an experimental and numerical study. *Boundary-Layer Meteorology*, 118(2), 379–400. doi: 10.1007/s10546-005-0608-y

Corti, J. 2017. Contribuciones de la Unión Europea a los desafíos que representa la protección del medio ambiente: La diplomacia europea en materia de lucha contra el cambio climático. *Cuadernos Europeos de Deusto* (57), 167–192. University of Deusto. doi: 10.18543/ced-57-2017pp167-192

Crosson, E.R. 2008. A cavity ring-down analyzer for measuring atmospheric levels of methane, carbon dioxide, and water vapor. *Applied Physics B: Lasers and Optics*, 92, 403–408. doi: 10.1007/s00340-008-3135-y

Cui, J., Pandey Deolal, S., Sprenger, M., Henne, S., Staehelin, J., Steinbacher, M., Nédélec, P. 2011. Free tropospheric ozone changes over Europe as observed at Jungfraujoch (1990-2008): An analysis based on backward trajectories. *Journal of Geophysical Research Atmospheres*, 116(10). D10304. doi: 10.1029/2010JD015154

Cundari, V., Colombo, T., Ciattaglia, L. 1995. Thirteen years of atmospheric carbon dioxide measurements at Mt. Cimone station, Italy. *Il Nuovo Cimento C*, 18, 33–47. doi: 10.1007/BF02561457

Curcoll, R., Camarero, L., Bacardit, M., Àgueda, A., Grossi, C., Gacia, E., Font, A., Morguí, J-A. 2019. Atmospheric Carbon Dioxide variability at Aigüestortes, Central Pyrenees, Spain. *Regional Environmental Change*, 19(2), 313–324. doi: 10.1007/s10113-018-1443-2

Cuxart, J., Yagüe, C., Morales, G., Terradellas, E., Orbe, J., Calvo, J., Fernández, A., Soler, M.R., Infante, C., Buenestado, P., Espinalt, A., Joergensen, H.E., Rees, J.M., Vilà, J., Redondo, J.M., Cantalapiedra, I.R., Conangla, L. 2000. Stable atmospheric boundary-layer experiment in Spain (SABLES 98): a report. *Boundary-Layer Meteorology*, 96, 337–370.

Cuxart, J. 2008. Nocturnal basin low-level jets: an integrated study. *Acta Geophysica*, 56(1), 100–113. doi: 10.2478/s11600-007-0042-2

Da, J., Zhang, Y.G., Li, G., Meng, X., Ji, J. 2019. Low CO_2 levels of the entire Pleistocene epoch. *Nature Communications*, 10(1), 4342. doi: 10.1038/s41467-019-12357-5

Dalsøren, S.B., Myhre, C.L., Myhre, G., Gomez-Pelaez, A.J., Søvde, O.A., Isaksen, I.S.A., Weiss, R.F., Harth, C.M. 2016. Atmospheric methane evolution the last 40 years. *Atmospheric Chemistry and Physics*, 16(5), 3099–3126. doi:10.5194/acp-16-3099-2016

de Haan, P. 1999. On the use of density kernels for concentration estimations within particle and puff dispersion models. *Atmospheric Environment*, 33, 2007–2021. doi: 10.1016/S1352-2310(98)00424-5

De Smith, M.J., Goodchild, M.F. Longley, P. 2007. Geospatial analysis: a comprehensive guide to principles, techniques and software tools, 2nd edn. Leicester: Matador, 491 pp.

DeCarlo, L.T. 1997. On the meaning and use of kurtosis. Psychological Methods, 2(3), 292–307. doi: 10.1037/1082-989X.2.3.292

Dekhtyareva, A., Edvardsen, K., Holmén, K., Hermansen, O., Hansson, H.-C. 2016. Influence of local and regional air pollution on atmospheric measurements in Ny-Ålesund. *International Journal of Sustainable Development and Planning*, 11(4), 578–587. doi: 10.2495/SDP-V11-N4-578-587

del Río, S., Penas, Á., Fraile, R. 2005. Analysis of recent climatic variations in Castile and Leon (Spain). *Atmospheric Research*, 73(1-2), 69–85. doi: 10.1016/j.atmosres.2004.06.005

del Río, S., Fraile, R., Herrero, L., Penas, A. 2007. Analysis of recent trends in mean maximum and minimum temperatures in a region of the NW of Spain (Castilla y León). *Theoretical and Applied Climatology*, 90(1-2), 1–12. doi: 10.1007/s00704-006-0278-9

Devroye, L.P. Györfi, L. 1985. Nonparametric Density Estimation: The L1 View. Wiley, New York, 367 pp.

Di Gilio, A., de Gennaro, G., Dambruoso, P., Ventrella, G. 2015. An integrated approach using high time-resolved tools to study the origin of aerosols. *Science of the Total Environment*, 530–531, 28–37. doi: 10.1016/j.scitotenv.2015.04.073

Dimitriou, K. 2015. The dependence of PM size distribution from meteorology and local regional contributions, in Valencia (Spain) – a CWT model approach. *Aerosol and Air Quality Research*, 15, 1979–1989. doi: 10.4209/aaqr.2015.03.0162

Dimitriou, K., Kassomenos, P. 2017a. Aerosol contributions at an urban background site in Eastern Mediterranean – Potential source regions of PAHs in PM_{10} mass. *Science of the Total Environment*, 598, 563–571. doi: 10.1016/j.scitotenv.2017.04.164

Dimitriou, K., Paschalidou, A.K., Kassomenos, P.A. 2017b. Distinct synoptic patterns and air masses responsible for long-range desert dust transport and sea spray in Palermo, Italy. *Theoretical and Applied Climatology*, 130(3-4), 1123–1132. doi: 10.1007/s00704-016-1957-9

Dimitriou, K., Kassomenos, P. 2018. Quantifying daily contributions of source regions to PM concentrations in Marseille based on the trails of incoming air masses. *Air Quality, Atmosphere & Health*, 11, 571–580. doi: 10.1007/s11869-018-0564-6

Dlugokencky, E.J., Steele, L.P., Lang, P.M., Masarie, A. 1994. The growth rate and distribution of atmospheric methane. Journal of Geophysical Research, 99, 17021–17043. doi: 10.1029/94JD01245

Domínguez-López, D., Adame, J.A., Hernández-Ceballos, M.A., Vaca, F., De la Morena, B.A., Bolívar, J.P. 2014. Spatial and temporal variation of surface ozone, NO and NO_2 at urban, suburban, rural and industrial sites in the southwest of the Iberian Peninsula. *Environmental Monitoring and Assessment*, 186(9), 5337–5351. doi: 10.1007/s10661-014-3783-9

Domínguez-López, D., Vaca, F., Hernández-Ceballos, M.A., Bolívar, J.P. 2015. Identification and characterisation of regional ozone episodes in the southwest of the Iberian Peninsula. *Atmospheric Environment*, 103, 276–288. doi: 10.1016/j.atmosenv.2014.12.050

Donnelly, A., Naughton, O., Broderick, B., Misstear, B. 2017. Short-term forecasting of nitrogen dioxide (NO_2) levels using a hybrid statistical and air mass history modelling approach. *Environmental Modeling & Assessment*, 22(3), 231–241. doi: 10.1007/s10666-016-9532-4

Đozić, D.J., Gvozdenac Urošević, B.D. 2019. Application of artificial neural networks for testing long-term energy policy targets. *Energy*, 174, 488–496. doi: 10.1016/j.energy.2019.02.191

EDGAR. 2020. Emissions Database for Global Atmospheric Research. https://edgar.jrc.ec.europa.eu/overview.php?v=booklet2019&dst=GHGemi. Accessed 11 August 2020.

Energy Roadmap 2050. 2012. https://ec.europa.eu/energy/sites/ener/files/documents/2012_energy_roadmap_2050_en_0.pdf. Accessed 17 July 2020.

Eneroth, K., Aalto, T., Hatakka, J., Holmen, K., Laurila, T., Viisanen, Y. 2005. Atmospheric transport of carbon dioxide to a baseline monitoring station in northern Finland. *Tellus, Series B: Chemical and Physical Meteorology,* 57, 366–374. doi: 10.1111/j.1600-0889.2005.00160.x

Espinosa, F., Rivera-Ingraham, G. A., Ostalé-Valriberas, E., García-Gómez, J. C. 2018. Predicting the fate of the most endangered marine invertebrate of the mediterranean: The power of long-term monitoring in conservation biology. *Aquatic Conservation: Marine and Freshwater Ecosystems, 28*(6), 1283–1293. doi:10.1002/aqc.2944

European Commision. 2020. Internal Market, Industry, Entrepreneurship and SMEs. https://ec.europa.eu/growth/tools-databases/regional-innovation-monitor/base-profile/castilla-y-leon. Accessed 5 August 2020.

Everitt, B.S., Skrondal, A. 2010. The Cambridge Dictionary of Statistics, 4th edn. United Kingdom, Cambridge, 480 pp.

Fan, J., Yao, Q. 2003. Nonlinear time series. Nonparametric and parametric methods. *Springer Series in Statistics*. New York, 576 pp.

Fang, B., Lei, H., Zhang, Y., Quan, Q., Yang, D. 2020. Spatio-temporal patterns of evapotranspiration based on upscaling eddy covariance measurements in the dryland of the North China Plain. *Agricultural and Forest Meteorology*, 281, 107844. doi: 10.1016/j.agrformet.2019.107844

Fang, S-X., Zhou, L-X., Masarie, K.A., Xu, L., Rella, C.W. 2013. Study of atmospheric CH_4 mole fractions at three WMO/GAW stations in China. *Journal of Geophysical Research Atmospheres*, 118(10), 4874–4886. doi: 10.1002/jgrd.50284

Fang, S.X., Zhou, L.-X., Tans, P.P., Ciais, P., Steinbacher, M., Xu, L., Luan, T. 2014. In situ measurement of atmospheric CO_2 at the four WMO/GAW stations in China. *Atmospheric Chemistry and Physics*, 14, 2541–2554. doi: 10.5194/acp-14-2541-2014

Fang, S.X., Tans, P.P., Steinbacher, M., Zhou, L.X., Luan, T. 2015. Comparison of the regional CO_2 mole fraction filtering approaches at a WMO/GAW regional station in China. *Atmospheric Measurement Techniques*, 8, 5301–5313. doi: 10.5194/amt-8-5301-2015

Fang, S.X., Tans, P.P., Dong, F., Zhou, H., Luan, T. 2016. Characteristics of atmospheric CO_2 and CH_4 at the Shangdianzi regional background station in China. *Atmospheric Environment*, 131, 1–8. doi: 10.1016/j.atmosenv.2016.01.044

Feng, D., Gao, X., Yang, L., Hui, X., Zhou, Y. 2019. Analysis of long-term (2003–2015) spatial-temporal distribution of atmospheric methane in the troposphere over the Qinghai-Xizang plateau based on AIRS data. *Theoretical and Applied Climatology,* 137(1-2), 1247–1255. doi:10.1007/s00704-018-2651-x

Fernández-Camacho, R., de la Rosa, J.D., Sánchez de la Campa, A.M. 2016. Trends and sources vs air mass origins in a major city in South-western Europe: Implications for air quality management. *Science of the Total Environment*, 553, 305–315. doi: 10.1016/j.scitotenv.2016.02.079

Fernandez-Cortes, A., Calaforra, J.M., Sanchez-Martos, F. 2006. Spatiotemporal analysis of air conditions as a tool for the environmental management of a show cave (Cueva del Agua, Spain). *Atmospheric Environment*, 40(38), 7378–7394. doi: 10.1016/j.atmosenv.2006.06.045

Fernández-Guisuraga, J.M., Castro, A., Alves, C., Calvo, A., Alonso-Blanco, E., Blanco-Alegre, C., Rocha, A., Fraile, R. 2016. Nitrogen oxides and ozone in Portugal: trends and ozone estimation in an urban and a rural site. *Environmental Science and Pollution Research*, 23(17), 17171–17182. doi: 10.1007/s11356-016-6888-6

Fernández-Raga, M., Tomás, C., Fraile, R. 2010. Human mortality seasonality in Castile-León, Spain, between 1980 and 1998: the influence of temperature, pressure and humidity. *International Journal of Biometeorology*, 54(4), 379–392. doi: 10.1007/s00484-009-0289-1

Fiedler, V., Arnold, F., Schlager, H., Dörnbrack, A., Pirjola, L., Stohl, A. 2009. East Asian SO_2 pollution plume over Europe – Part 2: Evolution and potential impact. *Atmospheric Chemistry and Physics*, 9(14), 4729–4745. doi: 10.5194/acp-9-4729-2009

Fiore, A.M., Naik, V., Leibensperger, E. 2015. Air quality and climate connections. Journal of the *Air and Waste Management Association*, 65(6), 645–685. doi: 10.1080/10962247.2015.1040526

Fleming, J.R. 2000. T.C. Chamberlin, Climate Change, and Cosmogony. Studies in History and Philosophy of Modern Physics, 31(3), 293–308. doi: 10.1016/S1355-2198(00)00015-0

Forkel, M., Carvalhais, N., Rödenbeck, C., Keeling, R., Heimann, M., Thonicke, K., Zaehle, S., Reichstein, M. 2016. Enhanced seasonal CO_2 exchange caused by amplified plant productivity in northern ecosystems. *Science,* 351(6274), 696–699. doi:10.1126/science.aac4971

Fraile, R., Calvo, A.I., Castro, A., Fernández-González, D., García-Ortega, E. 2006. The behavior of the atmosphere in long-range transport. *Aerobiologia*, 22, 35–45. doi: 10.1007/s10453-005-9014-7

Friedlingstein, P., Jones, M.W., O'Sullivan, M., Andrew, R.M., Hauck, J., Peters, G.P., Peters, W., Pongratz, J., Sitch, S., Le Quéré, C., Bakker, D.C.E., Canadell, J.G., Ciais, P., Jackson, R.B., Anthoni, P., Barbero, L., Bastos, A., Bastrikov, V., Becker, M., Bopp, L., Buitenhuis, E., Chandra, N., Chevallier, F., Chini, L.P., Currie, K.I., Feely, R.A., Gehlen, M., Gilfillan, D., Gkritzalis, T., Goll, D.S., Gruber, N., Gutekunst, S., Harris, I., Haverd, V., Houghton, R.A., Hurtt, G., Ilyina, T., Jain, A.K., Joetzjer, E., Kaplan, J.O., Kato, E., Klein Goldewijk, K.K., Korsbakken, J.I., Landschützer, P., Lauvset, S.K., Lefèvre, N., Lenton, A., Lienert, S., Lombardozzi, D., Marland, G., McGuire, P.C., Melton, J.R., Metzl, N., Munro, D.R., Nabel, J.E.M.S., Nakaoka, S.-I., Neill, C., Omar, A.M., Ono, T., Peregon, A., Pierrot, D., Poulter, B., Rehder, G., Resplandy, L., Robertson, E., Rödenbeck, C., Séférian, R., Schwinger, J., Smith, N., Tans, P.P., Tian, H., Tilbrook, B., Tubiello, F.N., van der Werf, G.R., Wiltshire, A.J., Zaehle, S. 2019. Global Carbon Budget 2019. *Earth System Science Data*, 11(4), 1783–1838. doi: 10.5194/essd-11-1783-2019

Friedrich, T., Timmermann, A. 2020. Using Late Pleistocene sea surface temperature reconstructions to constrain future greenhouse warming. *Earth and Planetary Science Letters*, 530, 115911. doi: 10.1016/j.epsl.2019.115911

Ganesan, A.L., Schwietzke, S., Poulter, B., Arnold, T., Lan, X., Rigby, M., Vogel, F.R., van der Werf, G.R., Janssens-Maenhout, G., Boesch, H., Pandey, S., Manning, A.J., Jackson, R.B., Nisbet, E.G., Manning, M.R. 2019. Advancing Scientific Understanding of the Global Methane Budget in Support of the Paris Agreement. *Global Biogeochemical Cycles*, 33(12), 1475–1512. doi: 10.1029/2018GB006065

García, M.Á., Sánchez, M.L., Pérez, I.A., De Torre, B. 2008. Continuous carbon dioxide measurements in a rural area in the upper Spanish plateau. *Journal of the Air & Waste Management Association*, 58(7), 940–946. doi: 10.3155/1047-3289.58.7.940

García, M.Á., Sánchez, M.L, Pérez, I.A. 2012. Differences between carbon dioxide levels over suburban and rural sites in Northern Spain. *Environmental Science and Pollution Research*, 19(2), 432–439. doi: 10.1007/s11356-011-0575-4

García, M.Á., Sánchez, M.L., Pérez, I.A., Ozores, M.I., Pardo, N. 2016. Influence of atmospheric stability and transport on CH_4 concentrations in northern Spain. *Science of the Total Environment*, 550, 157–166. doi: 10.1016/j.scitotenv.2016.01.099

García-Mozo, H., Hernández-Ceballos, M.A., Trigo, M.M., Galán, C. 2017. Wind dynamics' influence on south Spain airborne olive-pollen during African intrusions. *Science of the Total Environment*, 609, 1340–1348. doi: 10.1016/j.scitotenv.2017.08.005

García-Portugués, E., Barros, A.M.G., Crujeiras, R.M., González-Manteiga, W., Pereira, J. 2014. A test for directional-linear independence, with applications to wildfire orientation and size. *Stochastic Environmental Research and Risk Assessment*, 28, 1261–1275. doi: 10.1007/s00477-013-0819-6

Ghasemifard, H., Vogel, F.R., Yuan, Y., Luepke, M., Chen, J., Ries, L., Leuchner, M., Schunk, C., Vardag, S.N., Menzel, A. 2019. Pollution events at the high-altitude mountain site Zugspitze Schneefernerhaus (2670 m a.s.l.), Germany. *Atmosphere*, 10(330), 2–17. doi:10. 3390/atmos10060330

Ginzburg, A.S., Vinogradova, A.A., Fedorova, E.I. 2011. Some features of seasonal variations in the methane content in the atmosphere over northern Eurasia. *Izvestiya, Atmospheric and Oceanic Physics*, 47 (1), 45–58. doi: 10.1134/S0001433811010087

Gramacki, A. 2018. Nonparametric Kernel density estimation and its computational aspects. *Studies in Big Data*, 37. Springer, Switzerland, 197 pp.

Grange, S.K., Lewis, A.C., Carslaw, D.C. 2016. Source apportionment advances using polar plots of bivariate correlation and regression statistics. *Atmospheric Environment*, 145, 128–134. doi: 10.1016/j. atmosenv.2016.09.016

Graven, H.D., Guilderson, T.P., Keeling, R.F. 2012. Observations of radiocarbon in CO_2 at La Jolla, California, USA 1992–2007: analysis of the long-term trend. *Journal of Geophysical Research: Atmospheres*, 117, D02302. doi: 10.1029/2011JD016533

Graven, H.D., Keeling, R.F., Piper, S.C., Patra, P.K., Stephens, B.B., Wofsy, S.C., Welp, L.R., Sweeney, C.S., Tans, P.P., Kelley, J.J., Daube, B.C., Kort, E.A., Santoni, G.W., Bent, J.D. 2013. Enhanced seasonal exchange of CO_2 by northern ecosystems since 1960. *Science*, 341(6150), 1085–1089. doi:10.1126/science.1239207

Griffiths, S., Sovacool, B.K. 2020. Rethinking the future low-carbon city: Carbon neutrality, green design, and sustainability tensions in the making of Masdar City. *Energy Research and Social Science*, 62, 101368. doi: 10.1016/j.erss.2019.101368

Guha, A., Gentner, D.R., Weber, R.J., Provencal, R., Goldstein, A.H. 2015. Source apportionment of methane and nitrous oxide in California's San Joaquin Valley at CalNex 2010 via positive matrix factorization. *Atmospheric Chemistry and Physics*, 15(20), 12043–12063. doi: 10.5194/acp-15-12043-2015

Guo, J-X., Huang, C. 2020. Feasible roadmap for CCS retrofit of coal-based power plants to reduce Chinese carbon emissions by 2050. *Applied Energy*, 259, 114112. doi: 10.1016/j.apenergy.2019.114112

Gutiérrez, R., Gutiérrez-Sánchez, R., Nafidi, A. 2008. Trend analysis using nonhomogeneous stochastic diffusion processes. Emission of CO_2; Kyoto protocol in Spain. *Stochastic Environmental Research and Risk Assessment*, 22, 57–66. doi: 10.1007/s00477-006-0097-7

Halofsky, J.E., Peterson, D.L., Harvey, B.J. 2020. Changing wildfire, changing forests: the effects of climate change on fire regimes and vegetation in the Pacific Northwest, USA. *Fire Ecology*, 16(4). doi: 10.1186/s42408-019-0062-8

Härdle, W. 1991. Smoothing techniques with implementation in S. *Springer Series in Statistics*. Springer, New York.

Hartmann, D.L. 1994. Global physical climatology. *International Geophysics Series*, 56. Academic Press, San Diego, 411 pp.

Hase, F., Frey, M., Blumenstock, T., Groß, J., Kiel, M., Kohlhepp, R., Mengistu Tsidu, G., Schäfer, K., Sha, M.K., Orphal, J. 2015. Application of portable FTIR spectrometers for detecting greenhouse gas emissions of the major city Berlin. *Atmospheric Measurement Techniques*, 8, 3059–3068. doi: 10.5194/amt-8-3059-2015

Haszpra, L., Barcza, Z., Hidy, D., Szilágyi, I., Dlugokencky, E., Tans, P. 2008. Trends and temporal variations of major greenhouse gases at a rural site in central Europe. *Atmospheric Environment*, 42, 8707–8716. doi.org/10.1007/978-90-481-9950-1_3

Hatakka, J., Aalto, T., Aaltonen, V., Aurela, M., Hakola, H., Komppula, M., Laurila, T., Lihavainen, H., Paatero, J., Salminen, K., Viisanen, Y. 2003. Overview of the atmospheric research activities and results at Pallas GAW station. *Boreal Environment Research*, 8, 365–383.

Hawkins, E., Jones, P.D. 2013. On increasing global temperatures: 75 years after Callendar. *Quarterly Journal of the Royal Meteorological Society*, 139(677), 1961–1963. doi: 10.1002/qj.2178

Heimann, M., Reichstein, M. 2008. Terrestrial ecosystem carbon dynamics and climate feedbacks. *Nature*, 451(7176), 289–292. doi: 10.1038/nature06591

Henry, R.C., Chang, Y.S., Spiegelman, C.H. 2002. Locating nearby sources of air pollution by nonparametric regression of atmospheric concentrations on wind direction. *Atmospheric Environment*, 36, 2237–2244. doi: 10.1016/S1352-2310(02)00164-4

Hernández-Ceballos, M.A., Adame, J.A., Bolívar, J.P., De la Morena, B.A. 2013. Vertical behaviour and meteorological properties of air masses in the southwest of the Iberian Peninsula (1997-2007). *Meteorology and Atmospheric Physics*, 119(3-4), 163–175. doi: 10.1007/s00703-012-0225-5

Hernández-Ceballos, M.A., Skjøth, C.A., García-Mozo, H., Bolívar, J.P., Galán, C. 2014a. Improvement in the accuracy of back trajectories using WRF to identify pollen sources in southern Iberian Peninsula. *International Journal of Biometeorology*, 58(10), 2031–2043. doi: 10.1007/s00484-014-0804-x

Hernandez-Ceballos, M.A., Soares, J., García-Mozo, H., Sofiev, M., Bolivar, J.P., Galán, C. 2014b. Analysis of atmospheric dispersion of olive pollen in southern Spain using SILAM and HYSPLIT models. *Aerobiologia*, 30(3), 239–255. doi: 10.1007/s10453-013-9324-0

Hernández-Ceballos, M.A., García-Mozo, H., Galán, C. 2015a. Cluster analysis of intradiurnal holm oak pollen cycles at peri-urban and rural sampling sites in southwestern Spain. *International Journal of Biometeorology*, 59(8), 971–982. doi: 10.1007/s00484-014-0910-9

Hernández-Ceballos, M.A., Vargas, A., Arnold, D., Bolívar, J.P. 2015b. The role of mesoscale meteorology in modulating the 222Rn concentrations in Huelva (Spain) — impact of

phosphogypsum piles. *Journal of Environmental Radioactivity*, 145, 1–9. doi: 10.1016/j.jenvrad.2015.03.023

Hernández-Ceballos, M.A, Brattich, E., Cinelli, G. 2016. Heat-Wave events in Spain: air mass analysis and impacts on ^{7}Be concentrations. *Advances in Meteorology*, 2016. doi: 10.1155/2016/8026018

Hernández-Ceballos, M.Á., De Felice, L. 2019. Air mass trajectories to estimate the "most likely" areas to be affected by the release of hazardous materials in the atmosphere-feasibility study. *Atmosphere*, 10(5). doi: 10.3390/atmos10050253

Hernández-Paniagua, I.Y., Lowry, D., Clemitshaw, K.C., Fisher, R.E., France, J.L., Lanoisellé, M., Ramonet, M., Nisbet, E.G. 2015. Diurnal, seasonal, and annual trends in atmospheric CO_2 at southwest London during 2000-2012: wind sector analysis and comparison with Mace Head, Ireland. *Atmospheric Environment*, 105, 138–147. doi: 10.1016/j.atmosenv.2015.01.021

Higuchi, K., Worthy, D., Chan, D., Shashkov, A. 2003. Regional source/sink impact on the diurnal, seasonal and inter-annual variations in atmospheric CO_2 at a boreal forest site in Canada. *Tellus, Series B: Chemical and Physical Meteorology,* 55, 115–125. doi: 10.1034/j.1600-0889.2003.00062.x

Hill, J., McSweeney, C., Wright, A-D.G., Bishop-Hurley, G., Kalantar-zadeh, K. 2016. Measuring Methane Production from Ruminants. *Trends in Biotechnology*, 34(1), 26–35. doi: 10.1016/j.tibtech.2015.10.004

Hu, C., Griffis, T.J., Lee, X., Millet, D.B., Chen, Z., Baker, J.M., Xiao, K. 2018. Top-down constraints on anthropogenic CO_2 emissions within an agricultural-urban landscape. *Journal of Geophysical Research: Atmospheres*, 123, 4674–4694. doi: 10.1029/2017JD027881

Hu, H., Wei, W., Chang, C-P. 2020. The relationship between shale gas production and natural gas prices: An environmental investigation using structural breaks. *Science of the Total Environment*, 713, 136545. doi: 10.1016/j.scitotenv.2020.136545

Hu, J., Moore, D., Burns, S., Monson, R. 2010. Longer growing seasons lead to less carbon sequestration by a subalpine forest. *Global Change Biology*,16, 771–783. doi: 10.1111/j.1365-2486.2009.01967.x

Inoue, H.Y., Matsueda, H., Igarashi, Y., Sawa, Y., Wada, A., Nemoto, K., Sartorius, H., Schlosser, C. 2006. Seasonal and long-term variations in atmospheric CO_2 and ^{85}Kr in Tsukuba, Central Japan. *Journal of the Meteorological Society of Japan*, 84 (6), 959–968. doi: 10.2151/jmsj.84.959

IPCC, 1992. Climate Change: The IPCC 1990 and 1992 Assessments. *Intergovernmental Panel on Climate Change*. Cambridge University Press, UK, 180 pp.

IPCC, 1995. IPCC Second Assessment Climate Change 1995. *Intergovernmental Panel on Climate Change*. Cambridge University Press, UK, 73 pp.

IPCC, 2001. Climate Change 2001: The Scientific Basis. *Intergovernmental Panel on Climate Change*. Cambridge University Press, UK, 409 pp.

IPCC, 2007. Climate Change 2007: The Sciences Basis. *Intergovernmental Panel on Climate Change*. Cambridge University Press, UK, 112 pp.

IPCC, 2013. Climate Change 2013: The Physical Sciences Basis. Contribution of Working Group I to the Fifth Assessment Report of the Intergovernmental Panel on Climate Change. Cambridge University Press, UK, 1552 pp.

IPCC, 2014. Summary for Policymakers. In: Climate Change 2014: Mitigation of Climate Change. Contribution of Working Group III to the Fifth Assessment Report of the Intergovernmental Panel on Climate Change. Cambridge University Press, UK, 1454 pp.

IPCC, 2019. Summary for Policymakers. In: Climate Change and Land: an IPCC special report on climate change, desertification, land degradation, sustainable land management, food security, and greenhouse gas fluxes in terrestrial ecosystems. In press, 34 pp.

IPCC. 2020a. Intergovernmental Panel on Climate. https://www.ipcc.ch/about/. Accessed 18 September 2020.

IPCC. 2020b. AR6 Synthesis Report: Climate Change 2022. https://www.ipcc.ch/report/sixth-assessment-report-cycle/. Accessed 25 October 2020.

Isakar, K., Kiisk, M., Realo, E. Suursoo, S. 2016. Lead-210 in the atmospheric air of North and South Estonia: long-term monitoring, and back-trajectory calculations. *Proceedings of the Estonian Academy of Sciences*, 65 (4), 442–451. doi: 10.3176/proc.2016.4.11

Izquierdo, R., Alarcón, M., Mazón, J., Pino, D., De Linares, C., Aguinagalde, X., Belmonte, J. 2017. Are the Pyrenees a barrier for the transport of birch (Betula) pollen from Central Europe to the Iberian Peninsula? *Science of the Total Environment*, 575, 1183–1196. doi: 10.1016/j.scitotenv.2016.09.192

Jain, S.L., Ghude, S.D., Kumar, A., Arya, B.C., Kulkarni, P.S. 2005. Continuous observations of surface air concentration of carbon dioxide and methane at Maitri, Antarctica. *Current Science*, 88, 1941–1948.

Jamil, M., Parsa, S., Majidi, M. 1995. Wind power statistics and an evaluation of wind energy density. *Renewable Energy*, 6, 623–628. doi. org/10.1016/0960-1481(95)00041-H

Jeong, S.J., Ho, C.H., Gim, H.J., Brown, M.E. 2011 Phenology shifts at start vs. end of growing season in temperate vegetation over the Northern Hemisphere for the period1982-2008. *Global Change Biology*,17, 2385–2399. doi: 10.1111/j.1365-2486.2011.02397.x

Jiménez, E., Tapiador, F.J., Sáez-Martínez, F.J. 2015. Atmospheric pollutants in a changing environment: key issues in reactivity and monitoring, global warming, and health. *Environmental Science and Pollution Research*, 22(7), 4789–4792. doi: 10.1007/s11356-014-3850-3

Jung, Y.-Y., Koh, D.-C., Lee, J., Ko, K.-S. 2013. Applications of Isotope Ratio Infrared Spectroscopy (IRIS) to Analysis of Stable Isotopic Compositions of Liquid Water. *Economic and Environmental Geology*, 46(6), 495–508. doi: 10.9719/EEG.2013.46.6.495

Katsoulis, B.D. 1999. The potential for long-range transport of air-pollutants into Greece: a climatological analysis. *Science of the Total Environment*, 231(2–3), 101–113. doi: 10.1016/S0048-9697(99)00100-X

Keeling, C. D., Chin, J.F.S., Whorf, T.P. 1996. Increased activity of northern vegetation inferred from atmospheric CO_2 measurements. *Nature*, 382, 146–149. doi: 10.1038/382146a0

Keeling, R.F. 2007. Deglaciation mysteries. *Science,* 316(5830), 1440-1441. doi:10.1126/science.1142326

Keeling, R.F. 2008. Atmospheric science: Recording earth's vital signs. *Science*, 319(5871), 1771–1772. doi: 10.1126/science.1156761

Kim, H.-S., Chung, Y.S., Tans, P.P., Dlugokencky, E.J. 2015. Decadal trends of atmospheric methane in East Asia from 1991 to 2013. *Air Quality, Atmosphere & Health*, 8, 293–298. doi: 10.1007/s11869-015-0331-x

Kirschke, S., Bousquet, P., Ciais, P., Saunois, M., Canadell, J.G., Dlugokencky, E.J., Bergamaschi, P., Bergmann, D., Blake, D.R., Bruhwiler, L., Cameron-Smith, P., Castaldi, S., Chevallier, F., Feng, L., Fraser, A., Heimann, M., Hodson, E.L., Houweling, S., Josse, B., Fraser, P.J., Krummel, P.B., Lamarque, J.-F., Langenfelds, R.L., Le Quéré, C., Naik, V., O'Doherty, S., Palmer, P.I., Pison, I., Plummer, D., Poulter, B., Prinn, R.G., Rigby, M., Ringeval, B., Santini, M., Schmidt, M., Shindell, D.T., Simpson, I.J., Spahni, R., Steele, L.P., Strode, S.A., Sudo, K., Szopa, S., van der Werf, G.R., Voulgarakis, A., Weele, M., Weiss, R.F., Williams, J.E., Guang, Z. 2013. Three decades of global methane sources and sinks. *Nature Geoscience*, 6, 813–823. doi: 10.1038/ngeo1955

Klimenko, V.V., Klimenko, A.V., Tereshin, A.G. 2019. From Rio to Paris via Kyoto: How the Efforts to Protect the Global Climate Affect the World Energy Development. *Thermal Engineering*, 66(11), 769–778. doi: 10.1134/S0040601519110028

Knoblauch, C., Beer, C., Liebner, S., Grigoriev, M.N., Pfeiffer, E.M. 2018. Methane production as key to the greenhouse gas budget of thawing permafrost. *Nature Climate Change*, 8, 309–312. doi: 10.1038/s41558-018-0095-z

Kottek, M., Grieser, J., Beck, C., Rudolf, B., Rubel, F. 2006. World Map of the Köppen-Geiger climate classification updated. *Meteorologische Zeitschrift*, 15(3), 259–263. doi: 10.1127/0941-2948/2006/0130

Krisp, J.M., Peters, S., Murphy, C.E., Fan, H. 2009. Visual bandwidth selection for kernel density maps. *Photogrammetrie Fernerkundung Geoinformation*, 5, 445–454. doi: 10.1127/1432-8364/2009/0032

Kumar, D., Kumar, A., Kumar, V., Kumar, J., Ravi, P.M. 2013. Study of atmospheric stagnation, recirculation and ventilation potential at Narora Atomic Power Station NPP site. *Environmental Monitoring and Assessment*, 185(4), 2887–2894. doi: 10.1007/s10661-012-2756-0

Le Quéré, C., Andrew, R.M., Canadell, J.G., Sitch, S., Korsbakken, J.I., Peters, G.P., Manning, A.C., Boden, T.A., Tans, P.P., Houghton, R.A., Keeling, R.F., Alin, S., Andrews, O.D., Anthoni, P., Barbero, L., Bopp, L., Chevallier, F., Chini, L.P., Ciais, P., Currie, K., Delire, C., Doney, S.C., Friedlingstein, P., Gkritzalis, T., Harris, I., Hauck, J., Haverd, V., Hoppema, M., Goldewijk K.K., Jain, A.K., Kato, E., Körtzinger, A., Landschützer, P., Lefèvre, N., Lenton, A., Lienert, S., Lombardozzi, D., Melton, J.R., Metzl, N., Millero, F., Monteiro, P.M.S., Munro, D.R., Nabel, J.E.M.S., Nakaoka, S.I., O'Brien, K., Olsen, A., Omar, A.M., Ono, T., Pierrot, D., Poulter, B., Rödenbeck, C., Salisbury, J., Schuster, U., Schwinger, J., Séférian, R., Skjelvan, I., Stocker, B.D., Sutton, A.J., Takahashi, T., Tian, H., Tilbrook, B., van der Laan-Luijkx, I.T., van der Werf, G.R., Viovy, N., Walker, A.P., Wiltshire, A.J., Zaehle, S. 2016. Global carbon budget 2016. *Earth System Science Data*, 8, 605–649. doi: 10.5194/essd-8-605-2016

Lee, J.E., Edwards, J.S., Schmitt, J., Fischer, H., Bock, M., Brook, E.J. 2020. Excess methane in Greenland ice cores associated with high dust concentrations. *Geochimica et Cosmochimica Acta*, 270, 409–430. doi: 10.1016/j.gca.2019.11.020

Lee, T.R., De Wekker, S.F.J., Andrews, A.E., Kofler, J., Williams, J. 2012. Carbon dioxide variability during cold front passages and fair weather days at a forested mountaintop site. *Atmospheric Environment*, 46, 405–416. doi: 10.1016/j.atmosenv.2011.09.068

Lelieveld, J. 2006. Climate change: a nasty surprise in the greenhouse. *Nature*, 443, 405–406. doi: 10.1038/443405a

Li, C., Zhou, L., Qin, D., Liu, L., Qin, X., Wang, Z., Ren, J. 2014. Preliminary study of atmospheric carbon dioxide in a glacial area of the Qilian Mountains, west China. *Atmospheric Environment*, 99, 485–490. doi: 10.1016/j.atmosenv.2014.10.020

Li, X., Liu, E., Zhang, E., Lin, Q., Yu, Z., Nath, B., Yuan, H., Shen, J. 2020. Spatio-temporal variations of sedimentary metals in a large suburban lake in southwest China and the implications for anthropogenic processes. *Science of the Total Environment*, 707, 135650. doi: 10.1016/j.scitotenv.2019.135650

Likuku, A.S. 2006. Factors influencing ambient concentrations of ^{210}Pb and ^{7}Be over the city of Edinburgh (55.9ºN, 03.2ºW). *Journal of Environmental Radioactivity*, 87, 289–304. doi: 10.1016/j.jenvrad.2005.12.006

Lintner, B.R., Buermann, W., Koven, C.D., Fung, I.Y. 2006. Seasonal circulation and Mauna Loa CO_2 variability. *Journal of Geophysical Research Atmospheres*, 111, D13104. doi: 10.1029/2005JD006535

Liu, D.H.F.; Lipták, B.G. 2000. Air pollution. *Boca Ratón*. 256 pp.

Liu, M., Wu, J., Zhu, X., He, H., Jia, W., Xiang, W. 2015. Evolution and variation of atmospheric carbon dioxide concentration over terrestrial ecosystems as derived from eddy covariance measurements. *Atmospheric Environment*, 114, 75–82. doi: 10.1016/j.atmosenv.2015.05.026

Liu, Z., Zheng, C., Wu, Y., Flay, R.G.J., Zhang, K. 2019. Wind tunnel simulation of wind flows with the characteristics of thousand-meter high ABL. *Building and Environment*, 152, 74–86. doi: 10.1016/j.buildenv.2019.02.012

Lo Brano, V., Orioli, A., Ciulla, G., Culotta, S. 2011. Quality of wind speed fitting distributions for the urban area of Palermo, Italy. *Renewable Energy*, 36, 1026–1039. doi: 10.1016/j.renene.2010.09.009

Lörcher, I., Neverla, I. 2015. The dynamics of issue attention in online communication on climate change. *Media and Communication*, 3(1), 17–33. doi: 10.17645/mac.v3i1.253

Lotka, A.J. 1924. Elements of Physical Biology Williams and Wilkins, Baltimore, MD, reprinted 1956. Dover, New York, 495 pp.

Lövbrand, E. 2009. Revisiting the politics of expertise in light of the Kyoto negotiations on land use change and forestry. *Forest Policy and Economics*, 11(5-6), 404–412. doi: 10.1016/j.forpol.2008.08.007

Lozano, R.L., Hernández-Ceballos, M.A., San Miguel, E.G., Adame, J.A., Bolívar, J.P. 2012. Meteorological factors influencing the ^{7}Be and ^{210}Pb concentrations in surface air from the southwestern Iberian Peninsula. *Atmospheric Environment*, 63, 168–178. doi: 10.1016/j.atmosenv.2012.09.052

Ma, Z., Peng, C., Zhu, Q., Chen, H., Yu, G., Li, W., Zhou, W., Wang, W., Zhang, W. 2012. Regional drought-induced reduction in the biomass carbon sink of Canada's boreal forests. *Proceedings of the National Academy of Sciences of the United States of America*,109, 2423–2427. doi: 10.1073/pnas.1111576109

Marquis, M., Tans, P. 2008. Climate change: Carbon crucible. *Science, 320*(5875), 460–461. doi:10.1126/science.1156451

Martins, C.S.C., Macdonald, C.A., Anderson, I.C., Singh, B.K. 2016. Feedback responses of soil greenhouse gas emissions to climate change are modulated by soil characteristics in dryland ecosystems. *Soil Biology and Biochemistry*, 100, 21–32. doi: 10.1016/j.soilbio.2016.05.007

Marx, W., Haunschild, R., French, B., Bornmann, L. 2017. Slow reception and under-citedness in climate change research: A case study of Charles David Keeling, discoverer of the risk of global warming. *Scientometrics*, 112(2), 1079–1092. doi: 10.1007/s11192-017-2405-z

McAlevey, L.G., Stent, A.F. 2018. Kurtosis: a forgotten moment. *International Journal of Mathematical Education in Science and Technology*, 49(1), 120–130. doi: 10.1080/0020739X.2017.1357848

McClure, C.D., Jaffe, D.A., Gao, H. 2016. Carbon dioxide in the free troposphere and boundary layer at the Mt. Bachelor Observatory. *Aerosol and Air Quality Research,* 16(3), 717–728. doi:10.4209/aaqr.2015.05.0323

Megido, L., Negral, L., Castrillón, L., Fernández-Nava, Y., Suárez-Peña, B., Marañón, E. 2017. Impact of secondary inorganic aerosol and road traffic at a suburban air quality monitoring station. *Journal of Environmental Management*, 189, 36–45. doi: 10.1016/j.jenvman.2016.12.032

Menon, J. S., S.M, S. N. 2018. Statistical distribution and particle dosimetry models to estimate personal exposure at urban sidewalks of tropical climate. *Sustainable Cities and Society*, 40, 254–265. doi:10.1016/j.scs.2017.09.005

Miller, K.M., McGill, B.J. 2017. Land use and life history limit migration capacity of eastern tree species. *Global Ecology and Biogeography*, 27(1), 57–67. doi: 10.1111/geb.12671

Mitsakou, C., Kallos, G., Papantoniou, N., Spyrou, C., Solomos, S., Astitha, M., Housiadas, C. 2008. Saharan dust levels in Greece and received inhalation doses. *Atmospheric Chemistry and Physics*, 8, 7181–7192. doi: 10.5194/acp-8-7181-2008

Morris, J., Paltsev, S., Ku, A. Y. 2019. Impacts of China's emissions trading schemes on deployment of power generation with carbon capture and storage. *Energy Economics*, 81, 848–858. doi: 10.1016/j.eneco.2019.05.014

Müller, H.-G. 1988. Nonparametric regression analysis of longitudinal data. *Lecture Notes in Statistics*, 46. Springer, NY, 208 pp. doi: 10.1007/978-1-4612-3926-0

Munk, W.H. 1997. Colloquium Paper This paper was presented at a colloquium entitled "Carbon Dioxide and Climate Change", organized by Charles D. Keeling, held November 13-15, 1995, at the National Academy of Sciences, Irvine, CA. Tribute to Roger Revelle and his contribution to studies of carbon dioxide and climate change. *Proceedings of the National Academy of Sciences*, 94, 8275–8279.

Murayama, S., Saigusa, N., Chan, D., Yamamoto, S., Kondo, H., Eguchi, Y. 2003. Temporal variations of atmospheric CO_2 concentration in a temperate deciduous forest in central Japan. *Tellus, Series B: Chemical and Physical Meteorology*, 55, 232–243. doi: 10.1034/j.1600-0889.2003.00061.x

Nakazawa, T., Ishizawa, M., Higuchi, K., Trivett, N.B.A. 1997. Two curve fitting methods applied to CO_2 flask data. *Environmetrics*, 8, 197–218. doi: 10.1002/(SICI)1099-095X(199705)8:3<197::AID-ENV248>3.0.CO;2-C

Nisbet, E.G., Dlugokencky, E.J., Bousquet, P. 2014. Methane on the rise—again. *Atmospheric Science*, 343, 493–495. doi: 10.1126/ science.1247828

NOAA. 2016. National Oceanic and Atmospheric Administration, Global Monitoring Division. http://www.esrl.noaa.gov/gmd/. Accessed 2 November 2020.

NOAA. 2017a. CO_2 globally averaged marine surface monthly mean data. ftp://aftp.cmdl.noaa.gov/products/trends/co2/co2_mm_gl.txt. Accessed 25 September 2020.

NOAA. 2017b. CH_4 globally averaged marine surface monthly mean data. ftp://aftp.cmdl.noaa.gov/products/trends/ch4/ch4_mm_gl.txt. Accessed 11 October 2020.

NOAA. 2017c. Annual Increase in Globally-Averaged Atmospheric Methane. https://www.esrl.noaa.gov/gmd/ccgg/trends_ch4/#global_growth. Accessed 15 August 2020.

NOAA. 2020a. Global Mean CO_2 mixing ratios. https://data.giss.nasa.gov/modelforce/ghgases/Fig1A.ext.txt. Accessed 15 August 2020.

NOAA. 2020b. Global Radiative Forcing, CO_2-equivalent mixing ratio. https://www.esrl.noaa.gov/gmd/aggi/aggi.html. Accessed 15 August 2020.

NOAA. 2020c. Monthly Average Mauna Loa CO_2. https://www.esrl.noaa.gov/gmd/ccgg/trends/. Accessed 15 August 2020.

NOAA. 2020d. History of atmospheric carbon dioxide from 800,000 years ago until January, 2019. https://www.esrl.noaa.gov/gmd/ccgg/trends/history.html. Accessed 15 August 2020.

NOAA. 2020e. Global CH_4 monthly means. https://www.esrl.noaa.gov/gmd/ccgg/trends_ch4/. Accessed 15 August 2020.

Notario, A., Adame, J.A., Bravo, I., Cuevas, C.A., Aranda, A., Díaz-de-Mera, Y., Rodríguez, A. 2014. Air pollution in the plateau of the Iberian Peninsula. *Atmospheric Research*, 145–146, 92–104. doi: org/10.1016/j.atmosres.2014.03.021

Oney, B., Gruber, N., Henne, S., Leuenberger, M., Brunner, D. 2017. A CO-based method to determine the regional biospheric signal in atmospheric CO_2. *Tellus B: Chemical and Physical Meteorology*, 69(1), 1353388. doi: 10.1080/16000889.2017.1353388. 1-24

Paredes, V. 2013. Medida y parametrización de los flujos de CO_2 en un uso de suelo agrícola de la meseta utilizando datos en superficie y teledetección. *Universidad de Valladolid*. doi: 10.35376/10324/3823

Parry, I. 2020. Increasing carbon pricing in the EU: Evaluating the options. *European Economic Review*, 121, 103341. doi: 10.1016/j.euroecorev.2019.103341

Pauw, P., Mbeva, K., van Asselt, H. 2019. Subtle differentiation of countries' responsibilities under the Paris Agreement. *Palgrave Communications*, 5(1). doi: 10.1057/s41599-019-0298-6

Pedersen, I.T., Holmen, K., Hermansen, O. 2005. Atmospheric methane at Zeppelin Station in Ny-Ålesund: Presentation and analysis of in situ measurements. *Journal of Environmental Monitoring*, 7, 488–492. doi: 10.1039/b416934d

Peltola, O., Hensen, A., Helfter, C., Belelli Marchesini, L., Bosveld, F.C., van den Bulk, W.C.M., Elbers, J.A., Haapanala, S., Holst, J., Laurila, T., Lindroth, A., Nemitz, E., Röckmann, T., Vermeulen, A.T., Mammarella, I. 2014. Evaluating the performance of commonly used gas analysers for methane eddy covariance flux measurements: the InGOS inter-comparison field experiment. *Biogeosciences*, 11(12), 3163–3186. doi: 10.5194/bg-11-3163-2014

Peng, S., Chen, A., Xu, L., Cao, C., Fang, J., Myneni, R.B., Pinzon, J.E., Tucker, C.J., Piao, S. 2011. Recent change of vegetation growth trend in China. *Environmental Research Letters*, 6, 044027. doi: 10.1088/1748-9326/6/4/044027

Peña, D., Tiao, G.C., Tsay, R.S. 2001. A course in time series analysis. *Wiley series in probability and statistics*. Wiley, New York. 494 pp.

Pérez, I.A., García, M.A., Sánchez, M.L., de Torre, B. 2004a. Analysis of height variations of sodar-derived wind speeds in Northern Spain. *Journal of Wind Engineering and Industrial Aerodynamics*, 92(10), 875–894. doi: 10.1016/j.jweia.2004.05.002

Pérez, I. A., García, M. Á., Sánchez, M. L., De Torre, B. 2004b. Autocorrelation analysis of meteorological data from a RASS sodar. *Journal of Applied Meteorology,* 43(8), 1213–1223. doi:10.1175/1520-0450(2004)043<1213:AAOMDF>2.0.CO;2

Pérez, I.A., Sánchez, M.L., García, M.Á., De Torre, B. 2009a. Daily and annual cycle of CO_2 concentration near the surface depending on boundary layer structure at a rural site in Spain. *Theoretical and Applied Climatology*, 98, 269–277. doi: 10.1007/s00704-009-0112-2

Pérez, I.A., Sánchez, M.L., García, M.Á., De Torre, B. 2009b. CO_2 transport by urban plumes in the upper Spanish plateau. *Science of the Total Environment*, 407, 4934–4938. doi: 10.1016/j.scitotenv.2009.05.037

Pérez, I.A., Sánchez, M.L., García, M.A., De Torre, B. 2009c. Boundary layer structure and stability classification validated with CO_2 concentrations over the Northern Spanish Plateau. *Annals of Geophysics*, 27, 339–349. doi: 10.5194/angeo-27-339-2009

Pérez, I.A., Sánchez, M.L., García, M.A., Paredes, V. 2011. Relationship between CO_2 at a rural site and integral measures of atmospheric stagnation, recirculation and ventilation. *Naturwissenschaften*, 98, 565–574. doi: 10.1007/s00114-011-0800-5

Pérez, I.A., Sánchez, M.L., García, M.A., Pardo, N. 2012. Analysis and fit of surface CO_2 concentrations at a rural site. *Environmental Science and Pollution Research*, 19, 3015–3027. doi: 10.1007/s11356-012-0813-4

Pérez, I.A., Sánchez, M.L., García, M.A., Pardo, N. 2015a. Analysis of air mass trajectories in the northern plateau of the Iberian Peninsula. *Journal of Atmospheric and Solar-Terrestrial Physics*, 134, 9–21. doi: 10.1016/j.jastp.2015.09.003

Pérez, I.A., Artuso, F., Mahmud, M., Kulshrestha, U., Sánchez, M.L., García, M.A. 2015b. Applications of air mass trajectories. *Advances in Meteorology*, 2015, 1–20. doi: 10.1155/2015/284213

Pérez, I.A., Sánchez, M.L., García, M.A., Ozores, M., Pardo, N. 2015c. Cluster analysis applied to CO_2 concentrations at a rural site. *Environmental Science and Pollution Research*, 22(3), 1954–1962. doi: 10.1007/s11356-014-3679-9

Pérez, I.A., Sánchez, M.L., García, M.Á., Pardo, N. 2016. Features of the annual evolution of CO_2 and CH_4 in the atmosphere of a Mediterranean climate site studied using a nonparametric and a harmonic function. *Atmospheric Pollution Research*, 7, 1013–1021. doi: 10.1016/j.apr.2016.06.006

Pérez, I.A., Sánchez, M.L., García, M.Á., Pardo, N. 2017. Trend analysis of CO_2 and CH_4 recorded at a semi-natural site in the northern plateau of the Iberian Peninsula. *Atmospheric Environment*, 151, 24–33. doi: 10.1016/j.atmosenv.2016.11.068

Pérez, I.A., Sánchez, M.L., García, M.Á, Pardo, N., Fernández-Duque, B. 2018a. Analysis of the airflow at the centre of the upper plateau on the Iberian Peninsula and its link to CO_2 and CH_4 concentrations. International Journal of Climatology, 38(4), 2126–2137. doi:10.1002/joc.5323

Pérez, I.A., Sánchez, M.L., García, M.Á, Pardo, N., Fernández-Duque, B. 2018b. The influence of meteorological variables on CO_2 and CH_4 trends recorded at a semi-natural station. *Journal of Environmental Management*, 209, 37–45. doi: 10.1016/j.jenvman.2017.12.028

Pérez, I.A., Sánchez, M.L., García, M. Á., Pardo, N. 2018c. Influence of air parcel trajectories on CO_2 and CH_4 concentrations in the northern plateau of the Iberian Peninsula. *Journal of Atmospheric and Solar-Terrestrial Physics*, 167, 58–65. doi:10.1016/j.jastp.2017.10.015

Pérez, I.A., Sánchez, M.L., García, M.Á, Pardo, N. 2019. Sensitivity of CO_2 and CH_4 annual cycles to different meteorological variables at a rural site in northern Spain. *Advances in Meteorology*, 2019. doi: 10.1155/2019/9240568

Pérez, I.A., Sánchez, M.L., García, M.A., Pardo, N., Fernández-Duque, B. 2020. Statistical analysis of the CO_2 and CH_4 annual cycle on the northern plateau of the Iberian peninsula. *Atmosphere*, 11, 769. doi:10.3390/ATMOS11070769

Piao, S., Ciais, P., Friedlingstein, P., Peylin, P., Reichstein, M., Luyssaert, S., Margolis, H., Fang, J., Barr, A., Chen, A., Grelle, A., Hollinger, D.Y., Laurila, T., Lindroth, A., Richardson, A.D., Vesale, T. 2008. Net carbon dioxide losses of northern ecosystem in response to autumn warming. *Nature*, 451, 49–52. doi: 10.1038/nature06444

Piao, S., Wang, X., Ciais, P., Zhu, B., Wang, T., Liu, J., 2011. Changes in satellite-derived vegetation growth trend in temperate and boreal Eurasia from 1982 to 2006. *Global Change Biology*, 17, 3228–3239. doi: 10.1111/j.1365-2486.2011.02419.x

Piao, S., Liu, Z., Wang, Y., Ciais, P., Yao, Y., Peng, S., Chevallier, F., Friedlingstein, P., Janssens, I.A., Peñuelas, J., Sitch, S., Wang, T. 2017. On the causes of trends in the seasonal amplitude of atmospheric CO_2. *Global Change Biology*, 24(2), 608–616. doi:10.1111/gcb.13909

Plaza, M.P., Alcázar, P., Hernández-Ceballos, M.A., Galán, C. 2016. Mismatch in aeroallergens and airborne grass pollen concentrations. *Atmospheric Environment*, 144, 361–369. doi: 10.1016/j.atmosenv.2016.09.008

Prather, M.J., Holmes, C.D., Hsu, J. 2012. Reactive greenhouse gas scenarios: Systematic exploration of uncertainties and the role of atmospheric chemistry. *Geophysical Research Letters*, 39(9), L09803. doi: 10.1029/2012GL051440

Pu, J.J., Xu, H.H., He, J., Fang, S.X., Zhou, L.X. 2014. Estimation of regional background concentration of CO_2 at Lin'an Station in Yangtze River Delta, China. *Atmospheric Environment*, 94, 402–408. doi: 10.1016/j.atmosenv.2014.05.060

Rahn, T.A., McDowell, N., Powers, H. 2008. Continuous isotopic CO_2 measurements by Wavelength-Scanned Cavity Ring Down Spectroscopy: studies of exchange processes in terrestrial ecosystems. https://www.picarro.com/support/literature/continuous_isotopic_co2_measurements_by_wavelength_scanned_cavity_ring_down. Accessed 21 September 2020.

Ramos, M.C., Balasch, J.C., Martínez-Casasnovas, J. A. 2012. Seasonal temperature and precipitation variability during the last 60 years in a Mediterranean climate area of Northeastern Spain: a multivariate analysis. *Theoretical and Applied Climatology*, 110(1-2), 35–53. doi: 10.1007/s00704-012-0608-z

Rečka, L., Ščasný, M. 2017. Impacts of reclassified brown coal reserves on the energy system and deep decarbonisation target in the Czech Republic. *Energies*, 10(12), 1947. doi: 10.3390/en10121947

Rella, C.W., Chen, H., Andrews, A.E., Filges, A., Gerbig, C., Hatakka, J., Karion, A., Miles, N.L., Richardson, S.J., Steinbacher, M., Sweeney, C., Wastine, B., Zellweger, C. 2013. High accuracy measurements of dry mole fractions of carbon dioxide and methane in humid air. *Atmospheric Measurement Techniques*, 6(3), 837–860. doi: 10.5194/amt-6-837-2013

Reum, F., Gerbig, C., Lavric, J.V., Rella, C.W., Göckede, M. 2019. Correcting atmospheric CO_2 and CH_4 mole fractions obtained with Picarro analyzers for sensitivity of cavity pressure to water vapor. *Atmospheric Measurement Techniques*, 12, 1013–1027. doi: 10.5194/amt-12-1013-2019

Richardson, A.D., Black, T.A., Ciais, P., Delbart, N., Friedl, M.A., Gobron, N., Hollinger, D.Y.,Kutsch, W.L., Longdoz, B., Luyssaert, S., Migliavacca, M., Montagnani, L., Munger,J.W., Moors, E., Piao, S.L., Rebmann, C., Reichstein, M., Saigusa, N., Tomelleri, E.,Vargas, R., Varlagin, A., 2010. Influence of spring and autumn phonological transitions on forest

ecosystem productivity. Philosophical Transactions of the Royal Society. B Biological Sciences, 365B, 3227–3246. doi: 10.1098/rstb.2010.0102

Riza, R., Ariwahjoedi, B., Sulaiman, S.A. 2011. On the Numerical Exploration of Zero-Dimensional Greenhouse Model using Newton-Raphson and Steepest Descent Methods. *International Journal of Environmental Science and Development*, 2(3), 233–238. doi: 10.7763/IJESD.2011.V2.130

Roberts, D. 2016. A global roadmap for climate change action: From COP17 in Durban to COP21 in Paris. *South African Journal of Science*, 112(5-6). doi: 10.17159/sajs.2016/a0158

Rodríguez-Cortés, F.J., Mateu, J. 2015. Second-order smoothing of spatial point patterns with small sample sizes: a family of kernels. *Stochastic Environmental Research and Risk Assessment*, 29, 295–308. doi: 10.1007/s00477-014-0944-x

Román-Cascón, C., Yagüe, C., Sastre, M., Maqueda, G., Salamanca, F., Viana, S. 2012. Observations and WRF simulations of fog events at the Spanish Northern Plateau. *Advances in Science and Research*, 8(1), 11–18. doi: 10.5194/asr-8-11-2012

Román-Cascón, C., Steeneveld, G.J., Yagüe, C., Sastre, M., Arrillaga, J.A., Maqueda, G. 2016a. Forecasting radiation fog at climatologically contrasting sites: evaluation of statistical methods and WRF. *Quarterly Journal of the Royal Meteorological Society*, 142(695), 1048–1063. doi: 10.1002/qj.2708

Román-Cascón, C., Yagüe, C., Steeneveld, G-J., Sastre, M., Arrillaga, J.A., Maqueda, G. 2016b. Estimating fog-top height through near-surface micrometeorological measurements. *Atmospheric Research*, 170, 76–86. doi: 10.1016/j.atmosres.2015.11.016

Román-Cascón, C., Yagüe, C., Steeneveld, G-J., Morales, G., Arrillaga, J.A., Sastre, M., Maqueda, G. 2019. Radiation and cloud-base lowering fog events: Observational analysis and evaluation of WRF and HARMONIE. *Atmospheric Research*, 229, 190–207. doi: 10.1016/j.atmosres.2019.06.018

Rouaud, M. 2017. Probability, Statistics and Estimation. http://www.incertitudes.fr/book.pdf. Accessed 9 October 2020.

Sachs, L. 1978. Applied Statistics: a Handbook of Techniques, Fifth ed. Springer, New York.

San José, R., Casanova, J.L., Viloria, R.E., Casanova, J. 1985. Evaluation of the turbulent parameters of the unstable surface boundary layer outside Businger´s range. *Atmospheric Environment*, 19(10), 1555–1561.

San Miguel, E.G., Hernández-Ceballos, M.A., García-Mozo, H., Bolívar, J.P. 2019. Evidences of different meteorological patterns governing ^{7}Be and ^{210}Pb surface levels in the southern Iberian Peninsula. *Journal of Environmental Radioactivity*, 198, 1–10. doi: 10.1016/j.jenvrad.2018.12.007

Sánchez, M.L., Ozores, M.I., López, M.J., Colle, R., De Torre, B., García, M.A., Pérez, I. 2003. Soil CO_2 fluxes beneath barley on the central Spanish plateau. *Agricultural and Forest Meteorology*, 118, 85–95. doi: 10.1016/S0168-1923(03)00066-2

Sánchez, M.L., García, M.Á., De Torre, B., Pérez, I. 2005. O_3 and CO_2 concentrations in a rural area in central Spain. Air Pollution XIII, 82, 401–410. WIT Transactions on Ecology and the Environment, UK.

Sánchez, M.L., García, M.A., Pérez, I.A., de Torre, B. 2008. Evaluation of surface ozone measurements during 2000-2005 at a rural area in the upper Spanish plateau. *Journal of Atmospheric Chemistry*, 60(2), 137–152. doi: 10.1007/s10874-008-9113-2

Sánchez, M.L., Pérez, I.A., García, M.A. 2010. Study of CO_2 variability at different temporal scales recorded in a rural Spanish site. *Agricultural and Forest Meteorology*, 150(9), 1168–1173. doi: 10.1016/j.agrformet.2010.04.018

Sánchez, M.L., García, M.Á, Pérez, I.A., Pardo, N. 2014. CH_4 continuous measurements in the upper Spanish plateau. *Environmental Monitoring and Assessment*, 186(5), 2823–2834. doi: 10.1007/s10661-013-3583-7

Satar, E., Berhanu, T.A., Brunner, D., Henne, S., Leuenberger, M. 2016. Continuous CO_2/ CH_4/CO measurements (2012-2014) at Beromünster tall tower station in Switzerland. *Biogeosciences*, 13 (9), 2623–2635. doi: 10.5194/bg-13-2623-2016

Satar, E., Berhanu, T.A., Brunner, D., Henne, S., Leuenberger, M. 2017. Four Years of Continuous CO_2/CH_4/CO Measurements (2012-2016) at Beromünster Tall Tower Station in

Switzerland. Poster presented at the 10th International Carbon Dioxide Conference. August 2017 Interlaken, Switzerland, pp. 21–25. Available at: http://www.icdc10.unibe.ch/program/presentations/. Accessed 19 October 2020.

Saunois, M., Stavert, A.R., Poulter, B., Bousquet, P., Canadell, J.G., Jackson, R.B., Raymond, P.A., Dlugokencky, E.J., Houweling, S., Patra, P.K., Ciais, P., Arora, V.K., Bastviken, D., Bergamaschi, P., Blake, D.R., Brailsford, G., Bruhwiler, L., Carlson,K.M., Carrol, M., Castaldi, S., Chandra, N., Crevoisier, C., Crill, P.M., Covey, K., Curry,C.L., Etiope, G., Frankenberg, C., Gedney, N., Hegglin, M.I., Höglund-Isakson, L., Hugelius, G., Ishizawa, M., Ito, A., Janssens Maenhout, G., Jensen, K.M., Joos, F., Kleinen, T., Krummel, P.B., Langenfelds, R.L., Laruelle, G.G., Liu, L., Machida, T., Maksyutov, S., McDonald, K.C., McNorton, J., Miller, P.A., Melton, J.R., Morino, I., Müller, J., Murgia-Flores, F., Naik, V., Niwa, Y., Noce, S., O´Doherty, S., Parker,R.J., Peng, C., Peng, S., Peters, G.P., Prigent, C., Prinn, R., Ramonet, M., Regnier, P., Riley, W.J., Rosentreter, J.A., Segers, A., Simpson, I.J., Shi, H., Smith, S.J., Steele,P.L., Thornton, B.F., Tian, H., Tohjima, Y., Tubiello, F.N., Tsuruta, A., Viovy, N., Voulgarakis, A., Weber, T.S., van Weele, M., van der Werf, G.R., Weiss, R.F., Worthy,D., Wunch, D., Yin, Y., Yoshida, Y., Zhang, W., Zhang, Z., Zhao, Y., Zheng, B., Zhu, Q., Zhu, Q., Zhuang, Q., 2020. The Global Methane Budget 2000–2017. *Earth System Science Data*, 12, 1561–1623. doi: 10.5194/essd-2019-128

Schibig, M.F., Steinbacher, M., Buchmann, B., van der Laan-Luijkx, I.T., van der Laan, S., Ranjan, S., Leuenberger, M. 2015. Comparison of continuous in situ CO_2 observations at Jungfraujoch using two different measurement techniques. *Atmospheric Measurement Techniques*, 8 (1), 57–68. doi: 10.5194/amt-8-57-2015

Schmidt, M. 2003. The Schauinsland CO_2 record: 30 years of continental observations and their implications for the variability of the European CO_2 budget. *Journal of Geophysical Research*, 108, 4619. doi: 10.1029/2002JD003085

Schmidt, M., Lopez, M., Yver Kwok, C., Messager, C., Ramonet, M., Wastine, B., Vuillemin, C., Truong, F., Gal, B., Parmentier, E., Cloué, O., Ciais, P. 2014. High-precision quasi-continuous atmospheric greenhouse gas measurements at Trainou tower (Orléans forest, France). *Atmospheric Measurement Techniques*, 7(7), 2283–2296. doi: 10.5194/amt-7-2283-2014

Schumann, U., Weinzierl, B., Reitebuch, O., Schlager, H., Minikin, A., Forster, C., Baumann, R., Sailer, T., Graf, K., Mannstein, H., Voigt, C., Rahm, S., Simmet, S., Scheibe, M., Lichtenstern, M., Stock, P., Rüba, H., Schäuble, D., Tafferner, A., Rautenhaus, M., Gerz, T., Ziereis, H., Krautstrunk, M., Mallaun, C., Gayet, J.F., Lieke, K., Kandler, K., Ebert, M., Weinbruch, S., Stohl, A., Gasteiger, J., Groß, S., Freudenthaler, V., Wiegner, M., Ansmann, A., Tesche, M., Olafsson, H., Sturm, K. 2011. Airborne observations of the Eyjafjalla volcano ash cloud over Europe during air space closure in April and May 2010. *Atmospheric Chemistry and Physics*, 11(5), 2245–2279. doi: 10.5194/acp-11-2245-2011

Scott, D.W. 1992. Multivariate density estimation: theory, practice, and visualization. Wiley, New York.

Silverman, B.W. 1986. Density Estimation for Statistics and Data Analysis. Chapman & Hall/CRC, 176 pp.

Simsek, Y., Lorca, Á., Urmee, T., Bahri, P., Escobar, R. 2019. Review and assessment of energy policy developments in Chile. *Energy Policy*, 127, 87–101. doi: 10.1016/j.enpol.2018.11.058

Snyder, J.P. 1987. Map Projections–A Working Manual. U.S. Government Printing Office, Washington, 397 pp.

Soler, M.R., Udina, M., Ferreres, E. 2014. Observational and Numerical Simulation Study of a Sequence of Eight Atmospheric Density Currents in Northern Spain. *Boundary-Layer Meteorology*, 153(2), 195–216. doi: 10.1007/s10546-014-9942-2

Song, X., Wang, G., Ran, F., Huang, K., Sun, J., Song, C. 2020. Soil moisture as a key factor in carbon release from thawing permafrost in a boreal forest. *Geoderma*, 357. doi: 10.1016/j.geoderma.2019.113975

Sorribas, M., Ogren, J.A, Olmo, F.J., Quirantes, A., Fraile, R., Gil-Ojeda, M., Alados-Arboledas, L. 2015. Assessment of african desert dust episodes over the southwest Spain at sea level using in situ aerosol optical and microphysical properties. *Tellus, Series B: Chemical and Physical Meteorology*, 67(1), 27482. doi: 10.3402/tellusb.v67.27482

Sorribas, M., Andrews, E., Ogren, J.A., del Águila, A., Fraile, R., Sheridan, P., Yela, M. 2019. Climatological study for understanding the aerosol radiative effects at southwest Atlantic coast of Europe. *Atmospheric Environment*, 205, 52–66. doi: 10.1016/j.atmosenv.2019.02.017

Sreenivas, G., Mahesh, P., Subin, J., Lakshmi Kanchana, A., Venkata Narasimha Rao, P., Kumar Dadhwal, V. 2016. Influence of Meteorology and interrelationship with greenhouse gases (CO_2 and CH_4) at a suburban site of India. *Atmospheric Chemistry and Physics*, 16(6), 3953–3967. doi: 10.5194/acp-16-3953-2016

Srivastava, S., Naja, M., Thouret, V. 2015. Influences of regional pollution and long range transport over Hyderabad using ozone data from MOZAIC. *Atmospheric Environment*, 117, 135–146. doi: 10.1016/j.atmosenv.2015.06.037

Stohl, A. 1998. Computation, accuracy and applications of trajectories - A review and bibliography. *Atmospheric Environment*, 32(6), 947–966. doi:10.1016/S1352-2310(97)004573

Stone, C.J. 1977. Consistent Nonparametric Regression. *Annals of Statistics*, 5, 595–620.

Sun, Y., Bian, L., Tang, J., Gao, Z., Lu, C., Schnell, R.C. 2014. CO_2 monitoring and background mole fraction at Zhongshan Station, Antarctica. *Atmosphere*, 5, 686–698. doi: 10.3390/atmos5030686

Surkova, G. 2013. Air recirculation and ventilation in the coastal regions of the Black Sea. *Open Geosciences*, 5(2), 196–207. doi:10.2478/s13533-012-0126-7

Tang, S., Zhang, Y., Guo, Y., Zhai, X., Wilkes, A., Han, G., Jiang, Y., Liu, K., Zhou, P., Wang, K., Wang, C. 2015. Changes of soil CO_2 flux under different stocking rates during spring-thaw period in a northern desert steppe, China. *Atmospheric Environment*, 122, 343–348. doi: 10.1016/j.atmosenv.2015.09.073

Tans, P.P., Conway, T.J., Nakazawa, T. 1989. Latitudinal distribution of the sources and sinks of atmospheric carbon dioxide derived from surface observations and an atmospheric transport model. *Journal of Geophysical Research*, 94(D4), 5151–5172. doi: 10.1029/JD094iD04p05151

Terradellas, E., Morales, G., Cuxart, J., Yagüe, C. 2001. Wavelet methods: application to the study of the stable atmospheric boundary layer under non-stationary conditions. Dynamics of Atmospheres and Oceans, 34, 225–244. doi: 10.1016/S0377-0265(01)00069-0

Timokhina, A.V., Prokushkin, A.S., Onuchin, A.A., Panov, A.V., Kofman, G.B., Verkhovets, S.V., Heimann, M. 2015. Long-term trend in CO_2 concentration in the surface atmosphere over central Siberia. *Russian Meteorology and Hydrology,* 40(3), 186–190. doi:10.3103/S106837391503005X

Tiwari, Y.K., Revadekar, J.V., Kumar, K.R. 2013. Variations in atmospheric carbon dioxide and its association with rainfall and vegetation over India. *Atmospheric Environment,* 68, 45–51. doi:10.1016/j.atmosenv.2012.11.040

Toledano, C., Cachorro, V.E., de Frutos, A.M., Sorribas, M., Prats, N., de la Morena, B.A. 2007. Inventory of African desert dust events over the southwestern Iberian Peninsula in 2000-2005 with an AERONET Cimel Sun photometer. *Journal of Geophysical Research Atmospheres*, 112(21), D21201. doi: 10.1029/2006JD008307

Turner, D.B. 1994. Workbook of Atmospheric Dispersion Estimates, 2nd edn. *An Introduction to Dispersion Modeling*. CRC Press, Boca Raton, Florida, 184 pp.

Udina, M., Soler, M.R., Viana, S., Yagüe, C. 2013. Model simulation of gravity waves triggered by a density current. *Quarterly Journal of the Royal Meteorological Society*, 139(672), 701–714. doi: 10.1002/qj.2004

Uglietti, C., Leuenberger, M., Brunner, D. 2011. European source and sink areas of CO_2 retrieved from Lagrangian transport model interpretation of combined O_2 and CO_2 measurements at the high alpine research station Jungfraujoch. *Atmospheric Chemistry and Physics*, 11, 8017–36. doi: 10.5194/acp-11-8017-2011

ul-Haq, Z., Tariq, S., Ali, M. 2017. Spatiotemporal assessment of CO_2 emissions and its satellite remote sensing over Pakistan and neighboring regions. *Journal of Atmospheric and Solar-Terrestrial Physics*, 152–153, 11–19. doi: 10.1016/j.jastp.2016.11.001

Valverde, V., Pay, M.T., Baldasano, J.M. 2016. Ozone attributed to Madrid and Barcelona on-road transport emissions: Characterization of plume dynamics over the Iberian Peninsula. *Science of the Total Environment*, 543, 670–82. doi: 10.1016/j.scitotenv.2015.11.070

van der Wal, J.T., Stijnen, J., Janssen, L.H.J.M. 1997. Using observed methane concentrations in assessing regional emissions in Europe. Air Pollution Modelling, Monitoring and Management, 15, 787–796. WIT Transactions on Ecology and the Environment, UK.

van Drooge, B.L., Sicard, M., Stohl, A., Fontal, M., Bravo, N., Muñoz, A., Lange, D., Fernández, P., Grimalt, J.O. 2016. Detection and simulation of wildfire smoke impacting a Mediterranean urban atmosphere. *Atmospheric Pollution Research*, 7, 494–502. doi: 10.1016/j. apr.2015.12.003

Vardag, S.N., Hammer, S., O'Doherty, S., Spain, T.G., Wastine, B., Jordan, A., Levin, I. 2014. Comparisons of continuous atmospheric CH_4, CO_2 and N_2O measurements - results from a travelling instrument campaign at Mace Head. *Atmospheric Chemistry and Physics*, 14(16), 8403–8418. doi: 10.5194/acp-14-8403-2014

Velasco-Merino, C., Mateos, D., Toledano, C., Prospero, J.M., Molinie, J., Euphrasie-Clotilde, L., González, R., Cachorro, V.E., Calle, A., de Frutos, A.M. 2018. Impact of long-range transport over the Atlantic Ocean on Saharan dust optical and microphysical properties based on AERONET data. *Atmospheric Chemistry and Physics*, 18(13), 9411–9424. doi: 10.5194/acp-18-9411-2018

Vermeulen, A.T., Hensen, A., Popa, M.E., van den Bulk, W.C.M., Jongejan, P.A.C. 2011. Greenhouse gas observations from Cabauw Tall Tower (1992–2010). *Atmospheric Measurement Techniques*, 4, 617–644. doi: 10.5194/amt-4-617-2011

Viana, S., Yagüe, C., Maqueda, G. 2009. Propagation and effects of a mesoscale gravity wave over a weakly-stratified nocturnal boundary layer during the SABLES2006 field campaign. *Boundary-Layer Meteorology*, 133(2), 165–188. doi: 10.1007/s10546-009-9420-4

Viana, S., Terradellas, E., Yagüe, C. 2010. Analysis of gravity waves generated at the top of a drainage flow. *Journal of the Atmospheric Sciences*, 67(12), 3949–3966. doi: 10.1175/2010JAS3508.1

Visconti, G. 2016. Fundamentals of physics and chemistry of the atmosphere, 2nd edn. *Springer*. doi: 10.1007/978-3-319-29449-0

Wada, A., Sawa, Y., Matsueda, H., Taguchi, S., Murayama, S., Okubo, S., Tsutsumi, Y. 2007. Influence of continental air mass transport on atmospheric CO_2 in the western North Pacific. *Journal of Geophysical Research: Atmospheres*, 112, D07311. doi: 10.1029/2006JD007552

Walford, N. 2011. Practical Statistics for Geographers and Earth Scientists. Wiley-Blackwell, New Yersey, 440 pp.

Wand, M.P., Jones, M.C. 1995. Kernel smoothing. *Monographs on Statistics and Applied Probability*, 60. Chapman & Hall, London, 228 pp.

Wang, X., Chen, W., Chen, D., Wu, Z., Fan, Q. 2016. Long-term trends of fine particulate matter and chemical composition in the Pearl River Delta Economic Zone (PRDEZ), China. *Frontiers of Environmental Science & Engineering*, 10, 53–62. doi: 10.1007/s11783-014-0728-z

Wang, Y., Feng, J., Dan, L., Lin, S., Tian, J. 2020. The impact of uniform and nonuniform CO_2 concentrations on global climatic change. *Theoretical and Applied Climatology*, 139(1-2), 45–55. doi: 10.1007/s00704-019-02924-7

Wasserman, L. 2006. All of nonparametric Statistics. *Springer texts in Statistics*. New York, 123 pp.

Weart, S. R. 1997. The Discovery of the Risk of Global Warming. *Physics Today*, 50(1), 34–40. doi: 10.1063/1.881664

Weart, S. R. 2006. El calentamiento global: historia de un descubrimiento científico. Laetoli, 262 pp.

Webster, H.N., Thomson, D.J., Johnson, B.T., Heard, I.P.C., Turnbull, K., Marenco, F., Kristiansen, N.I., Dorsey, J., Minikin, A., Weinzierl, B., Schumann, U., Sparks, R.S.J., Witham. C.S., Haywood, J.M., Golding, B.W. 2012. Operational prediction of ash concentrations in the distal volcanic cloud from the 2010 Eyjafjallajökull eruption. *Journal of the Geophysical Research:Atmospheres*, 117, 1–17. doi:10.1029/2011JD016790

Westfall, P.H. 2014. Kurtosis as Peakedness, 1905–2014. R.I.P. *The American Statistician*, 68(3), 191–195. doi: 10.1080/00031305.2014.917055

White, M., Nemani, R. 2003. Canopy duration has little influence on annual carbon storage in the deciduous broad leaf forest. *Global Change Biology*, 9, 967–972. doi: 10.1046/j.1365-2486.2003.00585.x

Wilks, D.S. 2019. Statistical methods in the atmospheric sciences, 4nd edn. Elsevier, Amsterdam.

Woelk, M. 2009. Simple, Real-Time measurement of stable isotope ratios in H_2O and CO_2. https://www.picarro.com/products/g2201i_isotopic_analyzer. Accessed 17 March 2020.

WMO Greenhouse Gas Bulletin. 2015. The state of greenhouse gases in the atmosphere based on global observations through 2014. World Meteorological Organization. http://www.wmo.int/pages/prog/arep/gaw/ghg/GHGbulletin.html. Accessed 2 November 2020.

Wu, J., Guan, D., Yuan, F., Yang, H., Wang, A., Jin, C. 2012. Evolution of atmospheric carbon dioxide concentration at different temporal scales recorded in a tall forest. *Atmospheric Environment*, 61, 9–14. doi: 10.1016/j.atmosenv.2012.07.013

Xia, L., Zhou, L., Tans, P.P., Liu, L., Zhang, G., Wang, H., Luan, T. 2015. Atmospheric CO_2 and its $\delta^{13}C$ measurements from flask sampling at Lin'an regional background station in China. *Atmospheric Environment*, 117, 220–226. doi: 10.1016/j.atmosenv.2015.07.008

Yagüe, C., Viana, S., Maqueda, G., Lazcano, M.F., Morales, G., Rees, J.M. 2007. A Study on the Nocturnal Atmospheric Boundary Layer: SABLES2006. Física de la Tierra, 19, 37–53.

Yang, Y., Wang, T., Wang, P., Zhou, M., Yao, B. 2019. In-situ measurement of CO_2 at the Xinglong regional background station over North China. *Atmospheric and Oceanic Science Letters*, 12(6), 385–391. doi: 10.1080/16742834.2019.1644949

Yi, S.-M., Hwang, I. 2014. Source identification and estimation of source apportionment for ambient PM_{10} in Seoul, Korea. *Asian Journal of Atmospheric Environment*, 8(3), 115–125. doi:10.5572/ajae.2014.8.3.115

Yver Kwok, C., Laurent, O., Guemri, A., Philippon, C., Wastine, B., Rella, C.W., Vuillemin, C., Truong, F., Delmotte, M., Kazan, V., Darding, M., Lebègue, B., Kaiser, C., Xueref-Rémy, I., Ramonet, M. 2015. Comprehensive laboratory and field testing of cavity ring-down

spectroscopy analyzers measuring H_2O, CO_2, CH_4 and CO. *Atmospheric Measurement Techniques*, 8(9), 3867–3892. doi: 10.5194/amt-8-3867-2015

Zannetti, P. 1993. Numerical simulation modelling of air pollution: an overview. Air Pollution, Computational Mechanics Publications, 1, 3–11. WIT Transactions on Ecology and the Environment, UK.

Zeng, J., Matsunaga, T., Mukai, H. 2010. METEX-A flexible tool for air trajectory calculation. *Environmental Modelling & Software*, 25, 607–608. doi: 10.1016/j.envsoft.2008.10.015

Zhang, D., Tang, J., Shi, G., Nakazawa, T., Aoki, S., Sugawara, S., Wen, M., Morimoto, S., Patra, P.K., Hayasaka, T., Saeki, T. 2008. Temporal and spatial variations of the atmospheric CO_2 concentration in China. *Geophysical Research Letters*, 35, L03801. doi: 10.1029/2007GL032531

Zhang, F., Zhou, L.X. 2013. Implications for CO_2 emissions and sinks changes in western China during 1995–2008 from atmospheric CO_2 at Waliguan. *Tellus. Series B: Chemical and Physical Meteorology*, 65, 1–14. doi: 10.3402/tellusb.v65i0.19576

Zhou, L., Conway, T.J., White, J.W.C., Mukai, H., Zhang, X., Wen, Y., Li, J., MacClune, K. 2005. Long-term record of atmospheric CO_2 and stable isotopic ratios at Waliguan Observatory: Background features and possible drivers, 1991–2002. *Global Biogeochemical Cycles*, 19, GB2001, doi:10.1029/2004GB002430

Zhu, C., Yoshikawa-Inoue, H. 2015. Seven years of observational atmospheric CO_2 at a maritime site in northernmost Japan and its implications. *Science of the Total Environment*, 524–525, 331–337. doi: 10.1016/j.scitotenv.2015.04.044

2º Institute. 2020. Real-Time and historical methane CH_4 levels. https://www.methanelevels.org/#sources. Accessed 4 September 2020.

*****All references cited in the main text are listed in this section. Specific reference lists of the original contributions are just provided in the corresponding Original Contribution.

11. Appendices

11.1. Acronyms

Table Ap1. Main abbreviations used throughout the thesis.

Abbreviation	Description
AEMET	Spanish Meteorological Agency
AFOLU	Agriculture, Forestry and Other Land Use
CGER	Centre for Global Environmental Research
CIBA	Centro de Investigación de la Baja Atmósfera
COP	Conferences of the Parties
CRDS	Cavity Ring-Down Spectroscopy
DAS	Data Acquisition System
E_{FF}	Fossil fuel emissions
E_{LUC}	Emissions from land use, land use change and forestry activities
EU27	European Union
GHG	Greenhouse gas
GMD	Global Monitoring Division
IPCC	Intergovernmental Panel on Climate Change
Lowess	Locally weighted scatterplot smoothing
LSD	Least Significant Difference
m. a.s.l.	meters above sea level
m. a.g.l.	meters above ground level
METEX	Meteorological Data Explorer
MLO	Mauna Loa Observatory
NCEP	National Centers for Environmental Prediction
NDIR	Non-dispersive infrared
NOAA	National Oceanic & Atmospheric Administration
PBL	Planetary boundary layer
ppm	parts per million
ppb	parts per billion
PVU	Power Vaccum Unit
SIAR	Agroclimatic Information System for Irrigation
S_{LAND}	Terrestrial CO_2 sinks
S_{OCEAN}	Ocean sink
UNEP	United Nations Environment Program
UNFCCC	United Nation Framework Convention on Climate Change
WMO/GAW	Global Atmosphere Watch programme of the World Meteorological Organization
WRF	Weather Research and Forecast

11.2. List of tables and figures

*All tables and figures cited in the main text are listed in this section. The tables and figures of the original contributions are only provided in the corresponding Original Contribution.

11.2.1. List of tables

11.2.2. List of figures


esDUVa
Escuela de Doctorado Universidad de Valladolid
UVa
FacultaddeCiencias
GCA
Grupo de
Contaminación
Atmosférica